STUDIES OF PATHOLOGICAL DYNAMICS AFTER MICROVASCULAR INJURY USING NONLINEAR OPTICAL METHODS

A Dissertation

Presented to the Faculty of the Graduate School

of Cornell University

In Partial Fulfillment of the Requirements for the Degree of

Doctor of Philosophy

by

Nathanael L. Rosidi

August 2011

STUDIES OF PATHOLOGICAL DYNAMICS AFTER MICROVASCULAR INJURY USING NONLINEAR OPTICAL METHODS

Nathanael L. Rosidi, Ph. D.

Cornell University 2011

Microvascular lesions are a common feature in the aging brain and clinical evidence has correlated microvascular pathology with the development of neurodegenerative diseases such as Alzheimer's disease and dementia. Traditional animal models that replicate hemorrhagic and ischemic lesions in the brain typically affect large regions in the cortex and do not reproduce the small-scale lesions linked to neurodegeneration that likely stem from injuries to single microvessels. Due in part to this lack of small-scale injury animal models, there remains an incomplete understanding of the cellular and pathophysiological dynamics following small-scale vascular lesions, making progress on therapeutic strategies difficult. We used tightly focused femtosecond laser pulses to injure single penetrating arterioles (PA) (i.e., arterioles that plunge into the brain) in the cortex of live anesthetized rodents and used two-photon excited fluorescence (2PEF) imaging to quantify blood flow changes and to determine the time course of pathological consequences in the brain after injury.

We find that after ischemic occlusion of a PA, nearby pial and penetrating arterioles do not actively compensate for the reduction of blood flow observed near the occluded blood vessel. We find that capillaries connected downstream to the clotted vessel dilate but other capillaries in the vicinity do not, suggesting that any compensatory signal that results in a physiological response travels vascularly.

We ruptured individual PAs to induce microhemorrhages that resulted in extravasation of blood into the parenchyma. We find that tissue compression due to

the hematoma does not collapse capillaries and cause acute ischemia. 2PEF imaging of mice expressing yellow fluorescent protein (YFP) in a subset of cortical neurons revealed no dendrite degeneration out to seven days after microhemorrhage. However, we did observe an inflammatory response by microglia/macrophages as quickly as 1.5-hrs after microhemorrhage which persisted past seven days. Lastly, we looked at spine (i.e., post-synaptic terminals on dendrites) dynamics on GFP fluorescent cortical dendrites and found a higher rate of spine loss and gain after a nearby microhemorrhage out to 14 days. This higher rate of spine turnover may help provide an understanding of the development of symptomatic dysfunction due to consequences in neuronal rewiring after a microhemorrhage.

The work presented in this dissertation provides quantification of pathological consequences after both ischemic and hemorrhagic injury to a single blood vessel in the brain. We see that after a small-scale ischemic lesion, surrounding blood vessels do not elicit an active response to compensate for a lack of blood flow in the targeted blood vessel and surrounding tissue. After a hemorrhage to a single blood vessel, we do not observe any neuronal degeneration or death. These hemorrhagic lesions, however, do result in an inflammatory reaction that may lead to subtle changes in neuronal rewiring or seed the development of neurodegenerative diseases. The work presented in this dissertation can help provide new insights for the development of novel stroke therapeutics as well as provide cell specific observations about the development of pathological consequences in both ischemic and hemorrhagic lesions in the brain.

BIOGRAPHICAL SKETCH

Nathanael Rosidi was born in Surabaya, Indonesia in 1984. He moved to the United States in 1985 and was raised in the San Francisco Bay Area in California. In 2002 he attended the University of California, Davis majoring in Biosystems Engineering. While at UC Davis, Nathanael was awarded an undergraduate National Science Foundation research fellowship and conducted biomedical engineering research during this time. His first research position was at Stanford University under the guidance of Dr. Thomas Wang and Dr. Christopher Contag, where he developed a dual-axis confocal microscope to detect neoplastic tissue in the clinical setting. Nathanael's second research position was at UC Davis under the guidance of Dr. Atul Parikh. Nathanael helped develop a novel high-throughput and low-cost biosensor microchip capable of detecting multiple diseases simultaneously. He graduated with honors from UC Davis in June of 2006. In August of 2006, Nathanael attended Cornell University as a Ph.D. candidate in the Biomedical Engineering department. He joined Dr. Chris Schaffer's laboratory where he has spent the past five years studying the pathological consequences of microvascular lesions using nonlinear optical methods.

To my

Family and friends

ACKNOWLEDGMENTS

There are many people that I would like to acknowledge that have helped make this dissertation possible and that have helped contribute to a fulfilling graduate experience. First, I would like to thank my advisor, Dr. Christopher Schaffer, for a stimulating and well-rounded Ph.D. experience. I have learned a vast amount of complex nonlinear optical and microscopy techniques used to tackle biological problems. In addition, Chris has also helped me realize that clear, concise writing and presentation skills are equally as important as technical skills. I also appreciate the independence and flexibility that he allowed me, to cater towards my own work schedule and academic interest. I appreciate all the conversations and guidance provided throughout the years. Secondly, I would like to thank Dr. Nozomi Nishimura who started her position as a post-doctorate associate at the time that I started working in the Schaffer Lab. Nozomi was always willing to share her knowledge and experiences as a successful scientist throughout the years. I think of her as my 2nd PI and am thankful to have developed into a successful investigator through her guidance.

I would also like to recognize my committee members, Dr. Joseph Fetcho and Dr. Chris Xu for their trust in my decisions on this graduate path. I am glad to have them on my committee board, both of which have helped tailor my education towards my research interests.

Looking back at the last five years, I feel lucky to have been a part of a dynamic and fun lab group. I started working in the Schaffer lab with Ph.D. candidates John Nguyen and Flor Cianchetti, both of whom I was able to hold insightful, scientific conversations but also partake in light-hearted horseplay. Notably, I enjoyed John's famous gluten-free apple burrito and hope that he is not disheartened by the

numerous culinary losses (at the hands of my superior cooking skills) during Schaffer lab cooking competitions. I enjoyed Flor's humor and practical advice throughout the years. I hope that she will enjoy the west coast and end up permanently located in California (because why even think about living anywhere else?). Puifai Santisakultarm and Matt Farrar both joined the lab during my second year of graduate school. I am glad to have engaged in years of both serious and light-hearted conversations with them. I will look back on the barbeques, post research dinners, and lab activities fondly.

With regards to the next generation of scientists, Elizabeth Wayne and Poornima Gadamsetty, have both contributed to an exciting last year. I am saddened that I could not have passed down some of my technical skills, but have no doubt that their solutions will be more inventive to anything I could have taught. I would like to thank all the undergraduates that have collaborated with me. Joan Zhou, for passing down her surgical skills and for help with the dendrite portion of the microhemorrhage project. Sanket Pattanaik, for the help with the microglia portion of the microhemorrhage project. My most recent undergraduate, Susie Jin, for the help with both the dendrite spine and microhemorrhage projects. Morgan Brophy, for learning and successfully performing histology in such a short time. I would also like to acknowledge past lab members and graduated students. Jennifer Shum, Chanson Chang, Josie Bodle, and Jillian Ferdman for being great snowboarding friends throughout the years in Ithaca. Andrew Fong and Andrew Davis for providing interesting conversations on a daily basis. I am truly thankful for all the smart, successful students Cornell University admits.

On the homeside, I would like to thank Jonathan Bryant, Stanley Hsu, Erica Tong, and Lindsey Chin-Jones for enriching my undergraduate experience. I greatly appreciate the balance of class work and extracurricular activities provided during my

years at UC Davis. I am most thankful and deeply indebt to my childhood friends: Scott Lewis, David Yang, Matthew Cheung, Jeremy Takahashi, Phillip Wang, and Amir Seperhdad. We have grown together since grade school and have shared many experiences that have shaped our friendship. I am thankful for the work-life balance throughout the years, especially during my undergraduate and graduate career (fantasy basketball and Vegas trips definitely made Ithaca bearable). This quote, by Bill Simmons (coincidentally written about his trip to Las Vegas with his childhood friends), sums up our friendship:

"The truth is, you have your oldest friends in life, and then you have everyone else. Nothing will trump your oldest friends. Any amount of time can pass without your feeling as if you've grown apart because, really, you can't."

Jane Yang is an amazing person and has stood at my side through my last years in graduate school. She provided a refreshing scenery change and helped direct my focus to aspects of life outside of science. I thank Jane for providing the much needed balance in my life and providing a long-term vision of the future that does not necessarily involve work and career aspirations. I cannot wait for the next chapter in our lives to begin and am excited to share many more experiences together.

Last but not least, I would also like to thank my parents, Dario and Josephine Rosidi, who have been exceptional parents and mentors throughout my life. They are always supportive of my decisions and have always been proud of my accomplishments. They constructively emphasize having good life qualities such as being well rounded and being able to appreciate everything I have. I would also like to thank my younger sister, Denise. She is proof that hard work, independence, ambition and compassion will lead to great things in life.

TABLE OF CONTENTS

LIST OF FIGURES

LIST OF TABLES

LIST OF ABBREVIATIONS

2PEF	two-photon excited fluorescence
ACH	acetylcholine
AD	Alzheimer's disease
ATP	adenosine triphosphate
CADSIL	cerebral autosomal dominant arteriopathy with subcortical infarcts and leukoencephalopathy
CBF	cerebral blood flow
CNF	Cornell University Nano Facility
CX3CR1	CX3C receptor 1
CX3CL1	CX3L ligand 1
DNA	deoxyribonucleic acid
GFAP	glial fibrillary acidic protein
GFP	green fluorescent protein
ICH	intracerebral hemorrhage
IQR	interquartile range
LED	light emitting diode
MCA	middle cerebral artery
MRI	magnetic resonance imaging
PA	penetrating arteriole
PBS	phosphate buffered saline
RB	rose Bengal
RBC	red blood cell

ROS	reactive oxygen species
tPA	tissue plasminogen activator
YFP	yellow fluorescent protein

CHAPTER ONE

INTRODUCTION AND ORGANIZATION OF DISSERTATION

INTRODUCTION

Small-scale microvascular lesions that affect single blood vessels in the brain are a common feature among the elderly. Recent evidence has linked an accumulation of these injuries to the development of neurodegenerative diseases such as dementia, loss of memory, and Alzheimer's disease. In the clinical setting, symptoms of stroke and neurodegenerative disease are the end result of the pathological development due to small-scale lesions. Little is known about the progression of the physiological pathology to surrounding tissue and cerebral blood flow surrounding the microvascular injury.

There are several traditional animal models to study injury in the brain. The injuries in these animal models can be categorized by size and type. Large-scale injuries affect blood vessels that supply several downstream vessels and are crucial for a major portion of the blood flow through the brain. Small-scale injuries typically involve smaller, single blood vessels that do not affect large areas in the brain. The focus of this dissertation is of small-scale microvascular injuries to single cortical microvessels affecting diameters of $<500\ \mu$m.

The second category of animal models used to study brain injury is the type of lesion. Lesions can be classed as ischemic or hemorrhagic. In ischemic occlusions, blood flow is blocked and the development of pathological consequences such as cellular death and redistribution of collateral blood flow is studied. The progression and development of any deleterious affects observed from ischemic occlusions may be different compared to hemorrhagic lesions in the brain and must be classed accordingly. In this dissertation, we study pathological affects in both ischemic and

hemorrhagic injuries to single blood vessels in the brain.

Recently, femtosecond lasers have been introduced as a method to induce targeted injury in biological samples. This method coupled with two-photon excited fluorescence imaging together allow for time-lapse observations after injury of a single blood vessel in the brain. In this dissertation, we study any pathological affects of stroke over several weeks in a live intact animal. We hope that our observations can provide new insights in understanding the development of neurodegenerative disease and lead to the new therapeutic platforms for clinical stroke.

ORGANIZATION OF DISSERTATION

The work described in this dissertation involves the study of pathological consequences of small scale strokes using nonlinear optical methods previously developed by *Nishimura et al*.[1]. In each chapter, we looked at pathological consequences in specific biological structures in the brain after inducing either an occlusion or microhemorrhage. For this reason, each chapter can be read independently.

Chapter 2: This chapter provides an introduction on nonlinear imaging, specifically two-photon excited fluorescence used in all experiments in this dissertation. The chapter describes the generation of two-photon excited fluorescence, its advantages over linear microscopy, and its applications in the research setting. This chapter also discusses ionization mechanisms used to damage biological systems and was used to damage blood vessels in the brain in all the experiments in this dissertation.

Chapter 3: This chapter briefly describes two different types of microvascular injuries

in the brain: ischemic occlusions and microhemorrhages. The section on ischemic occlusions describes consequences to blood flow and cells after large and small-scale stroke, and is relevant to the work described in Chapter 4. The section on intracerebral hemorrhages describes pathological consequences to ruptures of blood vessels in the brain and is relevant to work in Chapter 5-7.

Chapter 4: Previous investigations have found that arterioles on the surface of the brain can reroute blood flow to compensate for a drop in blood flow due to a blockage. However, little is known about compensation mechanisms when an occlusion to a penetrating arterioles forms. This chapter describes the behavior of surrounding penetrating arterioles, pial arterioles, and capillaries after an occlusion to a penetrating arteriole. Measurements in blood flow for these different classes of blood vessels provide insight on compensation mechanisms after a stroke and can provide paths to new therapeutic platforms.

Chapter 5: Mechanisms by which microvascular hemorrhages lead to death or dysfunction in the brain remains unclear. Microhemorrhages in the brain lead to extravasation of blood components into the parenchyma and may underlie the development of neurodegenerative disease. In this chapter we characterize the dynamics of a rupture to a penetrating arteriole to understand the spatial and temporal effects of a microhemorrhages. We look at the pathological consequences after a microhemorrhage to surrounding tissue. Lastly, we look at the inflammatory response over several days to understand how the brain is affected by a microhemorrhagic injury.

Chapter 6: Dendrite spines are a membranous protrusion from a neuron and it is

thought that a rearrangement in spines on the dendrite shaft contributes to learning. Recent evidence shows that the morphological structure of dendrites degenerate during ischemic occlusion but maintain their structure after a microhemorrhage, as described in Chapter 5. The work in this chapter describes dendrite spine dynamics after a microhemorrhage of a penetrating arteriole. We look at spine growth and retraction rates compared to normal brain to provide an understanding of how neurodegenerative diseases may develop over time.

Chapter 7: Tissue plasminogen activator (tPA) is a drug used by clinicians to treat stroke. However, little is known on the effects of tPA on hemorrhages in the brain. In this chapter we intravenously infuse tPA before a microhemorrhage too study any deleterious effects the drug may have on the brain. If tPA does not enlarge the hemorrhage volume then it can potentially be administered before a brain scan and reduce treatment times to help patients with ischemic stroke reestablish blood flow in the brain .

Chapter 8: This chapter discusses the development of a curriculum for high school science students. The curriculum centers around the concept of blood flow in the brain during normal and disease states. Two laboratory exercises are discussed which are analogous to flow in the brain. This chapter also includes an assessment of the curriculum from the students.

Chapter 9: This chapter summarizes important findings from previous chapters. This chapter also addresses open questions regarding the work on small-scale microvascular injury and its importance in the clinical setting.

REFERENCES

1. Nishimura, N., *et al*. Targeted insult to subsurface cortical blood vessels using ultrashort laser pulses: three models of stroke. *Nature Methods* **3**, 99-108 (2006).

CHAPTER TWO

NONLINEAR OPTICAL METHODS TO STUDY AND MANIPULATE BIOLOGICAL SYSTEMS

Permission to reproduce Figure 2.1 and 2.2 was granted by Institute of Physics Publishing Ltd

Schaffer, C.B., Brodeur, A. & Mazur, E. Laser-induced breakdown and damage in bulk transparent materials induced by tightly focused femtosecond laser pulses. *Meas Sci Technol* **12**, 1784-1794 (2001)

Permission to reproduce Figure 2.3 was granted by Optical Society of America

Schaffer, C.B., Nishimura, N., Glezer, E.N., Kim, A.M.T. & Mazur, E. Dynamics of femtosecond laser-induced breakdown in water from femtoseconds to microseconds. *Optics Express* **10**, 196-203 (2002)

NONLINEAR OPTICAL METHODS FOR IN VIVO IMAGING

Optical methods to study biological systems provide a minimally invasive way to observe dynamics of normal and disease state systems. Past studies using conventional linear microscopy techniques such as video microscopy [1], laser Doppler flowmetry [2], and confocal microscopy [3] have been used to study biological systems for decades. In addition, medical imaging techniques such as positron emission and functional magnetic resonance imaging have provided a means to obtain high-resolution images and quantitative information of biological activity [4]. Recent advances in nonlinear microscopy, such as two-photon excited fluorescence (2PEF) imaging [5], over the past two decades have allowed for studies of biological systems that can resolve sub-cellular structure, function, and dynamics of specific-cell types in vivo. These recent developments in optical tools have allowed for relatively non-invasive preparations where intact biological systems can be studied over a time span of months [6]. The work presented in this dissertation uses 2PEF imaging as a tool to study normal and disease state processes in the brain of live anesthetized rodents.

In this introductory chapter we discuss the use of nonlinear optics for visualization and manipulation of biological systems. An overview of 2PEF generation and its advantages for in vivo work will be discussed as well as femtosecond duration laser ablation mechanisms used to damage biological structures with micrometer precision. Using a femtosecond duration laser, we are able to precisely ablate biological structures, causing minimal collateral damage, in the brains of live anesthetized animals enabling the study of any pathological consequences due to injury.

Two-photon excited fluorescence generation

2PEF works by generating fluorescence at a known localized volume in the sample.

Two photons are simultaneously absorbed to produce excitation energy equivalent to excite a fluorescent molecule. The energy of the two excitation photons is typically half of the absorption energy of a single photon needed to stimulate the fluorescent molecule. These two photons need to interact with the fluorescent molecule nearly simultaneously (within 10^{-16} s), resulting in an absorption probability that is quadratically dependent on the light intensity [7]. Achieving a sufficiently high intensity at an average power that a biological sample will safely tolerate requires the use of femtosecond duration laser pulses to drive this nonlinear process. This is achieved using a mode-locked femtosecond duration laser to achieve a low average power, but high peak power at specific durations. Mode-locking is a technique used to induce a fixed phase relationship between the modes of the laser's resonant cavity, thereby producing pulses of high intensity light. When a laser beam is tightly focused inside a sample, the intensity will be greatest at the focus. The nonlinear dependence of fluorescence on intensity then ensures that fluorescence is generated only in a diffraction-limited volume at the focus of the laser beam. This laser focus is then scanned in three dimensions to map the distribution of fluorescence in the sample, enabling subsurface imaging, hundreds of micrometers deep inside the tissue. Scattering only mildly affects the image quality because all detected fluorescence, scattered or not, contributes to the signal rather than producing background as in other fluorescence imaging techniques.

Advantages of 2PEF microscopy

One advantage of 2PEF imaging over linear fluorescence imaging techniques is that signal generation originates from the focus of the beam at a known location, thus any scattered fluorescence that reaches the detector is not background but signal. Raster-scanning the excitation beam over the specimen produces an axially isolated emission

plane that forms the image. Linear microscopy techniques are limited to biological tissue scattering lengths that quickly degrade the image resolution due to scattering of photons from the focus and collection of out-of-focus fluorescence. Collecting emission fluorescence from the focus contributes to the ability to image deeper, since any scattered photons passing through the biological sample is signal. Moreover, since fluorescent signal is only produced at the focal point, phototoxicity is also reduced compared to one photon imaging techniques. This feature of 2PEF greatly reduces photodamage and photobleaching in other regions of the sample, since high intensities will be found at the focus.

Another advantage of 2PEF imaging is that it uses standard fluorescent molecules and dyes such as fluorescein, Alexa dyes, green fluorescent protein (GFP), and yellow fluorescent protein (YFP). In addition, UV absorbing molecules can easily be excited at 700-800 nm rather than 350-400 nm, making 2PEF useful for detecting intrinsic species such as NADH without damaging the biological sample [8]. Another advantage is the ability to provide second harmonic generation (SHG) contrast seen in biological tissues such as cartilage and collagen [7]. These advantages as well as the ability to image deep in live tissue make 2PEF imaging a popular biological imaging tool.

Applications of 2PEF microscopy

2PEF microscopy has become a popular tool for biological imaging and allows for non-invasive fluorescent microscopy of living and fixed tissue. 2PEF imaging has been used to demonstrate 500-μm deep calcium transients in mouse brain [8] as well as to quantify blood flow, through intravenous injection of dextran-conjugated fluorescent dye, in the microcirculation of live rodents [9, 10]. An intravenous injection of fluorescent dye labels the blood plasma, leaving the red blood cells as shadows

flowing through the blood vessels. The 2PEF scanning laser can be scanned along a blood vessel, capturing the motion of the red blood cells as streaks across the image. The slope of the streaks is proportional to the inverse of the velocity and has been detailed by Schaffer *et al*. [11]. This method for extracting blood vessel velocity is used throughout this dissertation to quantify blood flow through different classes of vessels.

2PEF microscopy has also been used to visualize specific cell-types such as fluorescently labeled pyramidal neurons and microglia in live anesthetized mice. Recent investigations that capture the dynamics of GFP-labeled microglia and YFP-labeled dendrites of layer V pyramidal neurons after brain injury have both used 2PEF imaging to highlight cell-specific dynamics due to injury and disease [12, 13].

NONLINEAR OPTICS FOR MANIPULATING BIOLOGICAL SYSTEMS

Femtosecond duration lasers have been used on non-biological materials to characterize and enable subsurface micromachining of transparent materials [14] as well as fabricating three-dimensional structures of several hundred micrometers with nanoscale features [15]. In the past decade, femtosecond ablation has emerged as a technique to manipulate structures in biological systems, such as blood vessels and neurons in the cortical layer of live rodents. This technique for precise biological manipulation allows for the study of consequential dynamics and effects in an in vivo environment. Femtosecond ablation can be used to generate animal models that reproduce disease states seen clinically in humans such as microstrokes that are thought to correlate to cognitive decline and the development of neurodegenerative diseases [16]. Femtosecond ablation coupled with 2PEF microscopy can be used to study these disease states acutely and chronically over several weeks.

Mechanisms of femtosecond ablation

At low light intensities, photons pass through transparent material without ionization (i.e., a dissociation of material into ions). For example, sunlight passes through transparent glass without ionization of the material. However, at light intensities around 10^{13} W/cm^2, the density of photons passing through a transparent material has a high probability of interacting with molecules in the material, thereby transferring energy into the material. This deposition of energy from the light source is absorbed by the material and causes the production of ion-plasma. Plasma formation and expansion results in physical damage of the material. Here we will discuss several mechanisms of nonlinear excitation that leads to ionization and permanent damage of transparent material.

Regimes of photoionization: mechanisms of tunneling and multiphoton ionization

Because a single photon of visible light does not have enough energy to ionize transparent material, multiple photons must simultaneously combine energies to excite electrons in the material; this process is termed nonlinear photoionization. Depending on the laser frequency and intensity there are two different regimes of photoionization: tunneling ionization and multiphoton ionization. At low laser frequencies and strong electric laser fields, tunneling ionization typically occurs. In this regime the electric field of the laser is so strong that it acts as a barrier for electrons to surpass the Coulomb well, forcing electrons to tunnel through the Coulomb well to become free [17]. An analogous illustration is to imagine a ball without enough momentum to overcome a hill, so it is left to tunnel through the hill to set itself free. This physical process, or ionization, leads to the conversion of the molecule into an ion as electrons are removed through this tunneling process.

However, at high laser frequencies, multiple photons simultaneously interact with an electron to promote the electron in the valence band to a higher energy state

termed conduction band. This regime is termed multiphoton ionization. The total photon energy absorbed by the electron must be equal to or greater to the energy band-gap (i.e., the minimum energy required to transition from the valence band to the conduction band). of the material, allowing the electron to transition to the conduction band from the valence band.

The transition between tunneling and multiphoton ionization is expressed by the Keldysh parameter [18].

$$\gamma = \frac{\omega}{e}\left[\frac{mcn\varepsilon_0 E_g}{I}\right]^{\frac{1}{2}} \qquad (1)$$

where ω is the laser frequency, I is the laser intensity at the focus, m and e are the reduced mass and charge of the electron, c is the velocity of light, n is the refractive index of the material, E_g is the band-gap of the material, and ε_0 is the permittivity of free space [17]. When the Keldysh parameter is lower than 1.5, the photoionization is a tunneling process and becomes a multiphoton process when the parameter is greater than 1.5. However, when the Keldysh parameter is between the two regimes, photoionization is a mix between the two processes. The two regimes and the intermediate process are depicted in Fig. 2.1.

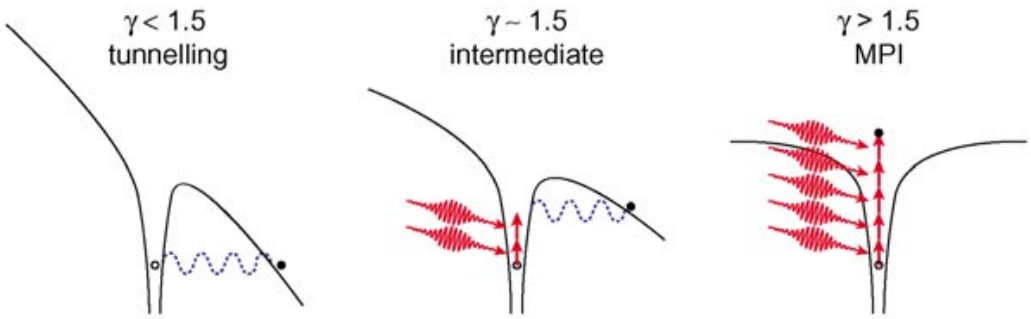

Figure 2.1 Schematic diagram of photoionization of an electron of different Keldysh parameter values. Adapted from reference [17]

Mechanism of avalanche ionization

The second ionization process requires high laser intensities and is termed avalanche ionization. In this process an electron in the conduction band moves to a higher energy state due to absorption of additional laser photons as illustrated in Fig. 2.2. The electron then collides with an electron in the valence band, transferring its energy to bring both electrons into the conduction band. This is plausible only if the electron, originally in the conduction band, posses' energy exceeding the band-gap minimum. The result of the collision is two electrons with energies that meet the conduction band minimum. Through additional energy absorption from laser photons, this process can grow according to:

$$\frac{dN}{dt} = \eta N \qquad (2)$$

where η is the avalanche ionization rate.

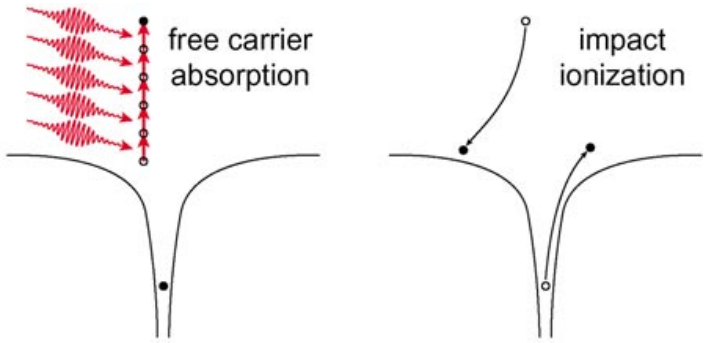

Figure 2.2 Schematic diagram of avalanche ionization [17]

Mechanisms of material damage

In our work using femtosecond duration lasers, ionization can lead to electron-ion

plasma in which electrons are separated from their molecules [19]. This processes produces kinetic energy and expands until all energy is depleted. As the expansion stops, a pressure wave propagates outward and the plasma recombines into a gas-filled bubble that expands as a cavitation bubble, both seen in the 6.4 ns image in Fig. 2.3. During this time, the plasma, subsequent pressure wave, and cavitation bubble causes permanent mechanical damage to the material [20].

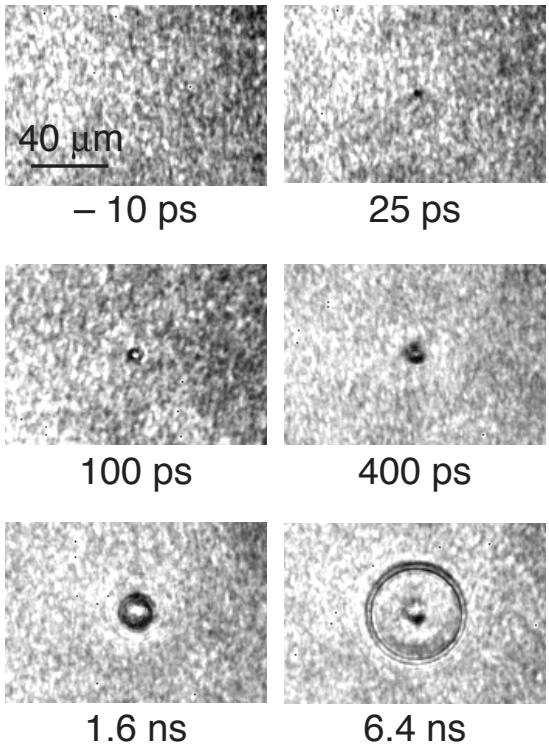

Figure 2.3 Time-lapse images of ionization of water at the focus by femtosecond laser. Images are of ionization, shockwave, and cavitation bubble [20]

The damage to the material can be controlled by limiting the size of the focal volume. By tightly focusing the femtosecond laser, the nonlinear absorption will occur only at the focus and ionize only the electrons present in the volume and nowhere else, resulting in a small damaged volume. In addition, controlling the laser pulse energy and repetition rate can limit the size of the affected volume. Irradiation of the material

by repetitive pulses of low energy can lead to a cumulative effect that ionizes the focal volume of the material without increasing the affected volume size compared to a single femtosecond pulse of high energy.

We used the femtosecond ablation technique to rupture and occlude blood vessels in the cortex of a live rodent. The use of a femtosecond duration laser to ablate features in biological systems was pioneered by Nishimura *et al*.[9] where three models of stroke was produced. The work presented in this dissertation uses Nishimura's method to induce occlusions and microhemorrhages to cortical blood vessels in live anesthetized rodents.

REFERENCES

1. MacVicar, B.A. Infrared video microscopy to visualize neurons in the in vitro brain slice preparation. *J Neurosci Methods* **12**, 133-139 (1984).

2. Nilsson, G.E., Tenland, T. & Oberg, P.A. Evaluation of a laser Doppler flowmeter for measurement of tissue blood flow. *IEEE Trans Biomed Eng* **27**, 597-604 (1980).

3. Rajadhyaksha, M., Grossman, M., Esterowitz, D., Webb, R.H. & Anderson, R.R. In vivo confocal scanning laser microscopy of human skin: melanin provides strong contrast. *J Invest Dermatol* **104**, 946-952 (1995).

4. Kerr, J.N.D. & Denk, W. Imaging in vivo: watching the brain in action. *Nature Reviews Neuroscience* **9**, 195-205 (2008).

5. Denk, W., Strickler, J.H. & Webb, W.W. Two-photon laser scanning fluorescence microscopy. *Science* **248**, 73-76 (1990).

6. Xu, H.T., Pan, F., Yang, G. & Gan, W.B. Choice of cranial window type for in vivo imaging affects dendritic spine turnover in the cortex. *Nature neuroscience* **10**, 549-551 (2007).

7. Zipfel, W.R., Williams, R.M. & Webb, W.W. Nonlinear magic: multiphoton microscopy in the biosciences. *Nature Biotechnology* **21**, 1368-1376 (2003).

8. Williams, R.M., Zipfel, W.R. & Webb, W.W. Multiphoton microscopy in biological research. *Current opinion in chemical biology* **5**, 603-608 (2001).

9. Nishimura, N., *et al*. Targeted insult to subsurface cortical blood vessels using ultrashort laser pulses: three models of stroke. *Nature Methods* **3**, 99-108 (2006).

10. Kleinfeld, D., Mitra, P.P., Helmchen, F. & Denk, W. Fluctuations and stimulus-induced changes in blood flow observed in individual capillaries in layers 2 through 4 of rat neocortex (vol 95, pg 15741, 1998). *P Natl Acad Sci USA* **96**, 8307-8307 (1999).

11. Schaffer, C.B., *et al*. Two-photon imaging of cortical surface microvessels reveals a robust redistribution in blood flow after vascular occlusion. *PLoS Biol* **4**, e22 (2006).

12. Zhang, S., Boyd, J., Delaney, K. & Murphy, T.H. Rapid reversible changes in dendritic spine structure in vivo gated by the degree of ischemia. *J Neurosci* **25**, 5333-5338 (2005).

13. Davalos, D., *et al*. ATP mediates rapid microglial response to local brain injury in vivo. *Nat Neurosci* **8**, 752-758 (2005).

14. Schaffer, C.B., Brodeur, A., Garcia, J.F. & Mazur, E. Micromachining bulk glass by use of femtosecond laser pulses with nanojoule energy. *Optics letters* **26**, 93-95 (2001).

15. Korte, F., *et al*. Towards nanostructuring with femtosecond laser pulses. *Appl Phys a-Mater* **77**, 229-235 (2003).

16. Cullen, K.M., Kocsi, Z. & Stone, J. Microvascular pathology in the aging human brain: Evidence that senile plaques are sites of microhaemorrhages. *Neurobiol Aging* **27**, 1786-1796 (2006).

17. Schaffer, C.B., Brodeur, A. & Mazur, E. Laser-induced breakdown and damage in bulk transparent materials induced by tightly focused femtosecond laser pulses. *Meas Sci Technol* **12**, 1784-1794 (2001).

18. Keldysh, L.V. Diagram Technique for Nonequilibrium Processes. *Sov Phys Jetp-Ussr* **20**, 1018-& (1965).

19. Stuart, B.C., *et al*. Nanosecond-to-femtosecond laser-induced breakdown in dielectrics. *Phys Rev B* **53**, 1749-1761 (1996).

20. Schaffer, C.B., Nishimura, N., Glezer, E.N., Kim, A.M.T. & Mazur, E. Dynamics of femtosecond laser-induced breakdown in water from femtoseconds to microseconds. *Optics Express* **10**, 196-203 (2002).

CHAPTER THREE

CLINICAL AND RESEARCH ASPECTS OF ISCHEMIC AND HEMORRHAGIC MICROVASCULAR INJURIES IN THE BRAIN

INTRODUCTION

The human symptoms of stroke involves the development of neurological deficits that can compromise the ability of the patient to function independently even after recovery. Some of these deficits include cognitive decline, dementia, motor control loss, and memory loss [1]. The origin of these neurological deficits can be traced back to blockages or ruptures of blood vessels in the brain that affect the health of tissue around the site of injury. An analysis of stroke patients revealed that 75% of clinical stroke were due to a blockage in a large blood vessel, while hemorrhages comprised 11% of stroke patients [2]. Therefore, to understand the pathological origins and consequences of stroke, it is important to study both blockages as well as ruptures to blood vessels in the brain.

PATHOLOGICAL CONSEQUENCES OF ISCHEMIC OCCLUSIONS

A highly redundant network of blood vessels feed the brain to ensure an adequate supply of nutrition and oxygen is supplied for proper function and health. Blockages to these blood vessels can lead to cellular death and dysfunction of nearby brain tissue. In the clinical assessment of stroke, diffusion-weighted magnetic resonance imaging (MRI) can be used to locate blockages or ischemic lesions in the brain within the first few hours of stroke onset [3]. Patients displaying stroke symptoms are typically treated with tissue plasminogen activator (tPA), as the drug has been demonstrated to be effective within the first three hours after ischemic stroke [4]. In addition to symptomatic ischemic brain lesions that can lead to tissue death, asymptomatic brain infarcts (ie, a small localized area of dead tissue) are also found in patients and are common among the elderly. Evidence has shown an accumulation of these infarcts in the brain contribute to neurodegenerative diseases such as dementia and Alzheimer's disease [5, 6]. These infarcts appear as dark dots on MRI scans of the brain, where the dark dots are

injury sites comprised of blood products such as haemosiderin [7]. These lesions are termed cerebral microbleeds and are defined as dark patches that appear <5 mm on T-2* weighted MRI scans [8]. Post-mortem analysis in patients with microbleeds have revealed that these small-scale lesions are <200 μm in diameter, contain haem-rich deposits, and are common in patients >70 years of age. These lesions typically appear around capillaries and small arterioles [9].

Large occlusions in the brain typically comprise of a blockage to a blood vessel that feeds several downstream arterioles. To study the pathological consequences of large scale occlusions, investigators typically use animal models to occlude large blood vessels such as the middle cerebral artery (MCA) or the bilateral carotid, shunting the supply of blood to downstream blood vessels and ultimately reducing cerebral blood flow (CBF) over a large area. This reduction in blood flow has a deleterious effect on nearby cellular tissue as early as 10 minutes after occlusion with irreversible damage observed 60 minutes after injury [10]. Physiological consequences after occlusions to smaller blood vessels have also been studied. Focal occlusions by photothrombosis can be used to study the effects of a blockage to a single blood vessel [10-12]. These focal occlusions can have similar consequences to larger MCA occlusions, with cellular degeneration and death observed in both injury models.

Cerebral blood flow and ischemia

Blood flow rearrangement is an important topic to help assess vascular function and cellular health after an ischemic occlusion, as blood flow regulation and rates are different between normal and pathological states. In human stroke, clinicians observe neurological symptoms that impair stroke victims, while researchers investigate the temporal and spatial physiological consequences of ischemic occlusions. In the first

few hours following occlusion, a severely low CBF is observed and corresponds to the ischemic core destined to develop into an infarction zone [13]. The CBF around the ischemic core is generally higher than in the ischemic zone and does not lead to infarction. Between the 1st and 6th day after ischemic occlusion, a 47% decrease in CBF compared to baseline has been observed in the infarction zone [14]. This low CBF perfusion through the infarction zone typically leads to poor clinical outcome. Surprisingly, between the 6th and 21st day after occlusion, CBF in stroke patients is variable and can result in increases in CBF through the infarction zone [14].

Animal models studying blood flow after occlusion of large blood vessels, such as the MCA and bilateral carotid have been extensively characterized. Ischemic animal models have revealed a decrease in CBF compared to baseline values after reperfusion [15]. In contrast, other investigators have observed an increase in CBF 2-3 times pre-occlusion levels several minutes after occlusion [16] but this elevation lasted less than an hour before a reduction in CBF 20% below baseline values was observed. This post-ischemic hyperemia is thought to be due to high blood pressure and to a decrease in vascular resistance [16]. In other animal models where a permanent occlusion was induced, large infarction zones ~37% of the ipsilateral hemisphere was observed 72 hours after occlusion [17].

Lastly, animal models studying blood flow after small vessel occlusion have recently been investigated. These small vessels typically comprise of single arterioles and venules in the cortex of rats and mice. Different classes of blood vessels in the brain have shown differences in regulation mechanisms that maintain CBF rates. Past investigations have revealed intact dilation mechanisms of cortical arterioles in the pneumbra of the lesion that help to keep adequate levels of blood flow to supply oxygen and nutrition to surrounding cells [18]. Redistribution of blood flow in pial arterioles (i.e., the arterioles that propagate on the surface of the cortex and supply

arterioles that dive down into the brain) after an occlusion have helped preserve the supply of blood to the occlusion site so that nearby tissue remains unaffected [11]. Conversely, the arterioles that dive down into the brain, penetrating arterioles (PA), are most affected by blockages as blood flow around the injury site is compromised [12]. Past work by Nishimura *et al*. [12] has shown that occlusions to PAs lead to blood flow that is dramatically decreased in vessels downstream from the occluded PA, leading to a region of cellular death near the occlusion. The work presented in chapter 4 discusses observations in blood flow regulation that may lead to this infarct region observed by Nishimura. Specifically, the work in chapter 4 discusses blood flow rearrangement and compensation by nearby penetrating and pial arterioles following occlusion of a single PA.

Pathological consequences to neurons and astrocytes after ischemic stroke

In any cerebral ischemia model, the change in CBF is crucial for understanding the development of pathology seen in surrounding tissue. Changes in CBF can lead to degeneration of cellular structures and have been observed after an occlusion to a cortical blood vessel. Blood flow after an occlusion leads to regions of hypoperfusion and past studies have found that cellular degeneration is observed if CBF is less than 10% of baseline [10]. This low CBF leads to a reduction of nutrition and oxygen to surrounding tissue, resulting in cellular death and an infarct zone after occlusion [19].

Focal photothrombotic occlusion methods, causing blood flow cessation to a single or few blood vessels in the brain, have revealed signs of neuronal dysfunction and structural degeneration (i.e., blebs) during the duration of ischemia [20]. This region of ischemia revealed stalling of blood vessels, resulting in structural degeneration of nearby neurons immediately after occlusion [10]. Within 12 hours of an occlusion, astrocytes and neurons show morphological changes in the ischemic region

comprising of neuronal shrinking and astrocyte swelling [21]. Time lapse studies that track cellular health six hours to thirty days after an ischemic occlusion has revealed cell death and necrosis in the ischemic tissue zone with various deleterious morphological changes of neurons [15, 22]. In addition, long-term studies of pathological consequences after ischemia reveal that astrocytes activate around the infarct zone leading to an increase in glial fibrillary acidic protein (GFAP) [22]. Taken together, CBF is drastically compromised by occlusions of blood vessels and hinders the supply of oxygen and nutrients to nearby tissue in the brain, resulting in deleterious pathology.

Inflammatory response after ischemic occlusion

Inflammatory cells such as microglia and macrophages have been shown to respond to ischemic occlusions. Blood-derived macrophages and monocytes infiltrate the parenchyma 12 hours after injury as microglia are observed to respond after six hours before morphologically transforming into phagocytes within the first few days [23]. These inflammatory cells comprised of microglia, macrophages, and monocytes continuously increase in numbers out to 14 days after injury and help clear out debris and necrotic cells [23, 24].

PATHOLOGICAL CONSEQUENCES OF INTRACEREBRAL HEMORRHAGES

In contrast to occlusions that block blood flow to parts of the brain, intracerebral hemorrhages (ICH) are blood vessel ruptures that lead to extravasation of blood into brain parenchyma, often without cessation of flow. ICH leads to a 44% mortality rating and is twice more prevalent than other hemorrhages, such as subarachnoid hemorrhages, which involve extravasation of blood between the pia matter and arachnoid membrane [25]. Furthermore, recent clinical evidence has shown that

microhemorrhages, i.e., ruptures to a single blood vessel, are prevalent in the brain and often asymptomatic. These microhemorrhages can accumulate over years and have been clinically correlated to cognitive decline in the elderly [9].

Methods to induce intracerebral hemorrhages

Traditional ICH animal models have provided a means to study the physiological impact due to bleeds in the brain. One injury models acts by either infusing intact or lysed red blood cells (RBC) into the parenchyma of the brain. Another ICH injury model uses injection of bacterial collagenase that degrade collagen found in the basal lamina of blood vessels, thereby, rupturing capillary vessels. Lesion sites in these injury models typically affect volumes of 15 to 150 mm^3 and can take up most of stratium [26]. These models also have their disadvantages, as long-term studies have been limited due to observed functional deficits that can result in the death of the subject. The collagenase infusion model has been shown to produce an exaggerated inflammatory response and can be directly toxic to neurons at higher doses [27]. Despite these disadvantages, these models are still used to study physiological consequences of large-scale hemorrhages in the brain.

Models that study the effects of hemorrhages of multiple vessels have traditionally used transgenic mice. Transgenic mice models such as hypertensive mice and NOTCH3 mutant mice expressing characteristics of cerebral autosomal dominant arteriopathy with subcortical infarcts and leukoencephalopathy (CADSIL) have been observed to experience spontaneous small vessel hemorrhages [28, 29]. These mice experience random ruptures to blood vessels in the brain and can have infarct sizes spanning 150 μm to 21 mm in diameter [30]. However, these transgenic mice models have been shown to exhibit pathology unassociated with the hemorrhages. For example, CADASIL mutant mice have shown degeneration of smooth muscle cells

and presence of granular osmiophilic material in addition to vascular hemorrhaging [31]. Furthermore, CADASIL mutant mice have shown physiological impairment such as functional hyperemia attenuation and cerebral blood flow autoregulation impairment making physiological effects due solely to the hemorrhage difficult to decouple [32]. Despite this observed uncorrelated pathology, these ICH models provide a valuable method to study pathological consequences of the accumulation of small-scale ICH in the brain.

Consequences of ICH on neurons and astrocytes

ICH models have shown similar pathological effects to ischemic brain injury. Apoptosis of neurons and astrocytes have been seen in the center and periphery of the hemorrhage 24-hr after injection of blood [33]. Furthermore, complimentary experiments using whole blood infusion have shown that both astrocytes and neurons show signs of apoptosis near the hematoma six hours after infusion [34]. These results indicate that the affects of extravasted blood in the parenchyma are toxic to neurons and astrocytes, due to several mechanisms such as toxicity of blood components and increases in intracranial pressure.

Secondary and delayed pathological injury after ICH

Secondary effects of the ICH can cause physiological degeneration of tissue and cells around the hemorrhage site. 17% of patients with hemorrhages also experience hematoma enlargement within 24 hours of the injury. This enlargement contributes to a physical tissue shift and can accelerate neurological degeneration [35].

Brain edema after ICH has been observed both in clinical patients and in experimental studies involving rodents. In experimental models, edema is observed to peak during the 3rd to 4th day after hemorrhage but does not peak until the 10th to 20th

day after hemorrhage in human patient studies [35]. Edema formation increases intracranial pressure and can lead to compression of cellular components resulting in dysfunction and blood vessel collapse. This edema formation is attributed by many factors. For example, the extravasation of RBCs and other blood components into the parenchyma contributes to brain edema due to the lysis of RBCs. This RBC lysis can damage surrounding tissue due to the release of hemoglobin that causes oxidative stress and free radical generation [36].

Apotosis and necrosis of surrounding tissue have been found adjacent to the ICH. It is thought that mechanical forces during hematoma formation or toxicity from blood components contribute to the cell death observed in the perihematomal zone in many studies [36].

Cerebral blood flow and ischemia after ICH

Whether cerebral ischemia occurs in the brain after an ICH remains controversial. When a hemorrhagic volume exceeds 150 mL of blood in the parenchyma, blood perfusion pressure to the brain falls to zero resulting in patient death. Patients have been observed to survive bleed volumes below 140 mL, acutely, but secondary or delayed effects often compromise the health of the brain [36]. Experiments have shown that CBF around the ICH hematoma slightly decreases in flow but were not substantial enough to cause ischemia [36]. It is unlikely that ischemia will be observed in the tissue surrounding a hematoma unless intracranial pressure is high enough to cause the compression of blood vessels or cellular components, ultimately leading to cellular dysfunction and death.

Cytokines involved in inflammatory mediated signaling

After brain injury, whether ischemic or hemorrhagic, an inflammatory response is

immediately observed. Cytokines are one type of molecule that diffuses through the parenchyma and elicits an immune response. Cytokines are released by many cell types including microglia, macrophages, astrocytes, neurons, and endothelial cells found in the brain [37]. Furthermore, cytokines are also released by blood-borne cells such as leukocytes, which can enter through the blood-brain barrier after ICH. Tumor necrosis factor α and interleukin-1β are cytokines that are elevated after brain injury which are released neurons, astrocytes, leukocytes, and microglia/macrophages [38]. Both of these cytokines have been shown to exacerbate brain injury. In contrast, prostanoids are important regulators of inflammation after brain injury. Evidence has shown that microglia and astrocytes both produce prostaglandin-E_2 (PGE_2) after brain injury and provides a protective inflammatory role by inhibiting both microglia and macrophage production of proinflammatory cytokines [39].

Other diffusible molecules have been known to influence microglia and macrophages behavior after injury. For example, in some lesions, ATP is released with the highest concentrations closest to the site of injury. Microglia in the vicinity of the injury have been observed to polarize its processes towards higher concentrations of ATP [40]. These processes gravitate towards the lesion site within minutes and can remain for weeks. Another cytokine involved in inflammation after brain injury is the fractalkine (i.e., CX_3CL_1) which is primarily produced in neurons and signal microglia and macrophages by binding to the CX_3CR_1 receptor found only in microglia and blood-derived monocytes, after brain injury [41]. The fractalkine cytokine has been shown to polarize microglia processes and evoke migration of inflammatory cells towards the site of injury.

Blood components after ICH also contain cytokines and other molecules that signal microglia and macrophages to respond to injury. Thrombin, a serine protease, is found in blood and is immediately produced by the brain after ICH. Thrombin is an

essential component of the clotting cascade, but when found in the parenchyma it activates brain resident microglia and can lead to apoptosis of neurons and astrocytes [36]. Plasmin, another serine protein derived from plasminogen found in the microcirculation, is also pushed into the parenchyma after ICH. Plasmin near the ICH site has been detected in neurons and can lead to neurotoxicity and brain damage after injury when coupled with thrombin [42].

Astrocytes in the vicinity of brain injury react by swelling and can contribute to a mesh of astrocytic processes encasing the site of injury. Astrocytes produce GFAP after brain injury and are thought to have positive affects on the surrounding tissue. GFAP-knockout mice have exhibited a greater cortical infract, decreased cerebral blood flow, and an increase in cranial pressure after ischemic brain injury. In addition, these mice have also reported greater neuronal loss after ischemia; therefore astrocytes are thought to be responsible for the viability of neurons [43]. In addition, activated microglia produces various growth factors that stimulate astrocytes to increase production of nerve growth factor which promotes neuronal regeneration and minimizes tissue damage [43].

Inflammatory response after ICH

An inflammatory response by microglia, astrocytes, blood-borne macrophages and monocytes have been observed following ICH. Microglia are the only cells in the central nervous system to express the fractalkine (CX_3CR_1) receptor. The CX_3CL_1 chemokine is secreted by neurons and is a ligand to the CX_3CR_1 receptor on microglia and monocytes, thus recruiting both cell types to the site of injury [44]. Microglia response after ICH, using both whole blood and bacterial collagenase infusion models, leads to an increase in microglia activation and response as early as one to four hours after ICH onset and persists for several weeks after [37]. Neutrophils and macrophages

have also been observed to invade the site of the hemorrhage after infusion of whole RBCs [45]. In addition, astrocyte activation has been observed near the injury site within two days after ICH [36]. Microglia populations have been observed to massively increase near the lesion site, peaking several days after injury [46] in both large-scale ischemic models as well as smaller focal lesion injury models [40, 47].

Inflammatory response in other injuries

A similar inflammatory response is observed in other injury models such as open skull imaging preparations and certain neurodegenerative diseases. In an open craniotomy preparation, where a portion of skull is removed, microglia processes have been observed to polarize towards the exposed portion of the brain [48].

In another injury model where Aβ-plaques are present in the brain, microglia/macrophages migrate towards these plaques, increasing in numbers to phagocytose the Aβ-plaques. Benefits Aβ-plaque removal also leads to removal of nearby neurons, thus contributing to cellular death and perhaps functional deficits as a collateral consequence [49].

Microbleeds in the brain

Recent evidence using magnetic resonance imaging and post-mortem histology have revealed that small blood vessel ruptures in the brain can lead to bleeding and affect a small area of the brain approximately 0.2-mm to 5-mm in diameter, termed microbleeds [9, 50]. These microbleeds are 34% ischemic and 60% hemorrhagic. They are thought to lead to cellular dysfunction and ultimately contribute to cognitive decline, dementia, and neurological disorders [9, 50]. Microbleeds have been linked in the development of Alzheimer's disease (AD) pathology. One in five patients diagnosed with AD have accumulated numerous microbleeds. These patients typically display

severe cognitive impairment and a two-fold increase in mortality compared to AD patients without microbleeds [50]. Elevated iron and heme deposits near capillaries have been found in aged and diseased human brains and are thought to be the by-products of microbleeds [9].

Little is known about the physiological progression of microbleeds. They are typically found in patients after MRI scans, where numerous microbleeds have already impacted the brain. Clinical treatments for microbleeds can range from antithrombotic treatments such as warfarin and aspirin to thrombolysis drugs such as tissue plasminogen activator (tPA). Currently, physicians are unaware of any potential affects these treatments may have on the brain, such as the development of additional microbleeds or larger ICHs.

Microhemorrhages to a single penetrating arteriole

To better understand the physiological impact of microbleeds, we characterize the bleeding dynamics and track any pathology out to several weeks in chapter 5. These microbleeds are ruptures to single blood vessels in the cortex of the brain, we termed microhemorrhages. In vivo observations of ruptures to single blood vessels and their physiological consequences are difficult to observe due to the inability to induce a microhemorrhage at a specific location and time-point. Until recently, there was no method to selectively target and rupture a blood vessel with minimal collateral damage below the surface of the brain. The work presented in chapter 5 characterizes and discusses observed consequences due to a microhemorrhage of a single cortical blood vessel and uses the injury method established by Nishimura [51]. We used tightly focused femtosecond laser pulses to rupture single blood vessels in the cortex of the brain at anytime producing blood extravasation of approximately $5x10^{-4}$ mm^3 of densely packed RBCs and 0.2 mm^3 of blood plasma, 10,000 times smaller than other

ICH methods previously mentioned, but these lesion sizes are clinically relevant because they correspond in size to those seen post-mortem in patients [9].

REFERENCES

1. Giannakopoulos, P., Hof, P.R., Michel, J.P., Guimon, J. & Bouras, C. Cerebral cortex pathology in aging and Alzheimer's disease: a quantitative survey of large hospital-based geriatric and psychiatric cohorts. *Brain Res Brain Res Rev* **25**, 217-245 (1997).

2. Garcia, J.H. Experimental ischemic stroke: a review. *Stroke* **15**, 5-14 (1984).

3. Lutsep, H.L., *et al*. Clinical utility of diffusion-weighted magnetic resonance imaging in the assessment of ischemic stroke. *Annals of Neurology* **41**, 574-580 (1997).

4. Chiu, D., *et al*. Intravenous tissue plasminogen activator for acute ischemic stroke - Feasibility, safety, and efficacy in the first year of clinical practice. *Stroke* **29**, 18-22 (1998).

5. Vermeer, S.E., *et al*. Silent brain infarcts and the risk of dementia and cognitive decline. *N Engl J Med* **348**, 1215-1222 (2003).

6. Schmidt, W.P., *et al*. Functional and cognitive consequences of silent stroke discovered using brain magnetic resonance imaging in an elderly population. *J Am Geriatr Soc* **52**, 1045-1050 (2004).

7. Werring, D.J., *et al*. Cognitive dysfunction in patients with cerebral microbleeds on T2*-weighted gradient-echo MRI. *Brain* **127**, 2265-2275 (2004).

8. Fiehler, J. Cerebral microbleeds: old leaks and new haemorrhages. *International journal of stroke : official journal of the International Stroke Society* **1**, 122-130 (2006).

9. Cullen, K.M., Kocsi, Z. & Stone, J. Pericapillary haem-rich deposits: evidence for microhaemorrhages in aging human cerebral cortex. *J Cereb Blood Flow Metab* **25**, 1656-1667 (2005).

10. Zhang, S., Boyd, J., Delaney, K. & Murphy, T.H. Rapid reversible changes in dendritic spine structure in vivo gated by the degree of ischemia. *J Neurosci* **25**, 5333-5338 (2005).

11. Schaffer, C.B., *et al*. Two-photon imaging of cortical surface microvessels reveals a robust redistribution in blood flow after vascular occlusion. *PLoS Biol* **4**, e22 (2006).

12. Nishimura, N., Schaffer, C.B., Friedman, B., Lyden, P.D. & Kleinfeld, D.

Penetrating arterioles are a bottleneck in the perfusion of neocortex. *Proc Natl Acad Sci U S A* **104**, 365-370 (2007).

13. Kaufmann, A.M., *et al*. Ischemic core and penumbra in human stroke. *Stroke* **30**, 93-99 (1999).

14. Lenzi, G.L., Frackowiak, R.S.J. & Jones, T. Cerebral Oxygen-Metabolism and Blood-Flow in Human Cerebral Ischemic Infarction. *J Cerebr Blood F Met* **2**, 321-335 (1982).

15. Nagasawa, H. & Kogure, K. Correlation between Cerebral Blood-Flow and Histologic-Changes in a New Rat Model of Middle Cerebral-Artery Occlusion. *Stroke* **20**, 1037-1043 (1989).

16. Hossmann, K.A., Lechtape.H & Hossmann, V. Role of Cerebral Blood-Flow for Recovery of Brain after Prolonged Ischemia. *Z Neurol* **204**, 281-299 (1973).

17. Longa, E.Z., Weinstein, P.R., Carlson, S. & Cummins, R. Reversible Middle Cerebral-Artery Occlusion without Craniectomy in Rats. *Stroke* **20**, 84-91 (1989).

18. Shih, A.Y., *et al*. Active dilation of penetrating arterioles restores red blood cell flux to penumbral neocortex after focal stroke. *J Cerebr Blood F Met* **29**, 738-751 (2009).

19. Bolander, H.G., *et al*. Regional cerebral blood flow and histopathologic changes after middle cerebral artery occlusion in rats. *Stroke* **20**, 930-937 (1989).

20. Enright, L.E., Zhang, S.X. & Murphy, T.H. Fine mapping of the spatial relationship between acute ischemia and dendritic structure indicates selective vulnerability of layer V neuron dendritic tufts within single neurons in vivo. *J Cerebr Blood F Met* **27**, 1185-1200 (2007).

21. Zeng, Y.S. & Xu, Z.C. Co-existence of necrosis and apoptosis in rat hippocampus following transient forebrain ischemia. *Neurosci Res* **37**, 113-125 (2000).

22. Tomita, Y., *et al*. Long-term in vivo investigation of mouse cerebral microcirculation by fluorescence confocal microscopy in the area of focal ischemia. *J Cerebr Blood F Met* **25**, 858-867 (2005).

23. Stoll, G., Jander, S. & Schroeter, M. Inflammation and glial responses in ischemic brain lesions. *Progress in neurobiology* **56**, 149-171 (1998).

24. Mabuchi, T., *et al*. Contribution of microglia/macrophages to expansion of infarction and response of oligodendrocytes after focal cerebral ischemia in rats.

Stroke **31**, 1735-1742 (2000).

25. Broderick, J.P., Brott, T., Tomsick, T., Miller, R. & Huster, G. Intracerebral Hemorrhage More Than Twice as Common as Subarachnoid Hemorrhage. *Journal of neurosurgery* **78**, 188-191 (1993).

26. Terai, K., Suzuki, M., Sasamata, M. & Miyata, K. Amount of bleeding and hematoma size in the collagenase-induced intracerebral hemorrhage rat model. *Neurochem Res* **28**, 779-785 (2003).

27. MacLellan, C.L., Silasi, G., Auriat, A.M. & Colbourne, F. Rodent models of intracerebral hemorrhage. *Stroke* **41**, S95-98 (2010).

28. Ayata, C. CADASIL Experimental Insights From Animal Models. *Stroke* **41**, S129-S134 (2010).

29. Wakisaka, Y., Chu, Y., Miller, J.D., Rosenberg, G.A. & Heistad, D.D. Spontaneous intracerebral hemorrhage during acute and chronic hypertension in mice. *J Cereb Blood Flow Metab* **30**, 56-69 (2010).

30. Bailey, E.L., McCulloch, J., Sudlow, C. & Wardlaw, J.M. Potential animal models of lacunar stroke: a systematic review. *Stroke* **40**, e451-458 (2009).

31. Ruchoux, M.M.*, et al*. Transgenic mice expressing mutant Notch3 develop vascular alterations characteristic of cerebral autosomal dominant arteriopathy with subcortical infarcts and leukoencephalopathy. *Am J Pathol* **162**, 329-342 (2003).

32. Joutel, A. Pathogenesis of CADASIL Transgenic and knock-out mice to probe function and dysfunction of the mutated gene, Notch3, in the cerebrovasculature. *Bioessays* **33**, 73-80 (2011).

33. Matsushita, K.*, et al*. Evidence for apoptosis after intracerebral hemorrhage in rat striatum. *J Cerebr Blood F Met* **20**, 396-404 (2000).

34. Gong, C.*, et al*. Intracerebral hemorrhage-induced neuronal death. *Neurosurgery* **48**, 875-882 (2001).

35. Xi, G.*, et al*. Mechanisms of edema formation after intracerebral hemorrhage: effects of extravasated red blood cells on blood flow and blood-brain barrier integrity. *Stroke* **32**, 2932-2938 (2001).

36. Xi, G., Keep, R.F. & Hoff, J.T. Mechanisms of brain injury after intracerebral haemorrhage. *Lancet Neurol* **5**, 53-63 (2006).

37. Wang, J. & Dore, S. Inflammation after intracerebral hemorrhage. *J Cerebr*

Blood F Met **27**, 894-908 (2007).

38. Munoz-Fernandez, M.A. & Fresno, M. The role of tumour necrosis factor, interleukin 6, interferon-gamma and inducible nitric oxide synthase in the development and pathology of the nervous system. *Progress in neurobiology* **56**, 307-340 (1998).

39. Aloisi, F. Immune function of microglia. *Glia* **36**, 165-179 (2001).

40. Davalos, D.*, et al*. ATP mediates rapid microglial response to local brain injury in vivo. *Nat Neurosci* **8**, 752-758 (2005).

41. Hughes, P., Botham, M., Frentzel, S. & Mir…, A. Expression of fractalkine (CX3CL1) and its receptor, CX3CR1, during acute and chronic inflammation in the rodent CNS. *Glia* (2002).

42. Fujimoto, S.*, et al*. Plasminogen potentiates thrombin cytotoxicity and contributes to pathology of intracerebral hemorrhage in rats. *J Cerebr Blood F Met* **28**, 506-515 (2008).

43. Panickar, K.S. & Norenberg, M.D. Astrocytes in cerebral ischemic injury: Morphological and general considerations. *Glia* **50**, 287-298 (2005).

44. Tanaka, R.*, et al*. Migration of enhanced green fluorescent protein expressing bone marrow-derived microglia/macrophage into the mouse brain following permanent focal ischemia. *Neuroscience* **117**, 531-539 (2003).

45. Gong, C., Hoff, J.T. & Keep, R.F. Acute inflammatory reaction following experimental intracerebral hemorrhage in rat. *Brain Research* **871**, 57-65 (2000).

46. Ladeby, R.*, et al*. Microglial cell population dynamics in the injured adult central nervous system. *Brain research reviews* **48**, 196-206 (2005).

47. Walter, L. & Neumann, H. Role of microglia in neuronal degeneration and regeneration. *Semin Immunopathol* **31**, 513-525 (2009).

48. Xu, H.T., Pan, F., Yang, G. & Gan, W.B. Choice of cranial window type for in vivo imaging affects dendritic spine turnover in the cortex. *Nature neuroscience* **10**, 549-551 (2007).

49. Fuhrmann, M.*, et al*. Microglial Cx3cr1 knockout prevents neuron loss in a mouse model of Alzheimer's disease. *Nature neuroscience* **13**, 411-413 (2010).

50. Cordonnier, C. Brain microbleeds. *Pract Neurol* **10**, 94-100 (2010).

51. Nishimura, N., *et al*. Targeted insult to subsurface cortical blood vessels using ultrashort laser pulses: three models of stroke. *Nature Methods* **3**, 99-108 (2006).

CHAPTER FOUR

LIMITATIONS OF COLLATERAL FLOW AFTER OCCLUSION OF A SINGLE CORTICAL PENETRATING ARTERIOLE

Nozomi Nishimura[1,3], Nathanael L Rosidi[1,3], Costantino Iadecola[2] and Chris B Schaffer[1]

[1]Department of Biomedical Engineering, Cornell University, Ithaca, New York, USA

[2]Department of Neurology and Neuroscience, Weill Cornell Medical College, New York, New York, USA

[3]These authors contributed equally to this work.

This research was originally published in the Journal of Cerebral Blood Flow & Metabolism. This paper was reprinted with permission from the Nature Publishing Group. Nozomi Nishimura[1,3], Nathanael L Rosidi[1,3], Costantino Iadecola[2] and Chris B Schaffer[1]Limitations of collateral flow after occlusion of a single cortical penetrating arteriole. *Journal of Cerebral Blood Flow & Metabolism* **(2010)** 30, 1914–1927.

ABSTRACT

Occlusions of penetrating arterioles, which plunge into cortex and feeds capillary beds, cause severe decreases in blood flow and are potential causes of ischemic microlesions. However, surrounding arterioles and capillary beds remain flowing and might provide collateral flow around the occlusion. We used femtosecond laser ablation to trigger clotting in single penetrating arterioles in rat cortex and two-photon microscopy to measure changes in microvessel diameter and red blood cell speed after the clot. We found that after occlusion of a single penetrating arteriole, nearby penetrating and surface arterioles did not dilate, suggesting that alternate blood flow routes are not actively recruited. In contrast, capillaries showed two types of reactions. Capillaries directly downstream from the occluded arteriole dilated after the clot, but other capillaries in the same vicinity did not dilate. This heterogeneity in capillary response suggests that signals for vasodilation are vascular rather than parenchymal in origin. Although both neighboring arterioles and capillaries dilated in response to topically applied acetylcholine after the occlusion, the flow in the territory of the occluded arteriole did not improve. Collateral flow from neighboring penetrating arterioles is neither actively recruited nor effective in improving blood flow after the occlusion of a single penetrating arteriole.

INTRODUCTION

In the healthy brain, the cerebral vasculature is highly regulated and demonstrates an impressive capacity to control the distribution of blood flow with spatial and temporal precision. For example, the brain vasculature can reroute flow toward specific groups of active neurons as small as a single cortical column (Attwell and Iadecola, 2002). This neurovascular coupling has important scientific and clinical implications because it provides the basis for localizing normal and abnormal brain function using methods such as functional magnetic resonance imaging (Ogawa et al, 1990). The neocortex in both rodents and humans has an interconnected network of surface arterioles that consists of many loops (Blinder et al, 2010; Schaffer et al, 2006; Vander Eecken and Adams, 1953). To feed the capillaries within the cortex, penetrating arterioles branch off surface arterioles and plunge perpendicularly into the brain. It has been suggested that this combination of a highly redundant network of surface arterioles and nonredundant penetrating arterioles might serve to facilitate rerouting of flow from one region to another (Nishimura et al, 2007). Such a network might provide a mechanism for flow redistribution not only during normal neurovascular coupling but also in response to vascular occlusions. In experimental models of occlusion of large cerebral arteries, such as the middle cerebral artery (MCA), acute (Belayev et al, 2002; Shih et al, 2009; Tomita et al, 2005; Wei et al, 1998) and chronic (Coyle and Heistad, 1987) dilation of cortical arteries and arterioles has been observed, suggesting that a mechanism for compensatory collateral flow is activated. However, it is not known whether such compensatory routing mechanisms are activated after occlusions of

smaller vessels such as penetrating arterioles.

Cortical microinfarcts, 400 to 500 mm in size, presumably resulting from occlusion of single cortical arterioles, have been recognized as a prevalent cause of focal neurologic deficits as well as cognitive impairment (Kovari et al, 2004; Vermeer et al, 2003). However, the hemodynamic mechanisms underlying such lesions are poorly understood. Recent developments in optical techniques enable the occlusion of only a single segment of an arteriole or capillary (Nishimura et al, 2006, 2007; Schaffer et al, 2006). These methods, in combination with two-photon excited fluorescence (2PEF) microscopy, provide the tools to study the changes in blood flow and role of active vascular regulation after an occlusion at the level of single microvessels. Experiments with clots in surface arterioles established that there is great redundancy in the surface arteriole network, which provides alternate routes for blood flow around the occluded vessel (Schaffer et al, 2006). In contrast, occlusions in penetrating arterioles, which have little redundancy, result in severe decreases in capillary blood flow in a region ~500mm in diameter (Nishimura et al, 2007), indicating that existing collateral flow is limited. However, it is not known whether the capacity for compensatory flow has been maximized or if additional compensation by vessel dilation might be possible.

In this study, we sought to determine whether the vasculature surrounding an occluded penetrating arteriole is recruited to provide collateral flow to alleviate blood flow decreases. First, we examined whether occlusion of a penetrating arteriole causes active vasodilation in the neighboring penetrating and surface arterioles similar to the dilation observed after occlusion of larger cerebral vessels. Surprisingly, we found no

such response. We then examined the effect of the occlusion on the diameter and flow in capillaries around the occluded vessel and found that the only capillaries to dilate were those directly downstream from the occluded vessel; these capillaries also slowed drastically as a result of the clot. Finally, we examined whether the capillary blood flow in the territory of the occluded arteriole could be improved by forcing the neighboring arterioles to dilate, but found that although applying a vasodilator leads to overall increases in flow, it does not resolve the severe blood flow decreases in capillaries downstream from the clot.

METHODS

Surgical Preparation

All animal procedures were approved by Cornell University Institutional Animal Care and Use Committee. Fifty-nine male Sprague-Dawley rats (Harlan, Inc, South Easton, MA, USA), ranging from 200 to 400g in weight were used in the experiments. Glycopyrrolate (50 mg/100 g rat) was injected intramuscularly to facilitate respiration. Rats were anesthetized by 5% isoflurane and maintained at 1.5% to 2%. Body temperature was kept constant at 37.51C, with a heating blanket controlled by rectal thermometer (50 to 7053P; Harvard Apparatus, Holliston, PA, USA). A pulse oximeter (MouseOx; Starr Life Sciences Corp., Oakmont, PA, USA) clipped to the hind paw of the rat was used to monitor blood oxygen saturation and heart rate. A local anesthetic,bupivacaine (0.1 mL, 0.125%), was administered at each incision site. The femoral artery was cannulated to monitor blood pressure (BP-1; World Precision Instruments, Sarasota, FL, USA). A tracheotomy was performed to allow intubation for artificial ventilation (SAR-830/P; CWE Inc, Ardmore, PA, USA) and to monitor exhaled carbon dioxide levels (Capstar-100; CWE Inc). Ventilation rates and breath volumes were adjusted to maintain stable end-tidal carbon dioxide. Rats were ventilated with a mix of medical air and the minimum amount of oxygen needed to maintain a minimum arterial blood oxygen saturation of ~95%. Physiological parameters were recorded throughout the experiments to ensure that physiological variables stayed the same during the multiple stages of each imaging session (Supplementary Table 4.1). Rats were also given 5% (wt/vol) glucose in physiological saline (0.1 mL/100 g rat) subcutaneously every hour to maintain hydration. An ~3 x

6-mm^2 craniotomy was performed over the parietal cortex and the dura was removed. Tubing (inner diameter: 0.25 mm, outer diameter: 0.76 mm; Microbore, Tygon, Shanghai, China) was glued at the edge of the craniotomy to allow perfusion of artificial cerebrospinal fluid (ACSF) (Kleinfeld and Delaney, 1996) and acetylcholine (ACh). An 8-mm, No. 1.5 glass cover slip (50201; World Precision Instruments) was then glued over the exposed brain using cyanoacrylate and dental cement (Lang Dental Mfg Co, Wheeling, IL, USA and Co-Oral-Ite Dental Mfg Co., Diamond Springs, CA, USA). The lateral edge of the craniotomy was left without glue, but covered in 1.5% agarose (A9793; Sigma, St Louis, MO, USA) in ACSF to allow for drainage of ACSF and the ACh solution while preventing exposure of the cortex to outside air. In most experiments (n = 47), rats were gradually transitioned off of isoflurane and onto urethane (1.5g/kg (U2500; Sigma)) administered by intraperitoneal injection. Imaging was started 30minutes after urethane administration. In some experiments (n=12), rats were kept on isoflurane for the entire duration of the experiment. The vasculature was visualized by intravenously injecting 0.3mL of 5% (wt/vol) solution of 2-MDa fluorescein- conjugated dextran (FD2000S; Sigma) in physiological saline.

Two-Photon Excited Fluorescence Microscopy of Cerebral Vasculature

In vivo vascular measurements were made with a custom- built 2PEF microscope using 800-nm, 87-MHz, 100-femtosecond pulses from a Ti:sapphire laser oscillator (MIRA HP; Coherent, Santa Clara, CA, USA), pumped by a continuous wave laser (Verdi-V18; Coherent, Santa Clara, CA, USA). Laser pulses were prechirped to

compensate for dispersion in the microscope with a prism-based compressor (Muller et al, 1998). Laser scanning and data acquisition was con- trolled by MPScope software (Nguyen et al, 2006). Images spanning the entire cranial window were taken using a 0.28 numerical aperture x4 air objective (Olympus, Center Valley, PA, USA). For high-resolution imaging, red blood cell (RBC) speed measurements, vessel diameter measurements, and vascular lesioning, we used a 0.95-numerical aperture, x20, water immersion objective (Olympus).

To map and categorize the arterioles, capillaries, and venules in the area around the target vessel, stacks of images spaced 1 mm axially were obtained (Supplementary Text). To measure vessel diameter, we recorded images of individual vessels stepping from above to below the vessel, accumulating at least 20 image frames (~6seconds). For surface and penetrating arterioles, these frames were axially projected, guaranteeing a measurement across the thickest (middle) portion of the vessel. Diameters were calculated by manual selection of a region of interest that included the vessel segment to be measured. The area above threshold (20% of maximum intensity in the projection) was divided by the length of the measured area to yield an average measure of diameter across a 10 to 50-mm segment. For capillaries, because the motion of the brain made averaging frames impractical, diameters were measured from ~5 to 10 individual frames in which the motion appeared to be minimal and then averaged.

To quantify centerline RBC velocity in individual vessels, linescan measurements were obtained by scanning single vessels at a line rate of 1.7 kHz for 40 seconds and extracting the average speed over this period (Kleinfeld et al, 1998;

Schaffer et al, 2006). In these measurements, the scan is aligned along the vessel axis, which produces diagonal dark streaks in the resulting space-time image due to moving RBCs (which exclude the intravenously injected dye), with the slope of the streaks inversely proportional to the RBC velocity. Slope is calculated with an automated image-processing algorithm (Kleinfeld et al, 1998; Schaffer et al, 2006). In arterioles, RBC flow (volume of RBCs/time) was taken to be proportional to the product of the centerline RBC velocity and the cross-sectional vessel area, so we calculated the ratio of flow in a vessel before and after an occlusion as

$$\frac{Flow_{RBC,post}}{Flow_{RBC,pre}} = \frac{R_{post}^2 v_{post}}{R_{pre}^2 v_{pre}}$$

where v is the centerline RBC speed and R is the vessel radius. The proportionality constant depends on the exact shape of the dependence of RBC speed and hematocrit on radial position in the vessel. We assume this proportionality constant does not change between baseline and later measurements in the same vessel, and thus cancels out in the ratios reported here (Supplementary Text). In penetrating arterioles, RBC velocity and vessel diameter were measured in the portion of the vessel that ran parallel to the cortical surface proximal to where the arteriole dove into the brain. In capillaries, RBCs must travel nearly single file so we report RBC speed and RBC flux (number of RBCs/time) (Supplementary Text). Images and linescans were taken in the same vessels about 1hour before and after penetrating arteriole occlusion. Approximately 10 to 25 vessels were measured in each animal. Following postocclusion measurements, ACh (A9101; Sigma; 10 mmol/L in ACSF) (Park et al,

2008) was topically applied to the neocortex in some animals. Vessels were remeasured starting 10 minutes after topical application of ACh.

Penetrating Arteriole Occlusion by Femtosecond Laser Ablation

Occlusions of penetrating arterioles were produced by damaging the endothelium of targeted vessels using tightly focused femtosecond laser pulses, leading to localized clotting of the vessel (Nishimura et al, 2006). Vessels were irradiated with 50 femtosecond, ~0.1 to 2-mJ pulses from a 1-kHz pulse train produced by a Ti:sapphire regenerative amplifier (Legend 1k USP; Coherent) pumped by a Q-switched laser (Evolution 15; Coherent) and seeded by a Ti:sapphire oscillator (Chinhook Ti:sapphire laser; Kapteyn-Murnane Laboratories Inc, Boulder, CO, USA; pumped by Verdi-V6; Coherent, Inc) (Nishimura et al, 2006). The imaging and ablation beams were combined using a polarizing beam splitter located just after the scan mirrors of the 2PEF microscope and were focused in the same plane. The energy was varied with neutral density filters and the number of pulses deposited on the targeted vessel was controlled by a mechanical shutter with 2milliseconds minimum opening time (VMM-D4; Uniblitz, Rochester, NY, USA). During imaging with 2PEF microscopy, the amplified beam was focused in the lumen of the targeted penetrating arteriole in the segment below the surface but proximal to the first capillary branch off the arteriole. To minimize possible collateral damage, we began irradiation with one pulse using an energy that is below the expected damage threshold (~100nJ at about 100-mm depth). Next, the number of pulses was increased by factors of 10 up to 1,000 pulses with the same energy, often trying each pulse number a few times while watching for signs of

vessel damage. The pulse energy was gradually increased by ~25%, and the sequence of increasing pulse number was repeated until some extravasation of fluorescently labeled blood plasma outside the vessel lumen was observed. Once extravasation occurred, multiple nearby areas along the inner wall of the arteriole segment were irradiated with this laser energy and pulse number. Irradiation was continued until RBC motion as visualized in the segment of the penetrating arteriole at the surface of the cortex was stalled. If the occlusion recanalized, irradiation was repeated until the target vessel stopped flowing. Only one occlusion was produced per animal. As an alternative method for producing occlusions, we use photothrombotic clotting (4/59 rats) (Supplementary Text) (Nishimura et al, 2007; Schaffer et al, 2006; Sigler et al, 2008; Watson et al, 1985).

Statistical Analysis

Distributions were nonnormal, so nonparameteric statistical tests were necessary. To compare the effects of different anesthetics and other parameters such as occlusion method or vessel type (Figures 4.1F–1H, 4.2A–2C, 4.2G–2I) two-way analysis of variance (ANOVA) on ranks was used (JMP Statistical Software, SAS Institute Inc, Cary, NC, USA). When this yielded significant differences (Figure 4.1F) or when multiple comparisons analysis was not necessary (Figures 4.4A and 4.4B), we compared pairs of groups with the Wilcoxon–Mann–Whitney ranks sum test. Whenever measurements were made in two instances in the same vessels, the more powerful Wilcoxon rank sign test for paired data was used (Figures 4.6A and 4.6C). The significance of trends dependent on topological separation from the targeted

arteriole was tested with Cuzick's trend test (Cuzick, 1985) (Stats Direct, Altrincham, Cheshire, UK), which is a variant of the Wilcoxon tests (Figures 4.2A–4.2C, 4,4A, 4.4B, 4.6B, and 4.6C). A P value of < 0.05 was considered statistically significant for all tests. Matlab was used to generate box plots and trend lines as a function of spatial distance (details in Supplementary Text). We used G*Power (Faul et al, 2007) for post hoc power analysis using the Wilcoxon–Mann– Whitney test to compare two groups and the Wilcoxon signed-rank test in cases where we had matched pairs (Supplementary Text). Sensitivity was also calculated with G*Power. In all cases, we used $\alpha = 0.05$. A summary of all raw data is given in the Supplementary Information.

RESULTS

The RBC speed and vessel diameter changes caused by penetrating arteriole occlusions were measured in neighboring penetrating and surface arterioles as well as in nearby capillaries in anesthetized, adult, male, Sprague-Dawley rats. We used 2PEF microscopy to image cortical vasculature labeled with intravenously injected fluorescein dextran through closed cortical windows (Figure 4.1A). Occlusions were produced by focusing femtosecond-duration laser pulses (0.1 to 2-mJ energy) onto the descending segment of a penetrating arteriole just above the first downstream branch (Figures 4.1B and 4.1C). Nonlinear absorption of laser energy injures the vessel wall and triggers clotting (Nishimura et al, 2006). Before and after occlusion of a single penetrating arteriole, lumen diameter, and RBC speed were measured with 2PEF microscopy in neighboring arterioles (Figures 4.1D and 4.1E) and capillaries (Figure 4.3). The targeted and neighboring penetrating arterioles had similar sizes and speeds (Supplementary Figure 4.1). Separate animals in which no occlusions were induced with only a matched time delay between vessel measurements were used as controls. We found that the active dilatory responses of neighboring arterioles and nearby capillaries after occlusion of a single penetrating arteriole were strikingly different.

Occlusion of a Single Penetrating Arteriole Does Not Initiate Dilation in Neighboring Arterioles

We found no evidence for active vasodilation in neighboring arterioles in response to a penetrating arteriole occlusion (Figures 4.1D and 4.1F). As vasoactivity can be altered

by anesthesia, we performed the measurements using either urethane (19 occlusions and 12 controls) or isoflurane (7 occlusions and 3 controls) anesthesia during vessel measurements and clot formation (Figures 4.1F–4.1H). Rather than dilating, neighboring penetrating arterioles constricted slightly after occlusion (Figure 4.1F; two-way ANOVA on ranks, $P = 0.041$). Post hoc sensitivity analysis showed that we should have been able to resolve a 5% increase in diameter under urethane and a 12% increase under isoflurane with a statistical power of 0.8 (Supplementary Text), suggesting that any vasodilation after a penetrating arteriole occlusion is less than these values. We observed a slight, but not statistically significant, drop in both RBC speed and in RBC flow in neighboring penetrating arterioles after the occlusion, indicating that blood flow to the area surrounding the occlusion was mildly decreased (Figure 4.1G and 4.1H; two-way ANOVA on ranks $P=0.26$ and $P=0.16$).

To rule out the possibility that nearby or closely connected penetrating arterioles responded differently than distant arterioles, we categorized neighboring penetrating arterioles by the topological separation (i.e., number of vessel branches) and spatial distance from the occluded arteriole. We found no dependence of changes in vessel diameter, RBC speed or RBC flow on topological separation (Figures 4.2A–4.2C; Cuzick's trend test, $P > 0.14$), indicating that vessels closely or distantly connected to the occluded arteriole are equally unaffected by the occlusion. Similarly, changes in vessel diameter, RBC speed or RBC flow did not depend on the spatial distance between the vessel and the occluded arteriole (Figures 4.2D–4.2F). In addition to no dilation in the penetrating arterioles that dive into the brain tissue to feed capillaries, we found that communicating arterioles that stay on the cortical

surface and serve as conduits to more distal regions of brain also did not dilate after a penetrating arteriole occlusion (Figure 4.2G, two-way ANOVA on ranks, $P = 0.4$). Communicating arterioles decreased slightly in both velocity and RBC flow after the clot, but did not differ significantly from penetrating arterioles (Figures 4.2H and 4.2I; two-way ANOVA on ranks, $P = 0.5$ for both). Finally, we tried an alternate clotting method based on photochemical thrombosis with rose bengal, and again found no dilation in neighboring penetrating arterioles (Supplementary Text; Supplementary Figure 4.2). In all these experiments, urethane and isoflurane anesthetics generated similar results.

Figure 4.1 Diameter and flow changes in neighboring penetrating arterioles after the occlusion of a single penetrating arteriole. (A) Average projection of a low-magnification two-photon excited fluorescence (2PEF) image stack of rat cortical surface vasculature with arterioles traced in red. Montages (Panavue Image Assembler) of average projections of 2PEF image stacks through 250 mm of cortical vasculature before (B) and after (C) clotting of a single penetrating arteriole by femtosecond laser irradiation (yellow circle). Images were median filtered. (D) Baseline vessel lumen diameter and diameter after penetrating arteriole clot as a percentage of the baseline diameter. (E) Baseline average centerline red blood cell speed and speed after penetrating arteriole clot as a percentage of baseline speed. Location of (B–E) is marked by box in (A). Aggregate diameter (F), centerline RBC speed (G), and RBC flow (H) in neighboring penetrating arterioles after occlusion of a single penetrating arteriole (or equivalent time delay only in controls), expressed as a percentage of the baseline value. Each point represents a measurement in a single neighboring penetrating arteriole. In (F), the diameter is significantly smaller in the clot experiments as compared with the control experiments under urethane anesthesia (Wilcoxon–Mann–Whitney ranks sum test after two-way analysis of variance on ranks, $P = 0.012$), although the magnitude of this difference is small. Some data points were off the scale of the plot: (G) 427% in urethane control experiments, 267%, 369%, 289%, 292% in isoflurane control experiments, (H) 296% and 353% in isoflurane clot experiments and 1,114%, 260%, 556%, 540%, 475%, 817%, 568%, 371% in isoflurane control experiments.

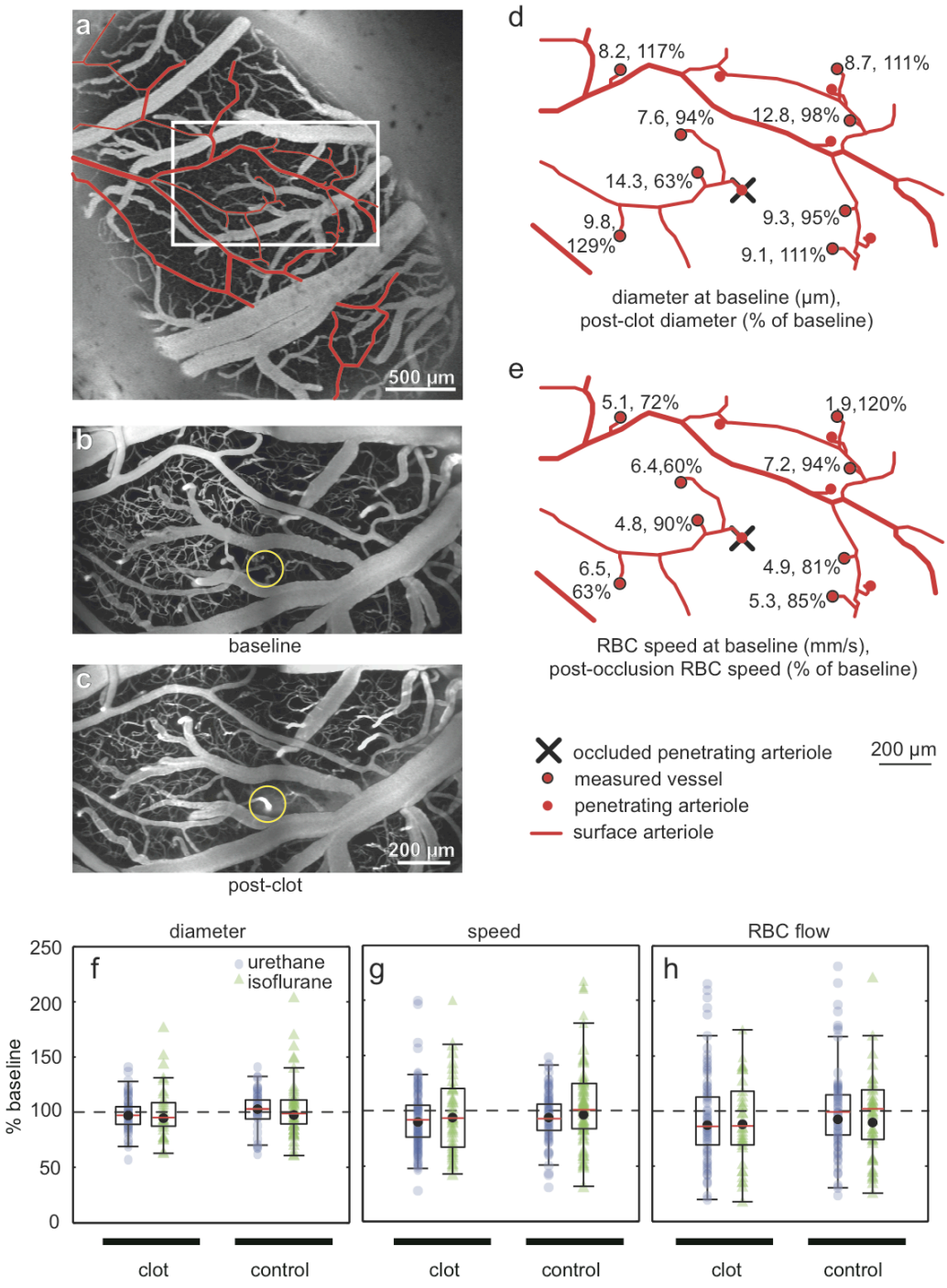
a
500 µm
b
baseline
c
200 µm
post-clot
d
8.2, 117%
8.7, 111%
7.6, 94%
12.8, 98%
14.3, 63%
9.8, 129%
9.3, 95%
9.1, 111%
diameter at baseline (µm),
post-clot diameter (% of baseline)
e
5.1, 72%
1.9,120%
6.4,60%
7.2, 94%
4.8, 90%
6.5, 63%
4.9, 81%
5.3, 85%
RBC speed at baseline (mm/s),
post-occlusion RBC speed (% of baseline)
occluded penetrating arteriole
measured vessel
penetrating arteriole
surface arteriole
200 µm
diameter
speed
RBC flow
f
g
h
urethane
isoflurane
% baseline
250
200
150
100
50
0
clot
control
clot
control
clot
control

Figure 4.2 Topology and distance dependence of diameter and flow changes in the neighboring penetrating arterioles after single penetrating arteriole occlusion. Diameter (A), centerline red blood cell (RBC) speed (B), and RBC flow (C) in neighboring penetrating arterioles after a single penetrating arteriole clot, expressed as a percentage of the baseline value, as a function of the number of vessel branches separating the measured and occluded vessels. No significant differences ($P > 0.70$) were detected by two-way analysis of variance on ranks in A–C. Dependence of postclot diameter (D), RBC speed (E), and RBC flow (F) in neighboring penetrating arterioles, expressed as a percentage of the baseline value, on the distance to the occluded vessel. Solid lines show a running median with 95% confidence intervals indicated by shaded areas. Each point represents a single vessel measurement. Comparison of penetrating and communicating arteriole diameter (G), RBC speed (H), and RBC flow (I) after penetrating arteriole occlusion. Outliers not shown in (H) are 264% and 292% for the communicating arteriole, urethane velocity measurements; (I) 296% and 353% penetrating arteriole, isoflurane RBC flow, 627% communicating arteriole, urethane RBC flow, and 347% and 442% communicating arteriole, isoflurane RBC flow.

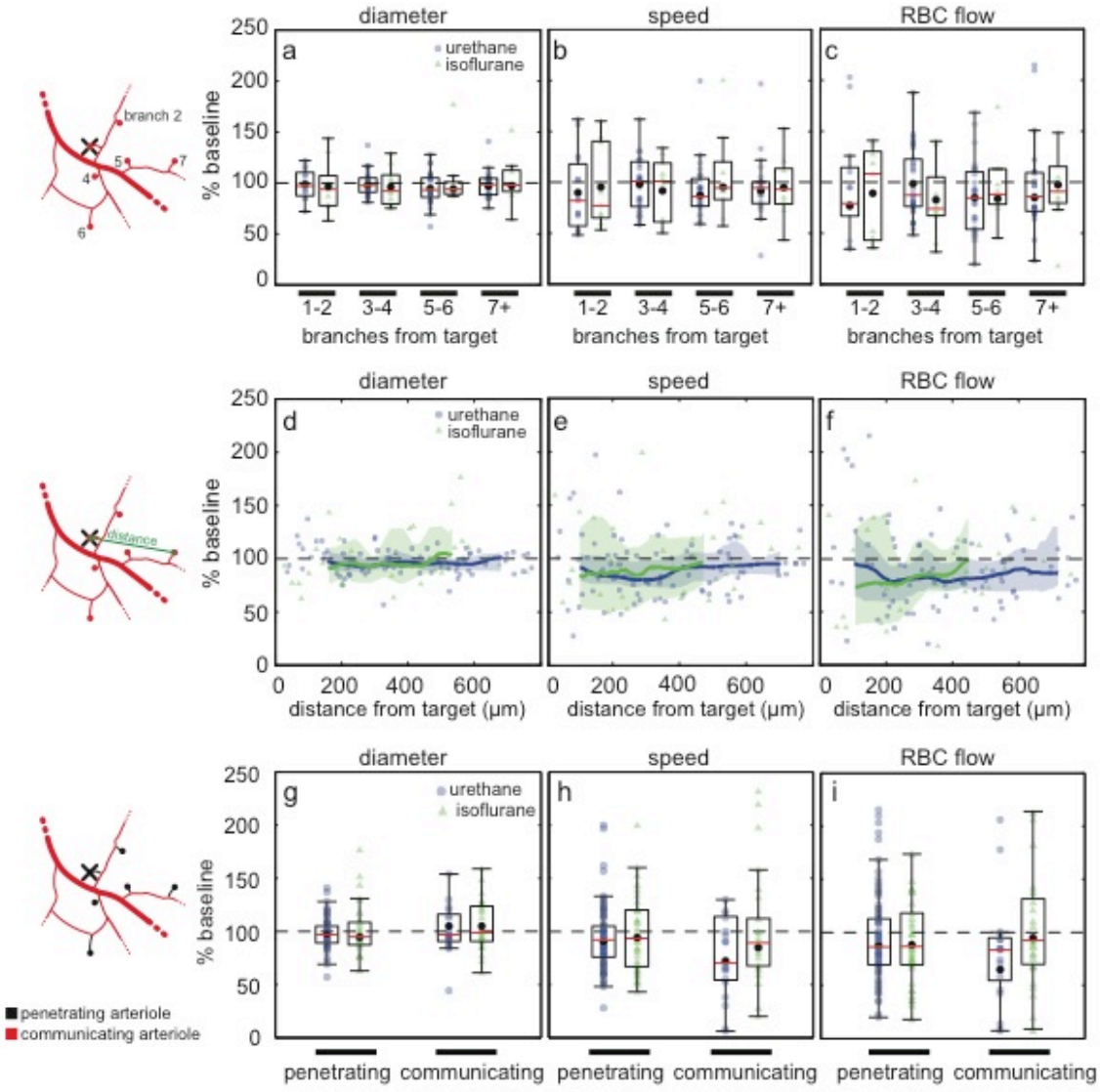
diameter
speed
RBC flow
a
b
c
urethane
isoflurane
% baseline
250
200
150
100
50
0
branch 2
4
5
6
7
1-2
3-4
5-6
7+
branches from target
d
e
f
distance
0
200
400
600
distance from target (μm)
g
h
i
penetrating arteriole
communicating arteriole
penetrating
communicating

Capillaries Immediately Downstream from an Occluded Penetrating Arteriole Dilated and Slowed Dramatically

A majority of the oxygen and nutrient exchange occurs in the subsurface vessels, so we measured vessel diameter and RBC speed in parenchymal capillaries before and after occlusion of a single penetrating arteriole (Figure 4.3). We used only urethane for these measurements because the two anesthetics showed similar behavior in arterioles. We found a highly heterogeneous mix of diameter and speed changes in nearby capillaries after a penetrating arteriole occlusion. In the example of Figure 4.3, the immediate vicinity of the occluded penetrating arteriole included capillaries p10 branches from the target (red in Figure 3B) and capillaries that we were unable to trace back to the target arteriole or were traced back to other arterioles (orange in Figure 4.3B). One capillary (marked with * in Figures 4.3D and 4.3E) was five branches away from both the target vessel and a neighboring penetrating arteriole. Note that the blood flow in this capillary was originally from the target vessel, but after the occlusion (Figure 4.3C), this vessel reversed direction and supplied flow from the neighboring unoccluded penetrating arteriole. Despite this source of collateral flow, there were large decreases in RBC speed in the majority of the vessels p10 branches away from the occluded arteriole (Figure 4.3D). Interestingly, nearly all of these vessels dilated (Figure 4.3E).

Figure 4.3 Flow and diameter changes in capillaries after penetrating arteriole occlusion. (A) Rendering of two-photon excited fluorescence microscopy image stack of fluorescently labeled vasculature using Voxx (Clendenon et al, 2002). A rotating movie of this image stack is shown in the Supplementary Movie. Surface arterioles are marked in red and the venules are marked in blue. Yellow oval indicates the target penetrating arteriole. (B) Average projection of image stack before the occlusion through volume marked with yellow box in (A), with a subset of capillaries traced. Red vessels were connected to the targeted penetrating arteriole in p10 branches. Orange vessels did not have any observable connections to the target arteriole. (C) Projection of same volume after occlusion of the penetrating arteriole (yellow oval in A). Extravasation of fluorescently labeled blood plasma is visible around the occluded arteriole and also along capillaries branching off of the clotted vessel. (D) Red blood cell velocity, expressed as a percentage of the baseline value, after occlusion of the penetrating arteriole marked with an X. Arrowheads indicate direction of flow with blue arrows and negative numbers, indicating a reversal in direction after the occlusion. Vessel indicated with an asterisk was five branches away from an unoccluded neighboring penetrating arteriole. (E) Postclot vessel diameter expressed as a percentage of the baseline value. Average projections (B, C) were median filtered.

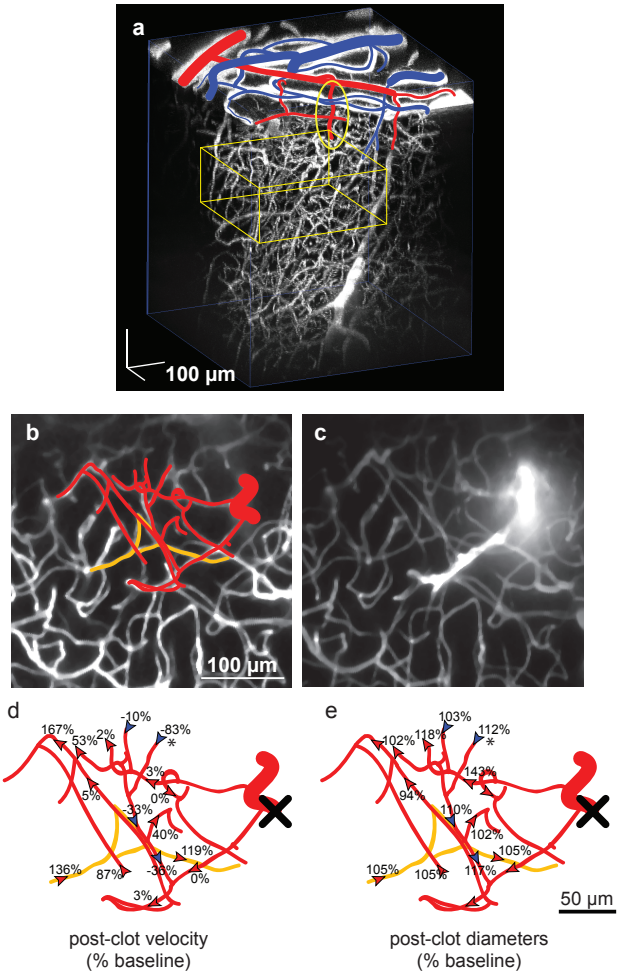

post-clot velocity
(% baseline)

post-clot diameters
(% baseline)

Changes in capillary diameter and RBC speed after a penetrating arteriole clot depended strongly on the topological separation between the capillary and the occluded vessel. We categorized each measured capillary by the number of branches that separate it from the trunk of the target vessel (Figure 4.4A, inset), or the nearest penetrating arteriole for controls. After occlusion of a penetrating arteriole, median RBC speed slowed to 1% (4%) of the baseline speed for capillaries one to two (three to four) branches downstream from the clot (Figure 4.4A). The amount of slowing decreased with increased topological separation from the clotted vessel (Cuzick's trend test, $P < 0.0001$), with no statistically significant slowing, relative to controls, in vessels more than four branches downstream. Capillaries one to two (three to four) branches downstream from the clot dilated to a median of 113% (110%) of baseline diameter after a penetrating arteriole clot (Figure 4.4B). The amount of dilation decreased further down- stream from the clotted vessel (Cuzick's, $P < 0.0001$), with no statistically significant dilation, relative to controls, more than four branches downstream (Figure 4.4B). Tube hematocrit remained unchanged after the occlusion for capillaries at all topological separations from the clotted arteriole (Supplementary Text; Supplementary Figure 4.3).

For capillaries with the same topological separation from the clotted vessel, the dilation and RBC speed decrease did not depend on the distance of the capillary from the occluded vessel. Vessels categorized as closely connected to the occluded penetrating arteriole (four or fewer branches downstream) slowed to a median speed of 2% of baseline.

Figure 4.4 Dependence of capillary diameter and blood flow changes after penetrating arteriole occlusion on topological separation and spatial distance from the clotted vessel. (A, inset) Capillaries were categorized by the number of branches from the trunk of the occluded penetrating arteriole or, in the case of controls, from the trunk of the nearest penetrating arteriole. (A) Postclot red blood cell (RBC) speed, expressed as a percentage of baseline, in capillaries after penetrating arteriole occlusion or time delay only (controls). (B) Postclot diameter, expressed as a percentage of baseline. Points not shown in (A) are clot/baseline: (5 to 6 branches, 284%), (> 10, 543%); control/baseline: (3 to 4, 265%), (7 to 10, 288%), (> 10, 537%). Dependence of RBC speed (C) and diameter (D) after penetrating arteriole clot on distance from the occluded vessel. Red (blue) indicates vessels 1 to 4 (> 4) branches away from the occluded penetrating arteriole. Bold lines are running medians with 95% confidence intervals indicated by shading. Black line in (C) is a running median of all capillaries. Two outliers in (C) not shown (> 4 branches, 170 mm, 284%; > 4 branches, 73 mm, 543%). Curly brackets indicate significant differences detected with Wilcoxon–Mann–Whitney ranks sum test.

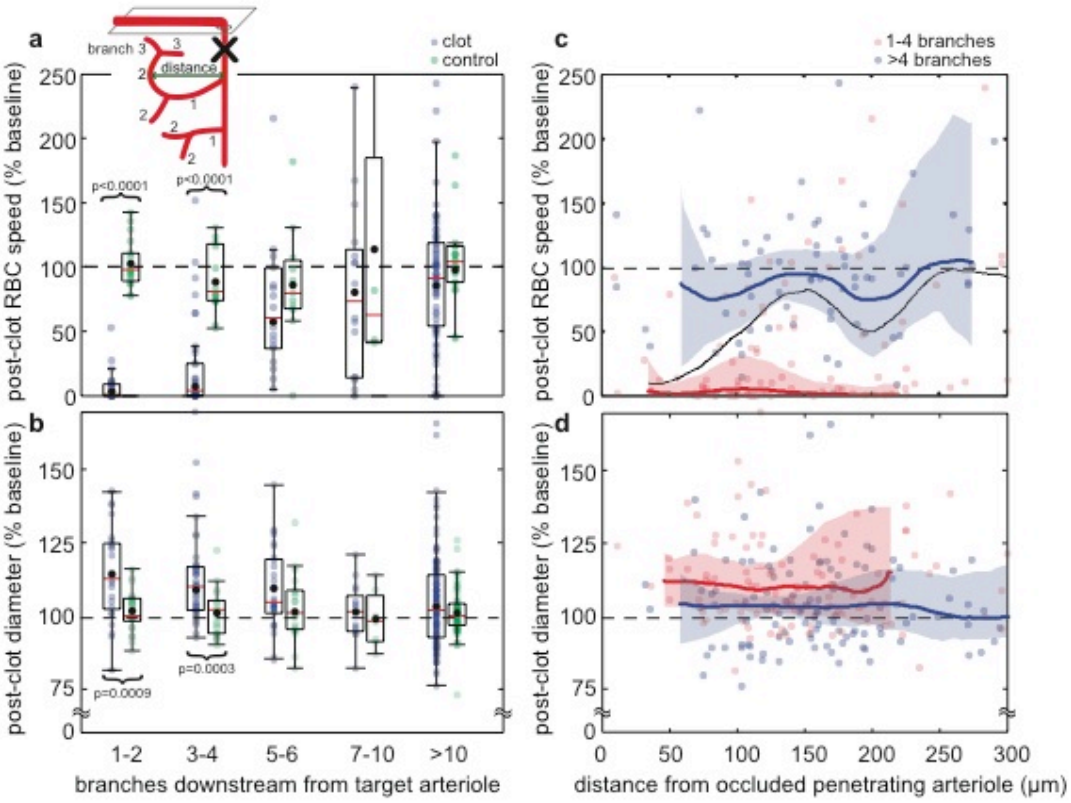
a
b
c
d
clot
control
1-4 branches
>4 branches
branch 3
distance
p<0.0001
p<0.0001
p=0.0009
p=0.0003
post-clot RBC speed (% baseline)
post-clot diameter (% baseline)
1-2
3-4
5-6
7-10
>10
branches downstream from target arteriole
distance from occluded penetrating arteriole (μm)

The speed was relatively constant for these closely connected capillaries in a 250-mm radius region around the occluded penetrating arteriole (red in Figure 4.4C). Distantly connected vessels (more than four branches downstream), however, remained at baseline speeds regardless of their distance from the clotted arteriole. If topological separation is ignored, the median capillary blood flow speed was severely decreased near the occluded vessel and returned to baseline over 300mm (black line in Figure 4.4C), confirming previous experiments that used a different clotting method based on photochemical inter- actions to form occlusions (Nishimura et al, 2007). This gradual increase in postclot blood flow speed with distance is consistent with the decrease in the number of closely connected vessels with distance (Supplementary Text; Supplementary Figure 4.4). Diameter changes also showed little dependence on lateral distance from the occluded vessel, when capillaries are segregated into closely and distantly connected groups (Figure 4.4D). Uniformly over a 250-mm radius region around the occluded vessel, closely connected vessels dilated to a median diameter of 111% of baseline, whereas distantly connected vessels did not dilate.

We asked whether the amount of dilation after a penetrating arteriole occlusion depended on the amount of reduction in RBC speed. We plotted the postclot diameter versus postclot speed, each as a percentage of baseline, for all penetrating arterioles (Figure 4.5A) and capillaries (Figure 4.5B), including both clot and control measurements. The penetrating arteriole measurements, both clot and control, grouped into a single distribution that showed no change, on average, in either speed or diameter (Figure 4.5A). In the capillaries, categorization into two groups by k-means

clustering (Matlab) revealed one cluster that slowed drastically and dilated (red in Figure 4.5B). In the second cluster (blue in Figure 4.5B), average speed and diameter did not change, similar to the behavior of the arterioles. This second cluster contained 91% of the control capillaries. The capillaries from clot experiments in these two clusters differed in their topological separation from the occluded penetrating arteriole (Kolmogorov– Smirnov test, $P<0.0001$), with the slowed and dilated group including more capillaries that were fewer branches from the occlusion (Figure 4.5B, inset). For example, 88% of capillaries four or fewer branches downstream from an occluded penetrating arteriole were in the slowed and dilated cluster. The difference in the cumulative probability of being in the slowed and dilated cluster vs. the unchanged cluster was largest at four branches downstream from the occlusion (Figure 4.5B, inset), indicating that vessels one to four branches downstream responded, on average, differently from those more than four branches downstream.

The slowed, dilated capillaries appeared to be spatially intermingled with unaffected capillaries. The clustering analysis suggested that closely connected capillaries (four or fewer branches downstream from an occluded penetrating arteriole) tended to belong to the slowed and dilated group, whereas distantly connected capillaries (more than four branches down- stream) belonged to the unchanged group (Figure 4.5B). Therefore, we analyzed the three-dimensional distribution of closely and distantly connected capillaries in three animals by categorizing every capillary within an image stack by its connectivity to the occluded arteriole and by the three-dimensional position of the midpoint of each capillary. In the example of Figures 4.5C and 4.5D, the flow speed and diameter changes in 19 capillaries were measured after the target

penetrating arteriole was occluded, and in all but three cases, the topological classification (closely or distantly connected) correctly predicted the measured physiological response (either slowed and dilated or unchanged). This consistency supports the observed relationship between the topological classification and the vessel's response (Figure 4.5B, inset). In this example, many distantly connected capillaries were adjacent to closely connected vessels (Figure 4.5D). Across three animals, we find that at a distance of ~120 mm from the targeted penetrating arteriole, about 16% (95% confidence interval, 10% to 24%, 1,101 vessels) of distantly connected capillaries had a capillary that was closely connected to the target penetrating arteriole as their nearest spatial neighbor (Supplementary Text; Supplementary Figure 4.4). The average distance between a closely connected capillary and the nearest distantly connected capillary was 46±12 mm (mean±s.d.; Supplementary Figure 4.5A). For the subset of distantly connected capillaries that had a closely connected vessel as a nearest neighbor, the separation between the two vessels was only 35±15mm (Supplementary Text; Supplementary Figure 4.5B).

Figure 4.5 Large decreases in blood flow speed are linked to vasodilation. (A) Change in diameter versus change in centerline RBC speed in neighboring penetrating arterioles after penetrating arteriole occlusion and in control experiments. Yellow circle and lines show mean and s.d. Data points not shown in urethane clot: (51% diameter, 67% speed), urethane control: (428%, 68%), isoflurane control: (370%, 149%), (267%, 204%). (B) Change in diameter versus change in speed in capillaries after penetrating arteriole occlusion and in control experiments. Data were clustered by k-means into two groups (red and blue). One point not shown in control: (537%, 95%). (B, inset) Cumulative probability of capillaries downstream from an occluded penetrating arteriole being in the slowed and dilated (red) or unaffected (blue) cluster as a function of the topological separation between the capillary and the target vessel from 1 to 9 branches downstream. (C) Rendering of two-photon excited fluorescence image stack of capillaries using Voxx (Clendenon et al, 2002). (D) Capillaries from (C) categorized as closely (one to four branches) or distantly (more than four branches) connected to the occluded vessel with each dot centered approximately on the capillary. Circles around dots indicate categorization of the measured subset of vessels into the clusters from (B). In two (one) of 19 measured vessels, the topological classification suggests the vessel should slow and dilate (be unaffected) when the cluster analysis places it in the other group. Yellow line in (C, D) indicates the occluded penetrating arteriole.

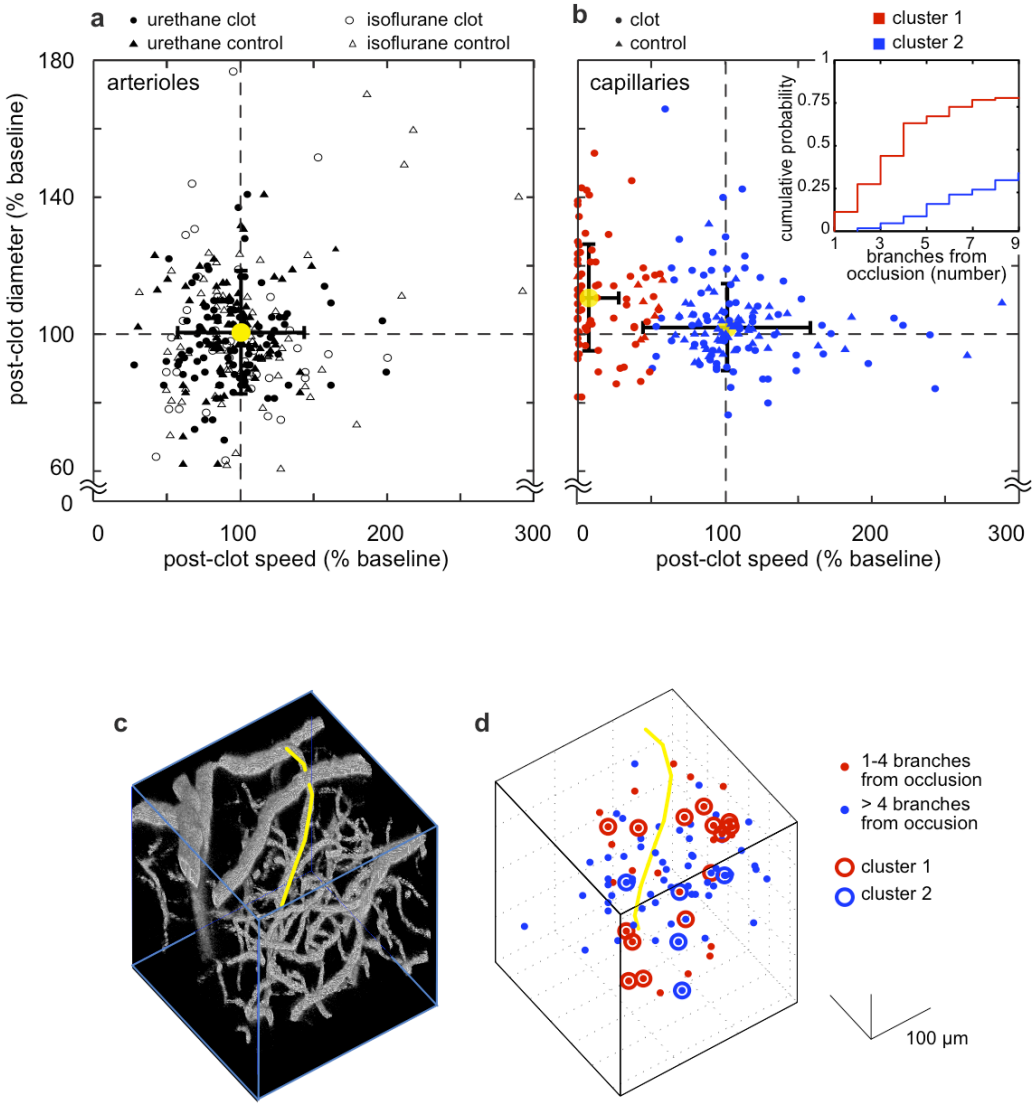
a
urethane clot
urethane control
isoflurane clot
isoflurane control
arterioles
post-clot diameter (% baseline)
post-clot speed (% baseline)
b
clot
control
cluster 1
cluster 2
capillaries
cumulative probability
branches from occlusion (number)
post-clot speed (% baseline)
c
d
1-4 branches from occlusion
> 4 branches from occusion
cluster 1
cluster 2
100 µm

Acetylcholine Application Dilated Vessels After a Penetrating Arteriole Occlusion, But Did Not Improve Flow in the Most Slowed Capillaries

After the measurements during occlusion, ACh (10mmol/L in ACSF) was perfused into the cranial window and each vessel was remeasured in a subset of animals. Penetrating arterioles neighboring the occlusion dilated with ACh relative to the postclot diameter (Figure 4.6A; Wilcoxon paired rank sign test, $P = 0.0002$). The Ach also caused the RBC flow in these vessels to increase relative to the RBC flow during the occlusion (Figure 4.6A; Wilcoxon paired rank sign test, $P < 0.0001$). Aggregated across all measurements capillaries dilated relative to clot diameters with ACh (Figure 4.6A; Wilcoxon paired rank sign test, $P = 0.00025$). Capillaries with different topological separation from the occluded penetrating arteriole dilated similarly in response to ACh application (Figure 4.6B; Cuzick's tend test, $P = 0.85$).

With ACh application after occlusion, the median RBC speeds one to two (three to four) branches downstream from the occluded penetrating arteriole remained at < 1% (13%) of baseline (Figure 4.6C). Ten or more branches away, the ACh causes an increase in median RBC speed to 105% of baseline values. Despite the dilation of both neighboring penetrating arterioles and capillaries, RBC speed in the down-stream capillaries most affected by a penetrating arteriole occlusion was not substantially improved by ACh, whereas distantly connected vessels became slightly hyperemic. Similarly, RBC flux, the number of RBCs flowing through the capillary segment per unit time, decreased severely in the capillaries closest to the occlusion, and was not improved with ACh application (Supplementary Text; Supplementary Figure 4.6).

Figure 4.6 Changes in postclot vessel diameter and flow speed after topical application of a vasodilator (10mmol/L acetylcholine (ACh)). (A) Neighboring penetrating arterioles and capillaries around an occlusion increased in diameter and in RBC flow, each expressed as a percentage of the baseline value, after topical application of ACh. Inset shows full range of data for arterioles. Arteriole clot data, shown for comparison, are same as in Figure 1, with urethane anesthesia. (B) Capillary diameter after ACh application, expressed as a percentage of the diameter after occlusion, as a function of the topological separation between the capillary and the occluded arteriole. Two outliers not shown at baseline: (branches 5 to 6, 65%), (>10, 56%). (C) Absolute value of speeds in capillaries before, after clotting of a penetrating arteriole, and after ACh application as a function of the number of branches the capillaries are downstream from the occluded vessel. Two outliers not shown at baseline: (two branches, 5.3 mm/s), (> 10, 4.2 mm/s). Square brackets indicate significant differences with Wilcoxon ranks sum test for paired data.

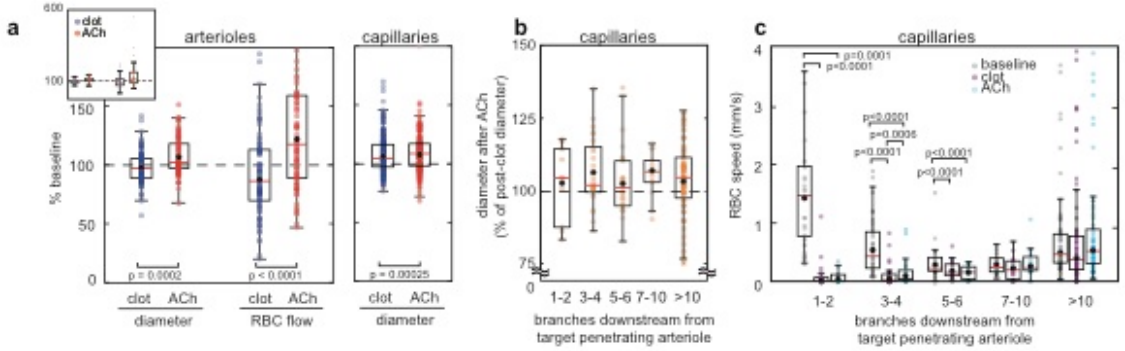
a
clot
ACh
arterioles
capillaries
% baseline
p = 0.0002
p < 0.0001
p = 0.00025
clot ACh
clot ACh
clot ACh
diameter
RBC flow
diameter
b
capillaries
diameter after ACh
(% of post-clot diameter)
1-2 3-4 5-6 7-10 >10
branches downstream from
target penetrating arteriole
c
capillaries
RBC speed (mm/s)
baseline
clot
ACh
p<0.0001
p<0.0001
p<0.0001
p<0.0001
p<0.0001
p<0.0001
1-2 3-4 5-6 7-10 >10
branches downstream from
target penetrating arteriole

DISCUSSION

Targeted Femtosecond Laser Ablation Provides a Viable Technique for Forming Clots in Individual Penetrating Arterioles

Femtosecond laser ablation can trigger clotting in penetrating arterioles while preserving structure and flow in neighboring vessels, enabling the study of physiological processes, such as vasoreactivity, in the nearby microvessels. This laser ablation technique is a variation on the method previously developed to clot single cortical capillaries (Nishimura et al, 2006). As the interaction of the laser light and the tissue depends on nonlinear absorption, only the targeted portion of the vessel is injured by the laser and the subsequent clotting and occlusion are limited to a single vascular segment. Previous work on occlusions of penetrating arterioles used photo-chemical thrombosis with rose bengal (Nishimura et al, 2007). As the rose bengal method uses linear optical excitation to produce the singlet oxygen that damages the vessel wall and initiates clotting, it is not possible to confine the effect to a single vessel segment and some level of clotting in surrounding capillaries is very difficult to avoid. To rule out the possible effects of our clotting technique on vasoreactivity, we tested both the femtosecond laser ablation and photochemical methods for clotting penetrating arterioles and saw no dilation in neigh- boring penetrating arterioles for both methods (Supplementary Figure 4.2). In addition, previous measurements of flow changes in capillaries after a penetrating arteriole occlusion produced using the rose bengal method (Nishimura et al, 2007) are similar to those reported here (Figures 4.4A and 4.4C).

Neighboring Penetrating Arterioles Do Not Dilate to Compensate for Penetrating Arteriole Occlusion

We used 2PEF microscopy to investigate whether active vascular regulation in surrounding penetrating arterioles mitigates the decreased flow in capillaries downstream from an occluded cortical penetrating arteriole. We first investigated whether the neighboring penetrating arterioles that feed territories adjacent to the occluded vessel dilate in response to the occlusion (Figure 4.1). Contrary to the expectation that the occlusion could trigger a compensatory vasoactive response in the surrounding area, the neighboring penetrating arterioles did not dilate (Figure 4.1F). Even the closest arterioles, both in topological and spatial distance, did not dilate after occlusion (Figure 4.2). Our methods had sufficient statistical power (Supplementary Text) to resolve changes in arteriole diameter and RBC speed of a magnitude comparable to or smaller than those observed in neurovascular coupling. Taken together, this data suggest that it is unlikely there is any physiologically relevant compensatory vasoregulatory mechanism that is recruited to increase flow in neighboring penetrating arterioles to increase perfusion in the tissue adjacent to the occluded arteriole.

This absence of dilation is in marked contrast to the coordinated dilation of local and upstream arterioles that occurs in response to increases in neural activity (Devor et al, 2008; Iadecola et al, 1997). Upstream dilation of arterioles in neurovascular coupling (and other systems such as muscle) is likely to be mediated by signal conduction in the endothelium (Dietrich et al, 1996; Welsh and Segal, 1998) or astrocytes (Xu et al, 2008). Our observation of dilation in the neighboring penetrating

arterioles after ACh application (Figure 4.6A), an endothelium- dependent dilator (Faraci and Heistad, 1998; Rosenblum and Nelson, 1988), indicates that both endothelium and smooth muscle were functional despite experimental manipulations. This suggests that the lack of dilation after penetrating arteriole occlusion comes from a lack of signaling. Although we used two different mechanisms for clotting that show similar results, we cannot eliminate the possibility that the lack of dilation of neighboring arterioles after the clot is an artifact of our technique. Injured endothelial cells or astrocytes at the clot location might not be capable of conducting the vasodilatory signals that might otherwise be present (Emerson and Segal, 2000; Xu et al, 2008). However, because these cells are quite susceptible to ischemia or hypoxia (Fisher, 2008), it is likely that a naturally forming thrombus or an embolus would also result in a disruption of endothelial or astrocyte function that would interfere with any possible vasodilatory signal (Emerson and Segal, 2000).

Vessel Dilation Is Correlated with Large Flow Speed Decreases

Although no dilation was observed in arterioles, a subset of capillaries do dilate after the occlusion (Figures 4.4B and 4.4D). Cluster analysis of downstream capillaries suggests that there is a trend for lower flow to be associated with a larger dilation (Figure 4.5B). No such trend is observed in the neighboring penetrating arterioles (Figure 4.5A), but this may be explained by the fact that after a single penetrating arteriole occlusion, flow in other arterioles does not drop to the extremely low levels observed in the downstream capillaries. After larger strokes, such as MCA occlusions, other investigators do observe acute vasodilation in the surface and penetrating

arterioles that sit downstream from the occlusion (Belayev et al, 2002; Shih et al, 2009; Tomita et al, 2005; Wei et al, 1998), consistent with the idea that drastically reduced flow or intraluminal pressure is necessary to trigger dilation. In the work by Shih et al (2009), mean velocities in penetrating arterioles dropped to ~30% of baseline and vessel diameter increased to ~120% of baseline after MCA occlusion. Wei et al (1998) made ministrokes by ligating several surface arterioles and noted a marked dilation and also described considerable slowing in nearby surface arterioles. Taken together, these data suggest that the vasodilation signal does not activate in a vessel until hemodynamics have substantially changed in that vessel.

Spatial Heterogeneity in Capillary Dilation Suggests that the Vasodilatory Signal Is Not of Parenchymal Origin

The spatial distribution of dilated and undilated capillaries rules out a parenchymal source for the vasodilation signal. There are frequent occurrences in which an extremely slowed and dilated capillary is adjacent to a rapidly flowing and undilated capillary. This is reflected in the aggregate data as a strong dependence of the speed and diameter changes on the topological separation (Figures 4.4A and 4.4B), but not the spatial distance (Figures 4.4C and 4.4D) between a capillary and the occluded penetrating arteriole. Analysis of the spatial distribution of vessels with different topological separation (Supplementary Figures 4.4 and 4.5) shows that capillaries only a few branches downstream from the target, which slow and dilate after the occlusion, are spatially interspersed with more distantly connected capillaries, which are largely unaffected by the clot (Figures 4.5C and 4.5D). The close proximity of dilated and

unaffected capillaries suggests that there is no signal for vasodilation that originates from the neurons or astrocytes or other parenchymal cells. If such a diffusible signal from the parenchymal tissue existed, one would expect that capillaries spatially near but many branches away from the occluded arteriole would dilate along with nearby, but more closely connected vessels.

Past work using a pimonadozole probe that precipitates in severe hypoxia suggests that tissue within 150 mm of a penetrating arteriole occlusion is relatively uniformly hypoxic (Nishimura et al, 2007). Our observations of undilated vessels in this region suggest vessels that maintain high levels of flow do not dilate even if they run through regions of likely hypoxia near the occluded vessel. This argues that tissue hypoxia is not sufficient to drive vasodilation. Current ideas that neurovascular coupling in the normal brain is linked to synaptic release and byproducts of neuronal activity rather than to metabolism or oxygen usage are consistent with our findings (Attwell and Iadecola, 2002; Devor et al, 2008; Lindauer et al, 2009; Sukhotinsky et al, 2010). For example, recent work on neurovascular coupling shows blood flow still increases in regions of neuronal activity even under hyperbaric hyper- oxygenation, which demonstrates another case in which dexoygenation is decoupled from vasodilation (Lindauer et al, 2009). We find that the alterations in oxygenation and energy delivery caused by blood flow decreases due to a penetrating arteriole occlusion do not generate upstream or diffusible vasodilatory signals, even though the oxygenation and metabolite deficits due to occlusions are more severe than those caused by normal neuronal activity.

Dilation in Capillaries Downstream from a Penetrating Arteriole Occlusion Is Triggered by a Vasogenic Signal, Likely Changes in Transmural Pressure

The dilation in downstream capillaries after penetrating arteriole occlusion (Figure 4.4B) suggests that there is a perfusion-dependent signal for dilation. Possible candidates for the vasodilatory signal include flow-dependent forces such as changes in shear stress or transmural pressure. Arterioles do respond to changes in shear stress, but arterioles tend to dilate in response to an increase in shear stress (Ngai and Winn, 1995). This response is the opposite of what is observed in the capillaries in our experiments and in surface and penetrating arterioles after MCA occlusion (Belayev et al, 2002; Shih et al, 2009; Tomita et al, 2005; Wei et al, 1998) in which vessels dilate in response to decreased flow. Hematocrit in the capillaries did not change significantly after occlusion (Supplementary Text; Supplementary Figure 4.3), but the RBC flux did drop in proportion to the speed change, suggesting that dilated capillaries may respond to some change in the rate of RBCs that pass through (Supplementary Text; Supplementary Figure 4.6). A more likely candidate is change in transmural pressure. Brain arterioles constrict with increased pressure, suggesting that decreased transmural pressure could trigger dilation (Ngai and Winn, 1995; Schmid-Schonbein, 1999). The vessels immediately downstream from a penetrating arteriole are likely at reduced luminal pressure after the occlusion relative to before the occlusion because these vessels are now effectively farther downstream from a high-pressure arteriole. Similarly, surface and penetrating arterioles would be at reduced luminal pressure after MCA occlusion, suggesting that a myogenic mechanism for vasodilation could be also responsible for the acute dilation observed after large stroke

models (Belayev et al, 2002; Shih et al, 2009; Tomita et al, 2005; Wei et al, 1998). Thus, our work suggests that acute postclot vascular reactivity could use the same mechanisms involved in autoregulation, which keeps brain perfusion constant under changing systemic blood pressure.

Hemodynamic Arguments Against Vasodilators as Therapies for Microvascular Strokes

We applied a vasodilator, ACh, to investigate whether increasing flow in unoccluded arterioles can substantially improve flow in capillaries down- stream from an occluded penetrating arteriole (Figure 4.6). Despite dilation in both neighboring penetrating arterioles and capillaries, ACh did not substantially improve perfusion in the territory of decreased flow caused by the occlusion. The ACh leads to only a very small increase in the magnitude of RBC speed (Figure 4.6C). The first few branches downstream from the occlusion are most severely affected by the clot and are also the least improved by vasodilator application. This result suggests that although connections between penetrating arteriole territories through the capillary bed exist (Moody et al, 1990), they are too infrequent to provide flow between territories. Clinical trials for vasodilators such as xanthine derivatives for treatment of vascular dementia (Kittner et al, 1997; Pantoni, 2004) have not shown significant efficacy and have also been disappointing for the treatment of stroke (Bath and Bath-Hextall, 2004; Bereczki and Fekete, 2008). If vascular dementia is driven by the effects of many small vessel occlusions, our finding that ACh does not improve flow downstream from the occlusion might be a contributing factor to the drug trials' somewhat

disappointing results. However, we can- not rule out that other patterns of dilation driven by mechanisms other than ACh might be more effectual or that vasodilators might have significant impact in the case of partial occlusions. Alternative strategies for increasing flow include reducing blood viscosity (Nishimura et al, 2006) or leukocyte adhesion (Belayev et al, 2002), each of which have been found to increase flow downstream from local occlusions. However, it is not clear that these flow increases are sufficient to be therapeutic.

REFERENCES

1. Attwell D, Iadecola C (2002) The neural basis of functional brain imaging signals. Trends Neurosci 25:621–5

2. Bath PM, Bath-Hextall FJ (2004) Pentoxifylline, propentofylline and pentifylline for acute ischaemic stroke. Cochrane Database Syst Rev; CD000162

3. Belayev L, Pinard E, Nallet H, Seylaz J, Liu Y, Riyamongkol P, Zhao W, Busto R, Ginsberg MD (2002) Albumin therapy of transient focal cerebral ischemia: in vivo analysis of dynamic microvascular responses. Stroke 33:1077–84

4. Bereczki D, Fekete I (2008) Vinpocetine for acute ischaemic stroke. Cochrane Database Syst Rev; CD000480

5. Blinder P, Shih AY, Rafie C, Kleinfeld D (2010) Topological basis for the robust distribution of blood to rodent neocortex. Proc Natl Acad Sci USA 107:12670–5

6. Clendenon JL, Phillips CL, Sandoval RM, Fang S, Dunn KW (2002) Voxx: a PC-based, near real-time volume rendering system for biological microscopy. Am J Physiol Cell Physiol 282:C213–8

7. Coyle P, Heistad DD (1987) Blood flow through cerebral collateral vessels one month after middle cerebral artery occlusion. Stroke 18:407–11

8. Cuzick J (1985) A Wilcoxon-type test for trend. Stat Med 4:87–90

9. Devor A, Hillman EM, Tian P, Waeber C, Teng IC, Ruvinskaya L, Shalinsky MH, Zhu H, Haslinger RH, Narayanan SN, Ulbert I, Dunn AK, Lo EH, Rosen BR, Dale AM, Kleinfeld D, Boas DA (2008) Stimulus- induced changes in blood flow and 2-deoxyglucose uptake dissociate in ipsilateral somatosensory cortex. J Neurosci 28:14347–57

10. Dietrich HH, Kajita Y, Dacey RG Jr (1996) Local and conducted vasomotor responses in isolated rat cerebral arterioles. Am J Physiol 271:H1109–16

11. Emerson GG, Segal SS (2000) Endothelial cell pathway for conduction of hyperpolarization and vasodilation along hamster feed artery. Circ Res 86:94–100

12. Faraci FM, Heistad DD (1998) Regulation of the cerebral circulation: role of endothelium and potassium channels. Physiol Rev 78:53–97

13. Faul F, Erdfelder E, Lang AG, Buchner A (2007) G*Power 3: a flexible statistical power analysis program for the social, behavioral, and biomedical sciences. Behav

Res Methods 39:175–91

14. Fisher M (2008) Injuries to the vascular endothelium: vascular wall and endothelial dysfunction. Rev Neurol Dis 5(Suppl 1):S4–11

15. Iadecola C, Yang G, Ebner TJ, Chen G (1997) Local and propagated vascular responses evoked by focal synaptic activity in cerebellar cortex. J Neurophysiol 78:651–9

16. Kittner B, Rossner M, Rother M (1997) Clinical trials in dementia with propentofylline. Ann NY Acad Sci 826:307–16

17. Kleinfeld D, Delaney KR (1996) Distributed representation of vibrissa movement in the upper layers of somatosensory cortex revealed with voltage sensitive dyes. J Comp Neurol 375:89–108

18. Kleinfeld D, Mitra PP, Helmchen F, Denk W (1998) Fluctuations and stimulus-induced changes in blood flow observed in individual capillaries in layers 2 through 4 of rat neocortex. Proc Natl Acad Sci USA 95:15741–6

19. Kovari E, Gold G, Herrmann FR, Canuto A, Hof PR, Michel JP, Bouras C, Giannakopoulos P (2004) Cortical micro- infarcts and demyelination significantly affect cognition in brain aging. Stroke 35:410–4

20. Lindauer U, Leithner C, Kaasch H, Rohrer B, Foddis M, Fuchtemeier M, Offenhauser N, Steinbrink J, Royl G, Kohl-Bareis M, Dirnagl U (2009) Neurovascular coupling in rat brain operates independent of hemoglobin deoxygenation. J Cereb Blood Flow Metab 30:757–68

21. Moody DM, Bell MA, Challa VR (1990) Features of the cerebral vascular pattern that predict vulnerability to perfusion or oxygenation deficiency: an anatomic study. AJNR Am J Neuroradiol 11:431–9

22. Muller M, Squier J, Wolleschensky R, Simon U, Brakenhoff GJ (1998) Dispersion pre-compensation of 15 femtosecond optical pulses for high-numerical-aperture objectives. J Microsc 191:1141–50

23. Ngai AC, Winn HR (1995) Modulation of cerebral arteriolar diameter by intraluminal flow and pressure. Circ Res 77:832–40

24. Nguyen QT, Tsai PS, Kleinfeld D (2006) MPScope: a versatile software suite for multiphoton microscopy. J Neurosci Methods 156:351–9

25. Nishimura N, Schaffer CB, Friedman B, Lyden PD, Kleinfeld D (2007) Penetrating arterioles are a bottleneck in the perfusion of neocortex. Proc Natl Acad

Sci USA 104:365–70

26. Nishimura N, Schaffer CB, Friedman B, Tsai PS, Lyden PD, Kleinfeld D (2006) Targeted insult to subsurface cortical blood vessels using ultrashort laser pulses: three models of stroke. Nat Methods 3:99–108

27. Ogawa S, Lee T-m, Nayak AS, Glynn P (1990) Oxygenation- sensitive contrast in magnetic resonance image of rodent brain at high fields. Magn Reson Med 14:68–78

28. Pantoni L (2004) Treatment of vascular dementia: evidence from trials with non-cholinergic drugs. J Neurol Sci 226:67–70

29. Park L, Zhou P, Pitstick R, Capone C, Anrather J, Norris EH, Younkin L, Younkin S, Carlson G, McEwen BS, Iadecola C (2008) Nox2-derived radicals contribute to neurovascular and behavioral dysfunction in mice overexpressing the amyloid precursor protein. Proc Natl Acad Sci USA 105: 1347–52

30. Rosenblum WI, Nelson GH (1988) Endothelium-dependent constriction demonstrated in vivo in mouse cerebral arterioles. Circ Res 63:837–43

31. Schaffer CB, Friedman B, Nishimura N, Schroeder LF, Tsai PS, Ebner FF, Lyden PD, Kleinfeld D (2006) Two-photon imaging of cortical surface microvessels reveals a robust redistribution in blood flow after vascular occlusion. PLoS Biol 4:e22

32. Schmid-Schonbein GW (1999) Biomechanics of microcircu- latory blood perfusion. Annu Rev Biomed Eng 1:73–102

33. Shih AY, Friedman B, Drew PJ, Tsai PS, Lyden PD, Kleinfeld D (2009) Active dilation of penetrating arteri- oles restores red blood cell flux to penumbral neocortex after focal stroke. J Cereb Blood Flow Metab 29:738–51

34. Sigler A, Goroshkov A, Murphy TH (2008) Hardware and methodology for targeting single brain arterioles for photothrombotic stroke on an upright microscope. J Neurosci Methods 170:35–44

35. Sukhotinsky I, Yaseen MA, Sakadzic S, Ruvinskaya S, SimsJR, Boas DA, Moskowitz MA, Ayata C (2010) Perfusion pressure-dependent recovery of cortical spreading depression is independent of tissue oxygenation over a wide physiologic range. J Cereb Blood Flow Metab 30:1168–77

36. Tomita Y, Kubis N, Calando Y, Tran Dinh A, Meric P, Seylaz J, Pinard E (2005) Long-term in vivo investigation of mouse cerebral microcirculation by fluorescence con- focal microscopy in the area of focal ischemia. J Cereb Blood Flow Metab 25:858–67

37. Vander Eecken HM, Adams RD (1953) The anatomy and functional significance of the meningeal arterial anastomoses of the human brain. J Neuropathol Exp Neurol 12:132–57

38. Vermeer SE, Prins ND, den Heijer T, Hofman A, Koudstaal PJ, Breteler MM (2003) Silent brain infarcts and the risk of dementia and cognitive decline. N Engl J Med 348:1215–22

39. Watson BD, Dietrich WD, Busto R, Wachtel MS, Ginsberg MD (1985) Induction of reproducible brain infarction by photochemically initiated thrombosis. Ann Neurol 17:497–504

40. Wei L, Craven K, Erinjeri J, Liang GE, Bereczki D, Rovainen CM, Woolsey TA, Fenstermacher JD (1998) Local cerebral blood flow during the first hour following acute ligation of multiple arterioles in rat whisker barrel cortex. Neurobiol Dis 5:142–50

41. Welsh DG, Segal SS (1998) Endothelial and smooth muscle cell conduction in arterioles controlling blood flow. Am J Physiol 274:H178–86

42. Xu HL, Mao L, Ye S, Paisansathan C, Vetri F, Pelligrino DA (2008) Astrocytes are a key conduit for upstream signaling of vasodilation during cerebral cortical neuronal activation in vivo. Am J Physiol Heart Circ Physiol 294:H622–32

SUPPLEMENTARY METHODS

Vascular identification

Penetrating arterioles were identified as vessels plunging into the brain in which the flow was directed into the brain parenchyma, as confirmed by using linescans in the surface segment of the penetrating vessel. Penetrating arterioles give rise directly to a capillary network. Communicating arterioles are defined as the surface arterioles that give rise to other arterioles and do not penetrate into the cortex. Subsurface vessels include penetrating arterioles, capillaries and ascending venules. The measured and targeted penetrating arterioles come from the same population, with similar diameters (11.7 μm mean diameter for targets and 11.9 μm for neighboring) and speeds (4.9 mm/s mean speed for target vessels and 4.7 mm/s for neighboring) (Supplementary Fig. 4.1). For convenience, we defined all the branches of penetrating arterioles of a size less than 10 μm as "capillaries". Capillaries coalesced into ascending venules, defined as vessels that run vertically up to the cortical surface and in which flow is directed out of the cortex (Fig. 4.3a).

To quantify the topological relationship between the penetrating arteriole targeted for clotting and neighboring penetrating arterioles we counted the number of branches between the target and neighboring penetrating arterioles, as traced through the surface arteriole network. We also categorized capillaries by the number of branches they lie downstream from the penetrating arteriole that was targeted for occlusion. Capillaries with no connection to the target penetrating arteriole that could be traced in our image volume and capillaries more than 10 branches away from the target vessel were grouped together ("> 10 branches"). This latter group includes

capillary branches from penetrating arterioles neighboring the occluded vessel. This quantification scheme was selected rather than conventions based on branching order or diameters [1-3] because penetrating arterioles seem to serve a unique anatomical and topological position linking the two-dimensional surface arteriole network to the three-dimensional capillary bed. In addition, our previous studies have shown regardless of the type of vessel occluded (surface arteriole [4], capillary [5] or penetrating arteriole [6]) the number of branches a vessel sits away from the occlusion is a strong determinant of the amount of RBC speed change. The disadvantage of this scheme is that it does not facilitate comparison to other organs because it starts the count at anatomical features that are unique to the brain.

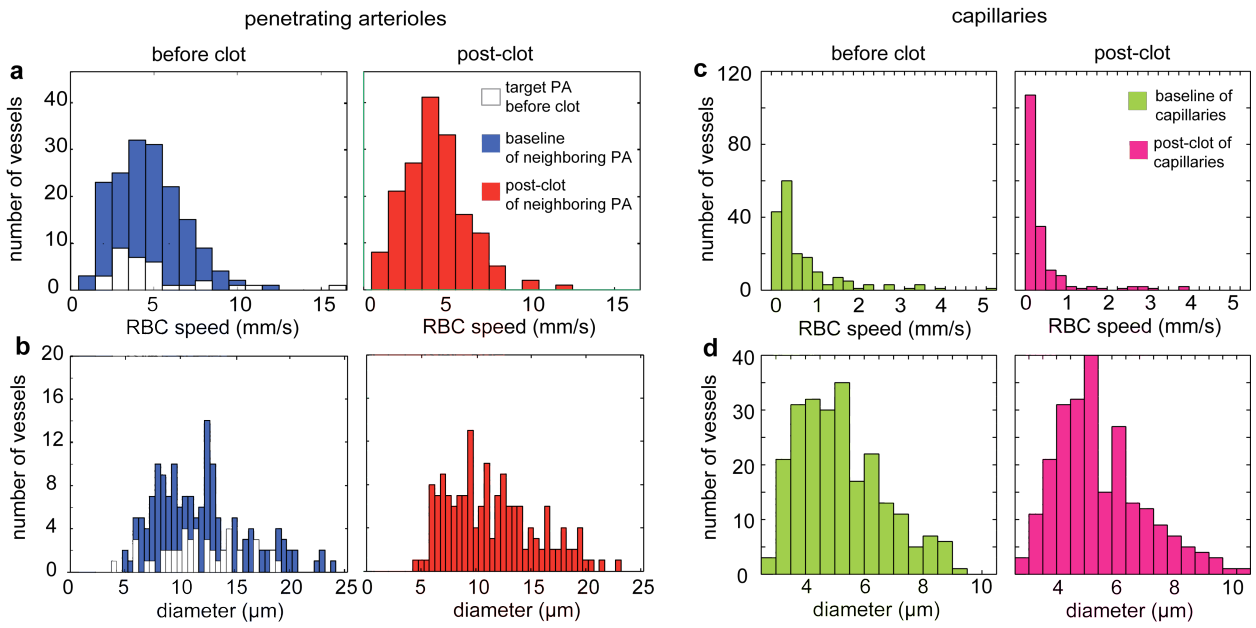

Supplementary Fig. 4.1 Histograms showing distributions of centerline red blood cell speeds (a) and vessel diameter (b) of targeted and measured penetrating arterioles (PA) before and after occlusion of the target vessel. These histograms include both urethane and isoflurane anesthesia and femtosecond and rose bengal occlusion methods. Histograms of capillary red blood cell speeds (c) and vessel diameters (d) before and after occlusion of a nearby penetrating arteriole.

Photothrombotic occlusion of penetrating arterioles

As an alternative to clotting with femtosecond laser ablation we used photochemical thrombosis. In this method, 1% (wt/vol) rose bengal in physiological saline was intravenously injected (100 mg/kg rat weight). While imaging with 2PEF microscopy, 1 mW of 532-nm wavelength laser light (Compass 215M; Coherent, Inc.) was focused on the lumen of the target vessel to photoactivate the rose bengal. The photoactivated rose bengal generates singlet oxygen, which locally damages the endothelium of the vessel and initiates clotting of the vessel [7,8].

Plot generation

Box plots were generated with Matlab (Mathworks, Inc.) using the boxplot function which displays the 25th percentile value of the data set (first quartile), median, 75th percentile value of the data set (third quartile), and whiskers denoting the minimum and maximum values that are not outliers. Data points were considered outliers if points fell below the 1.5 times the interquartile range from the first quartile or above 1.5 times the interquartile range from the third quartile. The interquartile is defined as the third quartile minus the first quartile. Means were calculated excluding statistical outliers indicated by the box plot algorithm and are indicated as bold dots in the plots.

Trends with spatial distance away from target diving arteriole were analyzed using Matlab. A running median and 95% confidence interval with a 200-μm window was applied for arterioles (Fig. 4.2d-f), 50-μm window for capillaries (Fig. 4.4c-d). The median trend line and confidence interval were then smoothed using a 50-μm wide moving average. Trend line points that were calculated with less than six data points were omitted from the graph. Matlab was used for k-means clustering analysis (Fig. 4.5b).

RBC flow determination in arterioles

Total flow in a vessel is the sum of plasma and RBC flow. Our measurements provide a direct assay of RBC speed, so we focus on a relationship for change in flow of RBCs, and do not consider plasma flow or changes in plasma flow. The RBC flow (volume of RBCs/time) in a vessel is related to radius, R, hematocrit, $h(r)$, and velocity, $v(r)$, which both vary with distance from the center of the vessel, r.

$$Flow_{RBC} = \int_0^R h(r)v(r)2\pi r dr \qquad \text{(Supplementary Eqn. 1)}$$

The RBC velocity profile across a small arteriole is not quite parabolic and varies over time with heartbeat. Previous measurements in rat brain arterioles of the shape of this profile averaged over time, however, suggest that approximating the RBC velocity profile as a function of *r*/*R* seems to be reasonable [4] because it is smooth and close to parabolic. The hematocrit profile across an arteriole *in vivo* is not well understood although measurements suggest that a cell free layer exists near the vessel wall, with RBCs packed closer to the vessel center. The hematocrit in this central region is a smooth function of radial position and is almost flat or slightly peaked in the center of the vessel [9]. These data suggest that both *v(r)* and *h(r)* are well-behaved functions that likely scale as *r*/*R*, so that the RBC flow is proportional to the area and *v*, the centerline speed of the vessel $Flow_{RBC} \propto R^2 v$. The proportionality constant depends on the flow profile and spatial variations in hematocrit.

In this work we present the ratios of RBC flow after a clot (or control) to the baseline value,

$$\frac{Flow_{RBC,post}}{Flow_{RBC,pre}} = \frac{R_{post}^{\ 2} v_{post}}{R_{pre}^{\ 2} v_{pre}} \qquad \text{(Supplementary Eqn. 2)}$$

so that we do not need to explicitly know the proportionality constant. We assume that any changes in diameter or speed in the vessel are small enough that the proportionality constant does not change. In the regime of the observed changes in

diameters (~10%) and RBC speeds (~10%) in the arterioles measured in our work, neither the hematocrit distribution nor the shape of the RBC velocity profile in the same arteriole are likely to change enough to significantly alter the dependence RBC flow on area and centerline speed. Experimental data summarized by Furman and Olbricht [10] suggest that the ratio between the average velocity of the RBCs and the flow of the combined plasma and RBCs is not strongly dependent on diameter in the range of the arteriole diameters studied here. This suggests that hematocrit distribution does not change dramatically in our experimental regime in arterioles and can be ignored in estimates the ratio of RBC flow, justifying the use of the relationship shown in Supplementary Eqn. 2.

The linescan velocity measurement technique was calibrated by translating fluorescently labeled, stationary samples on an encoded motorized stage. We estimate an uncertainty of 1% in the velocity measurement averaged over 40 s for vessels at 10 mm/s, at the upper range of speeds studied in this work. Because the position of edges of objects far apart (large separations compared to the diffraction-limited optical resolution) can be resolved to better than optical resolution of the microscope objective, we can resolve 0.25 μm changes in diameter, so for a 10-μm diameter vessel, 2.5% of diameter. Assuming that changes in flow scale as area x speed this results in ~10% uncertainty in RBC flow. This is approximately the measured uncertainty found in repeated measurements of the same vessel [4] and is smaller than the flow changes reported in neurovascular coupling.

RBC flux and hematocrit measurement in capillaries

RBC flux (number of RBCs/time) was extracted from linescan data by explicitly counting the number of RBCs that pass through the vessel. This method works only in capillaries, where RBCs travel single file. For each time segment (43 ms) in the approximately 40-s long linescan data the angle of the streaks formed by moving RBCs was calculated and the image was rotated so that the lines are horizontal. The fluorescence intensity was then averaged along the horizontal direction. The edges between RBCs and the blood plasma were detected by thresholding at 15% of the maximum average intensity, and the number of RBCs was calculated as half the number of detected edges. This algorithm was verified with a comparison to a manual count of streaks formed by moving RBCs in the linescan images over approximately 2 seconds for 94 individual capillaries. We found that up to an RBC flux of approximately 50 RBC/s flux, the hand count and automated count agreed very well. At higher flux rates of 50-100 RBC/s, the automated count undercounted by about 30% so that our estimates of flux at baseline in faster flowing capillaries may be somewhat low.

To calculate the tube hematocrit in individual capillaries, we use the RBC flux determined above, together with the RBC speed and vessel size. To ensure accurate hematocrit measurements, we only evaluated vessels that at baseline had flux below 50 RBCs/s, where we found our RBC flux determination algorithm to be most accurate. This does mean that our data tends to exclude some of the faster vessels with higher flux. We use the average vessel radius across the segment in which the velocity and flux was measured. Following Constantinescu, *et al*, the capillary tube hematocrit, H_t, was calculated from the RBC flux, f, the RBC speed, v, the vessel radius, r, and

volume of a red blood cell, V_{RBC} [11]. We used 55 μm^3 as the V_{RBC} for rat [12].

$$H_t = \frac{fV_{RBC}}{v\pi r^2} \qquad \text{(Supplementary Eqn. 3)}$$

SUPPLEMENTARY RESULTS

Lack of vasodilation in neighboring penetrating arterioles is independent of clotting method

We had some concern that the femtosecond laser ablation occlusion method might affect vasoactivity because this method causes some bleeding from the target vessel that could release vasoconstrictive factors. We used an alternate method based on clot initiation from endothelial damage resulting from singlet oxygen production by irradiation of intravenously injected rose bengal (Nishimura et al. 2007; Schaffer et al. 2006; Sigler et al. 2008; Watson et al. 1985). This method does not produce significant extravasation. We found no significant difference in diameter changes between the two clotting methods (Supplementary Fig. 4.2a, 2-way ANOVA of ranks, $p = 0.4$). The RBC speed change showed a tendency for rose bengal method to have faster RBC speeds (Supplementary Fig. 4.2b, 2-way ANOVA of ranks $p = 0.02$, with $p = 0.0003$ for effect from clot method). However this slight difference in speed did not translate to a major effect on RBC flow, where no significant differences were found (Supplementary. Fig. 4.2c, 2-way ANOVA on ranks, $p = 0.1619$).

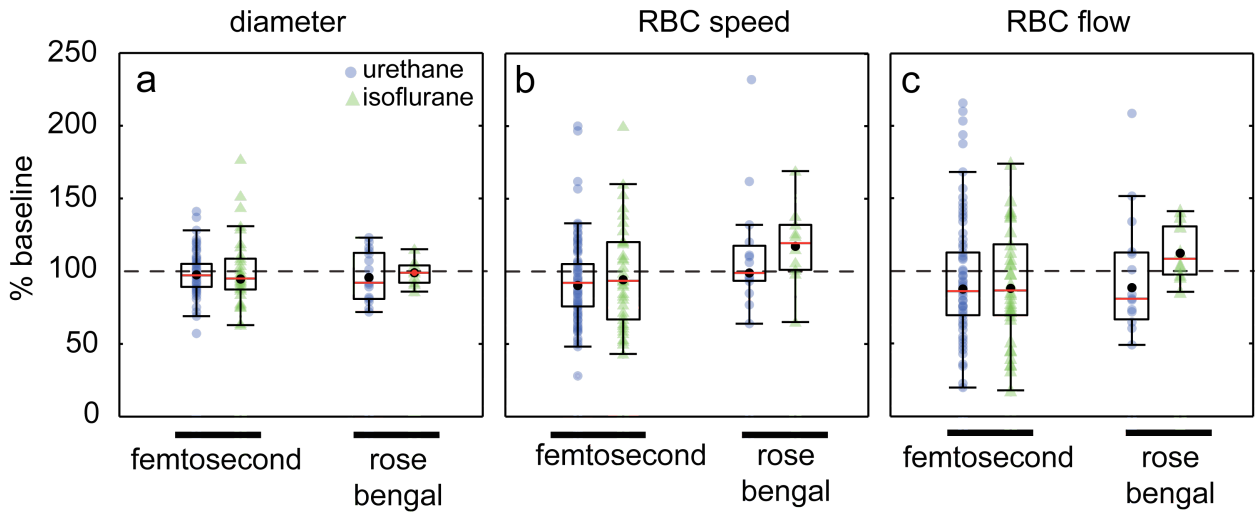

Supplementary Fig. 4.2 Occlusion technique dependence of diameter and blood flow changes in arterioles neighboring an occluded penetrating arteriole. Comparison of femtosecond laser ablation and rose bengal photochemical occlusion methods on diameter (a), centerline RBC speed (b), and RBC flow (c) after occlusion in penetrating arterioles, each expressed as percentage of baseline. Outliers not shown in (c) are 296% and 353% for the amplified technique, isoflurane anesthesia RBC flow measurements.

Hematocrit was unaffected in capillaries downstream from an occluded penetrating arteriole

Occluding a penetrating arteriole did not cause the capillary hematocrit to change relative to controls in either closely connected (four or fewer branches from occluded arteriole) or distantly connected vessels (Supplementary Fig. 4.3). Our measurements of capillary hematocrit in all capillaries was 39% +/- 16% (mean +/- std. dev.), which is higher than that found by other investigators who looked in cremaster preparations (~15%) [11, 13]. Also, in brain both the RBC flux (55 +/- 40 RBC/s) and RBC velocities (0.78 +/- 0.46mm/s) tended to be much higher than that reported for cremaster (RBC flux ~10 RBC/s and capillary velocities ~0.1-0.2 mm/s) [11, 13], suggesting organ-

dependent differences in blood flow parameters account for the difference in hematocrit [14].

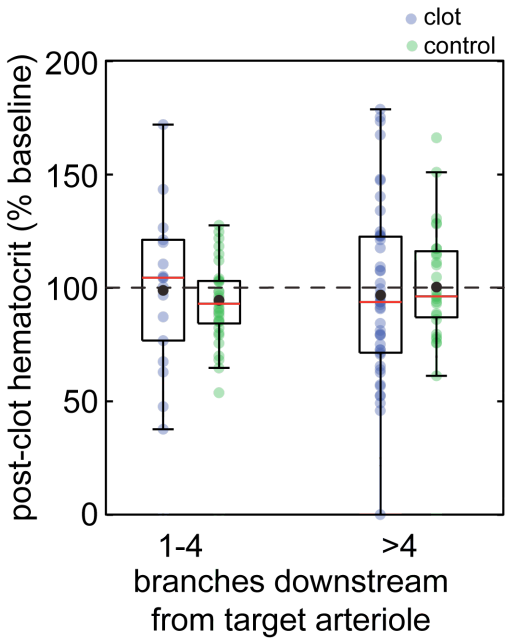

Supplementary Fig. 4.3 Capillary tube hematocrit did not change after penetrating occlusion. Post-clot capillary hematocrit, expressed as a percentage of baseline in capillaries after penetrating arteriole occlusion or time delay only (controls). Capillaries were grouped as closely connected (less than four branches downstream) or distantly connected (more than four branches downstream) to the target arteriole. No significant differences were detected with the Wilcoxon Mann Whitney rank sum test. One outlier is not shown (clot, 1-4 branches, 270%).

Relationship between topological and spatial distribution of capillaries

Capillaries were categorized as closely connected to a penetrating arteriole when there were four or fewer vascular branch points between the capillary and the penetrating arteriole. The remaining capillaries, which are five or more branches away from the arteriole, were categorized as distantly connected vessels. The division between

closely and distantly connected vessels was based on clustering analysis of the physiological response of capillaries to an occlusion (Fig. 4.5b). In three animals, all visible capillaries (1101 vessels) within an imaging volume were categorized by the number of branches separating them from a targeted penetrating arteriole. The location of each capillary was reported as the position of the midpoint. About one third of the capillaries within 50 μm of the targeted arteriole are four or fewer branches downstream from the arteriole (closely connected). This fraction decreases over about 300 μm (Supplementary Fig. 4.4a). This decrease in the fraction of vessels that are closely-connected to a penetrating arteriole, and therefore slow after the arteriole is occluded, explains the increase in the average capillary speed with radial distance from the occluded vessel (black line in Fig. 4.4c and see Nishimura, *et al* [6].

Near a penetrating arteriole, a substantial fraction of the distantly connected capillaries have as their nearest neighbor a capillary that is closely connected (Supplementary Fig. 4.4b). The representation of the capillary network by the centerpoints of the vessels is only a first approximation and serves as an initial measure of the spatial relationship between capillaries. Many capillaries wind great distances and will neighbor many vessels, so the nearest neighbor metric we use here tends to underestimate the degree of interactions between capillary territories. The closely connected capillaries are on average 46 +/-12 μm (mean +/- std) away from a distantly connected capillary (Supplementary Fig. 4.5a). A subset of distantly connected capillaries had a capillary that was closely connected to the target arteriole as the nearest neighbor. The average distance between these capillaries is 35 +/- 15 μm (Supplementary Fig. 4.5b).

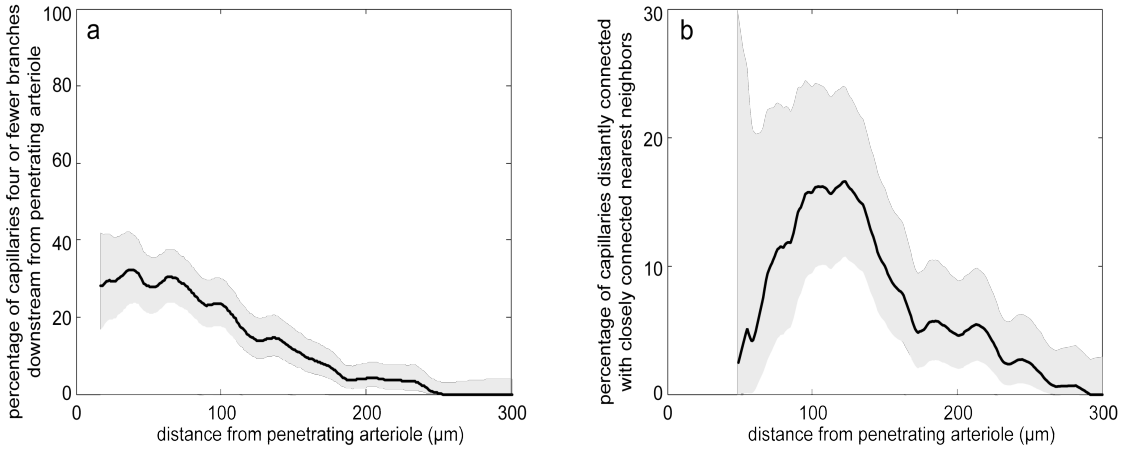

Supplementary Fig. 4.4 (a) Average fraction of vessels in a 50-μm moving window that are closely connected to a penetrating arteriole (less than four branches downstream) as a function of radial distance from the penetrating arteriole. (b) Average percentage of capillaries in a 50-μm moving window distantly connected to a penetrating arteriole (five or more branches) that have as their nearest neighbor a capillary that is closely connected to the penetrating arteriole (four or fewer branches). Gray shading indicates 95% confidence interval (binomial statistics). All traces were smoothed over 10 μm.

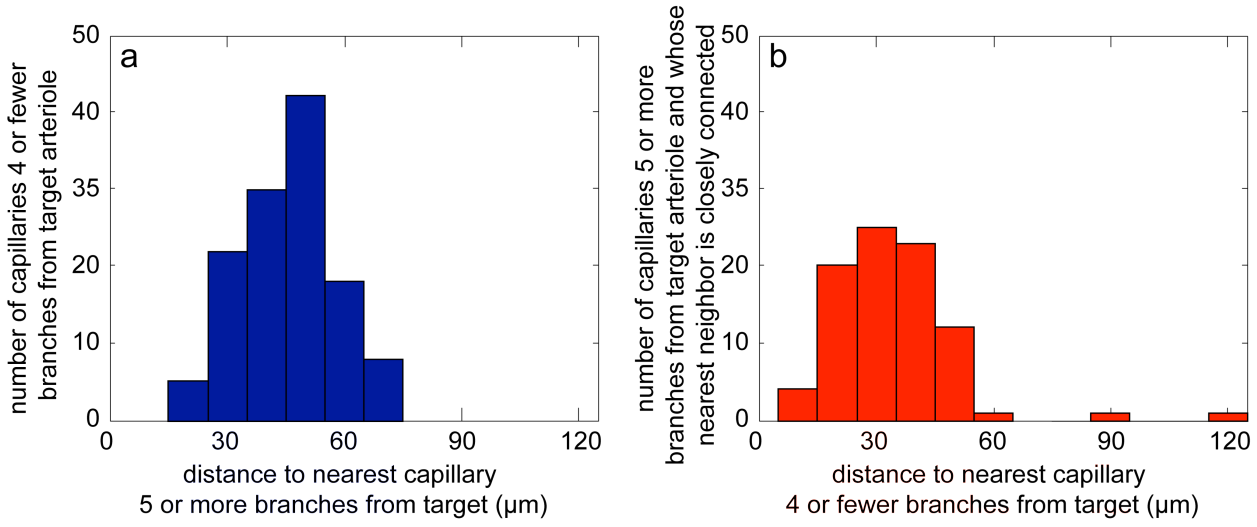

Supplementary Fig. 4.5 (a) Histogram of distances between closely connected capillaries and the nearest distantly connected capillary. (b) Histogram of distances between distantly connected capillaries and the nearest capillary for the subset of distantly connected capillaries that had a capillary that was closely connected to the target penetrating arteriole as their nearest neighbor.

Red blood cell flux decreased in capillaries downstream from a penetrating arteriole occlusion

RBC flux was severely reduced in the first four capillary branches downstream from a penetrating arteriole occlusion (Supplementary Fig. 4.6), reflecting the same tendencies as the RBC speed (Fig. 4.6c). ACh application did not improve RBC flux in the closest branches (Supplementary Fig. 4.6). On average, across all measured capillaries the RBC flux was 55 +/-40 RBC/s, which matches previously measured values for brain [15, 16].

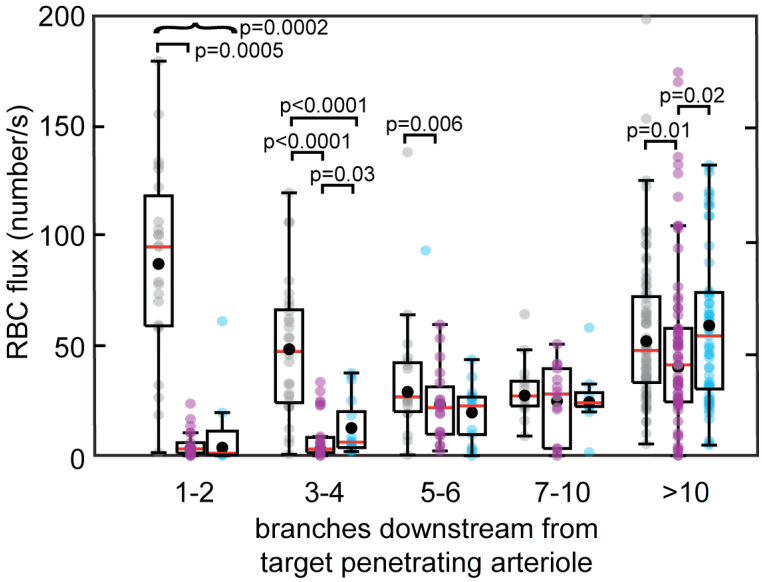

Supplementary Fig. 4.6 Flux dropped in downstream capillaries after penetrating arteriole occlusion. Flux in capillaries before, after clotting of a penetrating arteriole, and after ACh application as a function of the number of branches the capillaries are downstream from the occluded vessel. Square brackets indicate significant differences with Wilcoxon ranks sum test for paired data. Curly brackets indicate significant differences with Wilcoxon ranks sum test for unpaired data in one case in which not enough vessel pairs were measured for the paired test.

Post-hoc power analysis and sensitivity analysis

Our conclusion that there is no active arteriole compensatory response after the occlusion depends on observation of no vessel dilation. In order to estimate the probability of a Type II statistical error in which we have falsely concluded that there is no dilation, we conducted post-hoc sensitivity analysis. In this analysis we estimate the minimum change we should have been able to resolve given the number of measurements made and the measured variability in the data.

Arterioles after occlusion

In arterioles, the most important data that supports our conclusion that there was no significant dilation in the neighboring penetrating arterioles is summarized in Fig. 1f. For urethane, post-hoc analysis estimates the power of the study as 0.86. From sensitivity analysis we estimate that we should have been able to resolve a difference in change in diameters of 6.5% between the clot and control experiment with power = 0.95 and a 5% change with power = 0.8. We actually observed a reduction, rather than increase, in the mean vessel diameter of 6% in clot experiments relative to the controls, strongly suggesting there is no dilatory response in neighboring penetrating

arterioles after occlusion of one penetrating arteriole. With isoflurane, the results have less power (0.15), but sensitivity analysis suggests that with power 0.95 (0.8), we would have be able to detect a difference of 16% (12%) allowing us to conclude that we do not expect that there is a change in diameter greater than about 15% relative to control. What further bolsters our confidence in the conclusion that there was no dilation is that after ACh was applied to the cortical surface the same vessels were remeasured and we detected a statistically significant dilation difference of 9% of baseline diameters between the clot and the ACh timepoints (Fig. 4.6a).

For all other measurements in arterioles the differences between clot and control groups were small enough that all powers were <0.8, which is consistent with the hypothesis that there is little change in the arterioles after the occlusion so that the effect size is very small. Using sensitivity analysis, we estimate the minimum changes our study was likely to detect. Both RBC speed and RBC flow dropped relative to baseline with a clot, supporting that idea that there is no extra perfusion that goes to the territories surrounding the occluded arteriole. With urethane anesthesia, sensitivity analysis leads us to expect to be able to resolve a 15% differences in RBC speed and RBC flow between clot and control groups with 0.80 power. We cannot rule out a smaller change in speed and flow. With isoflurane, with fewer measurements, we place the upper limit of resolvable change in RBC speed at 30% differences. For RBC flow with isoflurane, we estimate sufficient sensitivity to detect a 33% change. In all cases, the trends are consistent with no dilation and no increase in flow or speed in the surrounding penetrating arterioles. All means and medians for both urethane and isoflurane were lower than the controls. We also did not observe a significant

difference in the behavior of communicating versus penetrating arterioles in diameter, speed or RBC flow (Fig. 4.2g-h). Sensitivity analysis estimates that we should have been able to resolve differences in vessel diameter changes of 12% with urethane between penetrating and communicating arterioles and 16% with isoflurane. In speed measurements and RBC flow calculations, communicating arteriole measurements had large variability, so we were unable to resolve differences less than about 50%. However, with both urethane and isoflurane, the speed and flow dropped relative to baseline, which is consistent with a lack of an active compensatory behavior.

Capillaries after occlusion

We also claim to see no significant speed changes in capillaries distant (more than 4 branches) from the occluded arteriole (Fig. 4.4a). Post-hoc analysis estimates power for groups 5-6, 7-10 and 10+ to be low (< 0.35) due to high variability and sensitivity analysis suggests that we cannot make conclusions about the percentage change in speed. However, looking at the magnitude of the speeds (rather than normalized by baseline speeds) when comparing the RBC speed at baseline to that after the occlusion as in Fig. 4.6, powers in groups up to 10 branches are all greater than 0.9 and sensitivity analysis for group 7-10 suggests that we should have been able to detect a difference in RBC speed of 0.08 mm/s. In the group of capillaries greater than 10 branches away, the power is only 0.18 and we cannot rule out speed changes less than 0.2 mm/s. However, the trend across branches downstream from the occluded vessel argues strongly for a decreasing effect of the occlusion on speed with increasing topological distance. We also do not see a change in RBC speed between the post-clot

measurement and the ACh application that reaches significance in most of the groups. Power is low in all branch groups, but we expected to be able resolve changes of 0.07 mm/s or less in all group up to 10 vessels away. In vessels more than 10 branches away, we cannot rule out changes less than 0.2mm/s and the trends suggest that there is actually an increase in RBC speed.

RBC flux in capillaries had similar trends to the speed (Supplementary Fig. 4.6). The data suggests that flux dropped in all groups of measured capillaries with the occlusion. ACh improved flow in some groups but not all. The power for the comparison of post-clot and ACh flux in group 1-2, 5-6, 7-10 is low <0.7 and sensitivity analysis suggests that we cannot rule out changes of less than 10 RBC/s.

We did not see significant dilation in capillaries five or more branches from the occluded arteriole relative to control (Fig. 4.4b). Power in the 5-6 branch group was 0.74, and we expected to be able to observe a 10% difference in changes in diameter relative to control with 0.80 power. In vessels 7-10 and more than 10 branches away power was <0.2, but we expected to be able to resolve difference in dilation of 12% and 3% respectively. The trend in the reduction of dilation with increasing branch numbers supports the idea that only the nearby vessels are affected.

We also do not see a change in capillary tube hematocrit with penetrating arteriole occlusion when compared to controls (Supplementary Fig. 4.3). For capillaries 1-4 branches downstream from the targeted penetrating arteriole, we would have expected to be able to resolve differences of about 16% between the clot and control. For capillaries more than 4 branches away, we expected to be sensitive to changes of 21%.

Sup Table 4.1: Physiological Monitoring

Physiological parameters were measured in most animals and values were averaged over each of the three stages of the experiment.

mean (standard deviation)

	mean arterial blood pressure (mmHg)				end-tidal % CO_2				% SpO_2			
	baseline	clot	ACh	n	baseline	clot	ACh	n	baseline	clot	ACh	n
urethane control	80 (22)	82 (20)		13	5.9 (1.0)	5.9 (1.1)		13	96 (2)	97 (1)		8
urethane clot	77 (15)	75 (21)	75 (16)	11	4.3 (1.2)	4.2 (1.2)	3.7 (0.8)	19	93 (3)	94 (1)	94 (1)	9
all urethane	80 (18)	78 (21)		24	5.0 (1.3)	4.9 (1.4)		32	95 (3)	96 (2)		17
isoflurane control	87 (5)	84 (16)		2	5.5 (0.8)	5.5 (0.9)		3	89 (5)	92 (3)		3
isoflurane clot	97 (21)	92 (22)		4	3.8 (1.4)	4.0 (1.5)		5				
all isoflurane	94 (17)	89 (19)		6	4.4 (1.4)	4.6 (1.4)		8				

Sup Table 4.2: Supplementary Data Tables

The following tables correspond to figures that include box plots and show the median, mean, number of vessels measured, the standard deviations and standard error of the mean of each column.

Figure 1

(f)

	Vessel diameter			
	Clot (%baseline)		Control (%baseline)	
	Urethane	Isoflurane	Urethane	Isoflurane
Mean	97	95	103	98
Median	97	95	103	99
n	96	39	94	73
Std Dev	14	23	14	24
SEM	1	4	1	3

(g)

	RBC speed			
	Clot (%baseline)		Control (%baseline)	
	Urethane	Isoflurane	Urethane	Isoflurane
Mean	90	94	94	97
Median	92	94	93	101
n	103	38	93	73
Std Dev	28	36	41	60
SEM	3	6	4	7

(h)

	RBC Flow			
	Clot (%baseline)		Control (%baseline)	
	Urethane	Isoflurane	Urethane	Isoflurane
Mean	87	88	93	90
Median	86	87	99	102
n	96	38	92	73
Std Dev	40	65	38	181
SEM	4	11	4	21

Figure 2

(a)

	Diameter (%baseline)			
	Urethane			
branches	**1-2**	**3-4**	**5-6**	**7+**
Median	97	98	93	99
Mean	99	98	95	97
n	13	30	28	25
SD	15	12	16	13
SEM	4	2	3	3
	Isoflurane			
branches	**1-2**	**3-4**	**5-6**	**7+**
Median	94	92	94	98
Mean	97	96	94	97
n	9	11	10	9
SD	26	18	27	24
SEM	9	5	9	8

(b)

	RBC speed (%baseline)			
	Urethane			
branches	1-2	3-4	5-6	7+
Median	82	101	86	93
Mean	90	98	87	91
n	15	31	29	28
SD	38	26	27	28
SEM	10	5	5	5
	Isoflurane			
branches	1-2	3-4	5-6	7+
Median	77	101	94.5	93
Mean	95	92	95	95
n	9	10	10	9
SD	41	32	42	31
SEM	14	10	13	10

(c)

	RBC flow (%baseline)			
	Urethane			
branches	1-2	3-4	5-6	7+
Median	79	87	85	86
Mean	77	99	85	85
n	13	30	28	25
SD	53	34	35	44
SEM	15	6	7	9
	Isoflurane			
branches	1-2	3-4	5-6	7+
Median	108	74	88	91
Mean	89	83	84	97
n	9	10	10	9
SD	46	36	72	95
SEM	15	11	23	11

(g)

	Diameter (%baseline)			
	Penetrating arteriole		Communicating arteriole	
	Urethane	Isoflurane	Urethane	Isoflurane
Median	97	95	97	99
Mean	97	95	105	105
n	96	39	21	29
SD	14	23	22	23
SEM	8	4	5	3

(h)

	RBC speed (%baseline)			
	Penetrating arteriole		Communicating arteriole	
	Urethane	Isoflurane	Urethane	Isoflurane
Median	92	94	70	89
Mean	90	94	72	85
n	103	38	21	29
SD	28	52	71	52
SEM	3	10	16	10

(i)

	RBC flow (%baseline)			
	Penetrating arteriole		Communicating arteriole	
	Urethane	Isoflurane	Urethane	Isoflurane
Median	86	87	83	91
Mean	87	88	65	95
n	96	38	21	29
SD	40	65	129	92
SEM	4	11	28	17

Figure 4

(a)

	RBC speed				
	Post - Clot (%baseline)				
branches	1-2	3-4	5-6	7-10	10+
Median	1	5	61	74	92
Mean	4	8	58	81	86
n	29	38	18	16	73
SD	11	35	71	68	72
SEM	2	6	17	17	8
	Control (%baseline)				
branches	1-2	3-4	5-6	7-10	10+
Median	98	81	80	63	104
Mean	102	88	86	114	98
n	18	16	11	4	21
SD	19	50	46	118	100
SEM	4	13	14	59	22

(b)

	Diameter				
	Post - clot (%baseline)				
branches	1-2	3-4	5-6	7-10	10+
Median	113	110	105	102	102
Mean	114	109	110	101	103
n	25	42	27	16	122
SD	16	16	14	10	16
SEM	3	2	3	2	1
	Control (%baseline)				
branches	1-2	3-4	5-6	7-10	10+
Median	100	102	101	98	100
Mean	102	101	102	99	101
n	25	21	19	7	65
SD	7	8	12	10	8
SEM	1	2	3	4	1

Figure 6

(a)

	Arterioles				Capillaries	
	Diameter (%baseline)		RBC flow (%baseline)		Diameter (%baseline)	
	clot	Ach	clot	Ach	clot	Ach
Median	97	102	86	117	105	108
Mean	97	106	87	122	106	107
n	96	72	96	72	233	175
SD	14	16	40	72	16	16
SEM	1	2	4	8	1	1

(b)

	Capillary diameter after clot (% of post clot diameter)				
branches	1-2	3-4	5-6	7-10	10+
Median	105	102	101	107	104
Mean	103	106	103	107	103
n	10	25	25	14	101
SD	13	12	14	8	13
SEM	4	2	3	2	1

(c)

	RBC speed (mm/s)					
branches	1-2			3-4		
	pre	clot	ACh	pre	clot	ACh
Median	1.5	0.0	0.0	0.4	0.0	0.1
Mean	1.6	0.1	0.1	0.6	0.1	0.2
n	29	29	14	40	38	25
SD	1.1	0.2	0.1	0.5	0.2	0.2
SEM	0.2	0.0	0.0	0.1	0.0	0.0
branches	5-6			7-10		
	pre	clot	ACh	pre	clot	ACh
Median	0.2	0.2	0.2	0.2	0.2	0.2
Mean	0.3	0.2	0.2	0.3	0.2	0.3
n	19	19	19	18	16	17
SD	0.3	0.1	0.1	0.2	0.2	0.3
SEM	0.1	0.0	0.0	0.0	0.1	0.1
branches	10+					
	pre	clot	ACh			
Median	0.5	0.4	0.5			
Mean	0.7	0.7	0.8			
n	73	73	62			
SD	0.8	0.9	0.9			
SEM	0.1	0.1	0.1			

Supplementary Figure 2

(a)

	Diameter			
	Amplified		Rose Bengal	
	Urethane	Isoflurane	Urethane	Isoflurane
Median	97	95	91	99
Mean	97	95	93	99
n	96	39	15	10
SD	14	23	15	8
SEM	1	4	4	3

(b)

	RBC speed			
	Amplified		Rose Bengal	
	Urethane	Isoflurane	Urethane	Isoflurane
Median	92	94	99	120
Mean	90	94	99	117
n	102	38	15	10
SD	29	36	41	28
SEM	3	6	10	9

(c)

	RBC flow			
	Amplified		Rose Bengal	
	Urethane	Isoflurane	Urethane	Isoflurane
Median	86	87	81	109
Mean	87	88	88	112
n	96	38	15	10
SD	40	65	42	19
SEM	4	11	11	6

Supplementary Figure 3

	post-clot hematocrit (% baseline)			
	1-4 branches		>4 branches	
	clot	control	clot	control
Median	104	93	94	96
Mean	99	93	97	103
n	18	14	50	28
SD	52	17	37	34
SEM	12	3	5	7

Supplementary Figure 6

	RBC flux (number/s)					
branches	1-2			3-4		
	pre	clot	ACh	pre	clot	ACh
Median	95	3	1	48	3	6
Mean	88	5	11	49	8	12
n	23	22	8	29	28	17
SD	44	6	21	30	10	13
SEM	9	1	8	6	2	3
branches	5-6			7-10		
	pre	clot	ACh	pre	clot	ACh
Median	27	22	23	28	28	24
Mean	35	23	20	30	25	31
n	19	19	18	15	14	13
SD	29	17	12	13	17	22
SEM	7	4	3	3	5	6
branches	10+					
	pre	clot	ACh			
Median	48	41	55			
Mean	56	49	59			
n	72	71	57			
SD	34	39	36			
SEM	4	5	5			

Tables corresponding to box plots showing median, mean, number of vessels, standard deviation and standard error of the mean for each column.

Supplementary movie

Movie url: http://www.nature.com/jcbfm/journal/v30/n12/extref/jcbfm2010157x3.mov

Three-dimensional rendering of vasculature shown in Fig. 4.3 using Voxx [17]. The targeted penetrating arteriole was colored in red.

SUPPLEMENTARY REFERENCES

1. Ley, K., Pries, A.R. & Gaehtgens, P. Topological structure of rat mesenteric microvessel networks. *Microvasc Res* **32**, 315-332 (1986).

2. Jiang, Z.L., Kassab, G.S. & Fung, Y.C. Diameter-defined Strahler system and connectivity matrix of the pulmonary arterial tree. *J Appl Physiol* **76**, 882-892 (1994).

3. Lipowsky, H.H. Microvascular rheology and hemodynamics. *Microcirculation* **12**, 5-15 (2005).

4. Schaffer, C.B., *et al*. Two-photon imaging of cortical surface microvessels reveals a robust redistribution in blood flow after vascular occlusion. *PLoS biology* **4**, e22 (2006).

5. Nishimura, N., *et al*. Targeted insult to subsurface cortical blood vessels using ultrashort laser pulses: three models of stroke. *Nature Methods* **3**, 99-108 (2006).

6. Nishimura, N., Schaffer, C.B., Friedman, B., Lyden, P.D. & Kleinfeld, D. Penetrating arterioles are a bottleneck in the perfusion of neocortex. *Proc Natl Acad Sci U S A* **104**, 365-370 (2007).

7. Watson, B.D., Dietrich, W.D., Busto, R., Wachtel, M.S. & Ginsberg, M.D. Induction of reproducible brain infarction by photochemically initiated thrombosis. *Annals of Neurology* **17**, 497-504 (1985).

8. Sigler, A., Goroshkov, A. & Murphy, T.H. Hardware and methodology for targeting single brain arterioles for photothrombotic stroke on an upright microscope. *J Neurosci Methods* **170**, 35-44 (2008).

9. Aarts, P.A., *et al*. Blood platelets are concentrated near the wall and red blood cells, in the center in flowing blood. *Arteriosclerosis* **8**, 819-824 (1988).

10. Furman, M.B. & Olbricht, W.L. Unsteady Cell Distributions in Capillary Networks. *Biotechnol. Prog.* **1**, 26-32 (1985).

11. Constantinescu, A.A., Vink, H. & Spaan, J.A. Elevated capillary tube hematocrit reflects degradation of endothelial cell glycocalyx by oxidized LDL. *Am J Physiol Heart Circ Physiol* **280**, H1051-1057 (2001).

12. Udden, M.M. In vitro sub-hemolytic effects of butoxyacetic acid on human and rat erythrocytes. *Toxicol. Sci.* **69**, 258-264 (2002).

13. Keller, M.W., Damon, D.N. & Duling, B.R. Determination of capillary tube hematocrit during arteriolar microperfusion. *Am J Physiol* **266**, H2229-2238 (1994).

14. Mchedlishvili, G., Varazashvili, M., Kumsishvili, T. & Lobjanidze, I. Regional hematocrit changes related to blood flow conditions in the arterial bed. *Clin. Hemorheol. Microcirc.* **29**, 71-79 (2003).

15. Kleinfeld, D., Mitra, P.P., Helmchen, F. & Denk, W. Fluctuations and stimulus-induced changes in blood flow observed in individual capillaries in layers 2 through 4 of rat neocortex. *Proceedings of the National Academy of Sciences USA* **95**, 15741-15746 (1998).

16. Villringer, A., Them, A., Lindauer, U., Einhaupl, K. & Dirnagl, U. Capillary perfusion of the rat brain cortex: An in vivo confocal microscopy study. *Circulation Research* **75**, 55-62 (1994).

17. Clendenon, J.L., Phillips, C.L., Sandoval, R.M., Fang, S. & Dunn, K.W. Voxx: a PC-based, near real-time volume rendering system for biological microscopy. *Am J Physiol Cell Physiol* **282**, C213-218 (2002).

CHAPTER FIVE

CORTICAL MICROHEMORRHAGES CAUSE LOCAL INFLAMMATION BUT DO NOT TRIGGER DENDRITE PATHOLOGY

This research was submitted to a peer-reviewed journal.

Nathanael L. Rosidi[1], Joan Zhou[1], Sanket Pattanaik[1], Peng Wang[2], Morgan Brophy[1], William L. Olbricht[1, 2], Nozomi Nishimura[1], Chris B. Schaffer[1]

[1]Department of Biomedical Engineering, Cornell University, Ithaca, NY 14853

[2]Department of Chemical and Biomolecular Engineering, Cornell University, Ithaca, NY 14853

ABSTRACT

Microhemorrhages are common in the aging brain, and their incidence is correlated with increased risk of neurodegenerative disease. Past work has shown that occlusion of individual cortical microvessels as well as large-scale hemorrhages can lead to degeneration of neurons and increased inflammation. Using two-photon excited fluorescence microscopy together with a laser-based approach to rupture individual microvessels in mice, we explored the consequences of a microhemorrhage on brain cells both acutely and over one week. We found that extravasated red blood cells compressed surrounding parenchymal tissue but did not crush capillaries and cause ischemia. Imaging of cortical dendrites revealed no degenerative changes up to seven days after the microhemorrhage. We observed a rapid microglia/macrophage inflammatory response up to 200 μm from the microhemorrhage that persisted over seven days. Taken together, our data suggest that a cortical microhemorrhage does not cause significant neural pathology but does trigger a sustained, local inflammatory response.

INTRODUCTION

Recent clinical evidence suggests that cortical microhemorrhages, while not producing acute stroke symptoms, are linked to increased risk of cognitive decline and dementia[1, 2]. Traditional animal models of hemorrhage, such as infusion of whole blood or injection of bacterial collagenase, have provided a means to study the physiological impact of large-scale intracerebral hemorrhages (ICH), which affect macroscopic regions of the cortex and do cause acute stroke[3]. However, these methods are unable to reproduce the microhemorrhages that likely stem from the rupture of a single small arteriole or capillary and may underlie aspects of cognitive decline. Due in part to this lack of good animal models, there remains an incomplete understanding of the acute and chronic cellular dynamics and pathophysiological events following microhemorrhage, making progress on therapeutic strategies difficult.

There are multiple potential mechanisms, identified in previous studies of large hemorrhages that may play a role in injuring brain cells after microhemorrhage. Acutely, increases in intracranial pressure and compression of brain tissue resulting from hematoma formation can mechanically injure cells[4] and can crush surrounding blood vessels, reducing cerebral blood flow (CBF) and causing ischemic pathology[5]. Over several days after ICH, additional injury to brain cells can be caused by oxidative stress and free radical damage from, for example, the byproducts of red blood cell (RBC) lysis, as well as by edema formation[6]. Hemorrhage also drives an inflammatory cascade, leading to microglia response and invasion of neutrophils and macrophages, which may exacerbate injury[7].

In this paper, we studied the timecourse and spatial extent of the pathological

consequences of a cortical microhemorrhage in mice. We ruptured individual, targeted arterioles in the cortex using femtosecond laser ablation, producing microhemorrhages[8] that are ~10,000 times smaller than those produced with existing ICH models[9] and that match the size of the microhemorrhages histologically observed in human brains[10]. We used two-photon excited fluorescence (2PEF) microscopy to track the acute and chronic effects of these microhemorrhages with micrometer-scale spatial resolution. We first quantified the extravasation dynamics of RBCs and blood plasma after microhemorrhage and determined that clotting limits the extent of bleeding. We then measured tissue compression caused by the hematoma and showed this compression was not sufficient to collapse nearby capillaries. Next, we examined structural changes in dendrite morphology, acutely and up to one week after microhemorrhage, and found no evidence of dendrite degeneration. Finally, we found microglia/macrophages responded within an hour after the microhemorrhage and increased in density near the lesion over one week. These data suggest that the pathological impact of a microhemorrhage from a single cortical blood vessel may be more dependent on inflammation-mediated injury rather than on direct neuronal degeneration.

METHODS

Transgenic animals

We used 25 adult C57BL/6 mice (~5 to 8 months of age, both sexes, 21-32 g in mass) expressing yellow fluorescent protein (YFP) in a subset of cortical neurons (YFP-H line; stock# 3782; The Jackson Laboratory)[48] for experiments to characterize bleed dynamics, tissue compression, and dendrite health after microhemorrhage. Data on microglia/macrophage recruitment after microhemorrhage was generated using C57BL/6 mice heterozygous ($CX_3CR1^{+/GFP}$ (5 mice)) and homozygous ($CX_3CR1^{GFP/GFP}$ (5 mice)) for a knock-in that replaces the CX_3CR1 fractalkine receptor with green fluorescent protein (GFP), leading to fluorescent labeling of resident microglia cells in the brain as well as in peripheral blood monocytes (CX_3CR1-GFP; stock# 5582; The Jackson Laboratory)[22]. Wild-type animals used in histology (6 mice) and heparin-infusion experiments (3 mice) were age-matched, non-transgenic littermates of the YFP-H animals.

Chronic cranial imaging window preparation

To prepare a chronic cranial window for imaging[47], mice were anesthetized using 5% isoflurane (VetOne) and maintained at 1.5-2%. Body temperature was kept constant at 37.5˚C with a heating blanket and thermometer (50-7053P; Harvard Apparatus). Glycopyrrolate (0.005 mg/kg mouse) (Baxter Healthcare Corp.) was administered intramuscularly while ketoprofen (5 mg/kg mouse) (Fort Dodge) and dexamethasone sodium phosphate (0.2 mg/kg mouse) (American Regent, Inc.) were both administered subcutaneously prior to surgery. A 5-mm diameter circular bilateral craniotomy was

performed over the parietal cortex. An 8-mm No. 1.5 glass cover slip (50201; World Precision Instruments) was then placed over the exposed brain and glued to the skull using cyanoacrylate (Loctite 495; Henkel) and dental cement (Co-Oral-Ite Dental Mfg Co.). Animals were administered 5% (wt/vol) glucose in physiological saline (1 ml/kg mouse) subcutaneously and gradually transitioned off isoflurane anesthesia. Mice were then administered ketoprofen (5 mg/kg mouse) every 24 hr for 72 hr and allowed a minimum of five days recovery before *in vivo* imaging and laser-induced microhemorrhaging. All animal procedures were approved by the Cornell University Institutional Animal Care and Use Committee.

Two-photon excited fluorescence microscopy

Before imaging sessions, mice were anesthetized with isoflurane (1.5-2%) and retro-orbitally injected with 0.1-mL of 2.5% (wt/vol) neutral (D1830; Invitrogen) or lysine-fixable (D1864; Invitrogen) Texas-Red dextran (70 kDa) in physiological saline to fluorescently label the blood plasma. Animals were transferred to a custom-built two-channel 2PEF microscope with 645/65 emission filters for Texas-Red and 517/65 filters for GFP and YFP. We used a 1045-nm, 1-MHz, 350-fs pulse train from a Yb-fiber oscillator/amplifier system (μJewel FCPA, IMRA Corp.) as the excitation source to image YPF-H mice, while a 920-nm, 87-MHz, 100-fs pulse train from a Ti:sapphire laser oscillator (MIRA HP; Coherent), pumped by a continuous wave laser (Verdi-V18; Coherent), was used to image GFP and Texas-Red in CX_3CR1-GFP mice.

Penetrating arteriole microhemorrhage by femtosecond laser ablation

We identified penetrating arterioles (PAs), i.e. arterioles that branch from the surface arteriole network and dive into the brain to feed capillary beds, as target vessels[14]. Before inducing a microhemorrhage, 2PEF image stacks spaced 1-μm apart in the axial direction were taken. The diameter and blood flow speed[11] of the target PA were also measured. Microhemorrhages were produced in the descending segment of the target PA ~20-100 μm below the surface of the brain in most experiments, or at a depth of ~300-500 μm for studies of the impact of a deep microhemorrhage on dendrite degeneration. To induce a microhemorrhage, femtosecond laser pulses were tightly focused (20X, 0.95 numerical aperture, water immersion objective; XLUMPlanFl (Olympus)) on the outer edge of the lumen of the target PA [11]. We used 50-fs duration laser pulses produced by a Ti:sapphire regenerative amplifier (Legend 1k USP; Coherent), pumped by a Q-switched laser (Evolution 15; Coherent) and seeded by a Ti:sapphire oscillator (Chinhook; Kapteyn-Murnane Laboratories Inc.) that was pumped by a continuous wave laser (Verdi-V6; Coherent, Inc). Briefly, a 10-pulse burst (1-kHz repetition rate) with an energy of about 500 nJ/pulse was applied. If the vessel did not rupture, the laser energy was increased by about 50%, and the vessel was irradiated again. This process was repeated until extravasation of RBCs and blood plasma into the parenchyma of the brain was observed. The required laser energy to trigger a microhemorrhage depended principally on the depth of the target vessel beneath the brain surface and the presence of large blood vessels on the surface of the brain above the target vessel. For each microhemorrhage, we used the minimum laser energy required to rupture the target vessel wall and initiate bleeding into the brain. 2PEF images of the bleeding dynamics were acquired over ~1 min after the

microhemorrhage. In addition, 2PEF image stacks of dendrites or microglia/macrophages along with the vasculature were taken 0.5 and 1.5 hours, then one, two and seven days after each microhemorrhage.

Characterization of RBC and plasma bleeding dynamics

2PEF movies of the bleeding dynamics after microhemorrhage were captured at 3.34 frames/s at the axial location where the vessel was ruptured for ~1 min with lateral optical resolution of ~1-μm (n = 14 microhemorrhages). During bleeding, we measured the diameter of the growing disk of fluorescently-labeled blood plasma, as well as the diameter of the growing core of non-fluorescent RBCs, which appeared as dark patches in the sea of fluorescence (>4 measurements at different angles at each timepoint). At 0.5 and 1.5 hours after microhemorrhage, the RBC core and plasma extravasation diameters were measured from a 20-μm maximum intensity projection of a 2PEF image stack, centered at the axial depth of the microhemorrhage. In some cases, we used tiled image stacks that were later stitched together to increase the area around the hemorrhage we could analyze. All 2PEF *in vivo* images were analyzed using ImageJ (NIH).

In addition, in three wild-type C57BL/6 mice we intravenously infused heparin before and during a microhemorrhage (n = 10 microhemorrhages). Prior to microhemorrhage induction, a jugular vein catheter was implanted and a 50-μL bolus of heparin (100 U/kg mouse, diluted in 500 μL saline) was infused. This was followed by a constant infusion of the heparin solution at 15-μL/min using a syringe pump (PHD2000; Harvard Apparatus). During the period of steady infusion, target PAs were

located and ruptured, and the bleeding dynamics quantified.

Quantification of tissue displacement after microhemorrhage

To calculate the tissue displacement after microhemorrhage, 2PEF images of fluorescently-labeled dendrites were analyzed using custom-written Matlab (The Mathworks, Inc) software that determined how far dendrites in the post-hemorrhage image shifted laterally compared to the pre-hemorrhage image. The 2PEF images were normalized by first subtracting background (average of the lowest 1% of pixel values) and then dividing by the maximum signal (average of the highest 1% of pixel values). We calculated the dendrite displacement by finding the shift along the *x*- and *y*-axes of a 50 X 50 pixel region of the post-hemorrhage image that maximized the normalized cross-correlation with the pre-hemorrhage image. To speed up computation and avoid artifacts due to correlation with unrelated dendrites, we considered only a 100 X 100 pixel region of the pre-hemorrhage image, centered on the post-hemorrhage region. The analyzed regions of the pre and post image were then shifted in ten pixel increments and the algorithm repeated until the dendrite displacement from all regions in the image was determined. Tissue displacement was radially averaged and displayed as a function of distance from the center of the microhemorrhage. For dendrites within about 50 μm of the microhemorrhage, the shape and orientation of the dendrites changed too much for a cross-correlation based algorithm to reliably determine tissue displacement. In this region, we manually identified the same dendrites before and after the microhemorrhage and measured their displacement. We verified overlap of manual and automated measurements between 100 and 150 μm

from the hemorrhage.

Modeling of tissue compression by a microhemorrhage

To describe the compression of brain tissue around a microhemorrhage, we adapted a model from Basser[12] that describes tissue displacement during fluid infusion into the brain. Briefly, we treated the tissue as a fluid-saturated poroelastic network in which the pores are too small to let RBCs into the tissue. The stress-strain relation for the fluid phase is written as

$$\underline{\underline{\sigma}}_f = -p_f \underline{\underline{I}} \qquad (1)$$

where $\underline{\underline{\sigma}}_f$ is the stress in the fluid, p_f is the pressure in the fluid phase, and $\underline{\underline{I}}$ is the unit tensor. For the solid phase, the stress-strain relation is written as

$$\underline{\underline{\sigma}}_s = 2G\underline{\underline{\varepsilon}}_s + \lambda(Tr\underline{\underline{\varepsilon}}_s)\underline{\underline{I}} \qquad (2)$$

where $\underline{\underline{\sigma}}_s$ is the stress in the solid, G and λ are Lame constants for the solid phase, and Tr indicates the trace operation. The strain tensor, $\underline{\underline{\varepsilon}}_s$, is the symmetric part of the gradient of the displacement vector, $\underline{u}_s$, of the solid phase,

$$\underline{\underline{\varepsilon_s}} = \frac{1}{2}\left[\underline{\nabla u_s} + (\underline{\nabla u_s})^T\right] \tag{3}$$

where T is the transpose operation. At mechanical equilibrium, the divergence of the total stress is zero,

$$\underline{\nabla} \cdot \left\{(1-\phi)\left[2G\underline{\underline{\varepsilon_s}} + \lambda(Tr\underline{\underline{\varepsilon_s}})\underline{\underline{I}}\right] - \phi p_f \underline{\underline{I}}\right\} = 0 \tag{4}$$

where ϕ is the tissue porosity. Substituting Eq. (1) into Eq. (4), we obtain Navier's equation,

$$\underline{\nabla} p_f = \frac{1-\phi}{\phi}\left[G\nabla^2 \underline{u_s} + (G+\lambda)\underline{\nabla}(\underline{\nabla} \cdot \underline{u_s})\right] \tag{5}$$

At mechanical equilibrium, $\underline{\nabla} p_f = \underline{0}$. Assuming spherical symmetry, the r-component of this equation can then be simplified to

$$\frac{d}{dr}\left(\frac{1}{r^2}\frac{d}{dr}\left(r^2 u_{sr}\right)\right) = 0 \tag{6}$$

where u_{sr} is the displacement of the solid phase in the radial direction. Integrating Eq. (6) twice, we find

$$u_{sr} = \frac{Ar}{3} + \frac{B}{r^2} \tag{7}$$

where A and B are unknown integration constants. As r approaches infinity, u_{sr} should be finite, implying $A = 0$. At $r = a_{RBC}$, where a_{RBC} is the steady-state radius of the cavity filled with RBCs after the microhemorrhage, the stress in the solid phase should equal the contact stress, τ_c, at the boundary between the surrounding tissue and the RBC core,

$$\left[(2G + \lambda) \frac{du_{sr}}{dr} + \lambda \frac{2u_{sr}}{r} \right]_{r=a_{RBC}} = -\tau_c \tag{8}$$

This boundary condition leads to

$$B = \frac{a_{RBC}{}^3 \tau_c}{4G} \tag{9}$$

The radial tissue displacement, u_{sr}, as a function of the center of the microhemorrhage, r, can then be written as:

$$\frac{u_{sr}}{a_{RBC}} = \frac{\tau_c}{4G} \left(\frac{r}{a_{RBC}} \right)^{-2} \tag{10}$$

The unknown contact stress, τ_c, was then determined by fitting equation (10) to the

experimentally measured tissue displacement.

Analysis of dendrite degeneration after microhemorrhage

Using 2PEF image stacks taken acutely and out to one week after microhemorrhage, we classified individual dendrites within 150 μm of the lesion as intact or degenerated based on the presence of dendrite blebs (i.e. circular swellings along the dendrite path)[39]. We counted all dendrites in sub-regions of 2PEF image stacks taken from the same volumes within 150 μm of the center of the microhemorrhage across all timepoints in each animal (n = 24 microhemorrhages in 16 mice). Approximately 10-40 dendrites were identified in each sub-region and each dendrite was classed as showing evidence of degeneration or not. Control regions were at least 1.5-mm away from the microhemorrhage or on the contralateral side. The dendrite exclusion diameter was determined by measuring the distance between the closest dendrites along a line through the center of the microhemorrhage core (average of 4 measurements).

Photothrombotic stroke model

A 532-nm continuous wave laser (Compass 215M, Coherent, Inc.) was added to the 2PEF microscope so that the green light was focused through the microscope objective at the imaging plane[11]. After chronic window implantation and recovery, animals were anesthetized, a photosensitizer dye, rosebengal (RB) (0.03-mg/g mouse diluted at 10-mg/ml in saline), was retro-orbitally injected, and clotting was initiated by focusing ~5-mW of 532-nm laser light onto the target PA at the surface of the brain for five

minutes. Dendrite degeneration was analyzed as described above.

Analysis of microglia/macrophage dynamics after microhemorrhage

We manually counted the number of microglia/macrophage cell bodies as a function of distance from the center of the microhemorrhage using 2PEF image stacks taken acutely and out to one week after the lesion for heterozygous and homozygous CX_3CR1-GFP mice. We also identified microglia/macrophages that responded to the microhemorrhage by analyzing the polarity of cellular processes. A cell was determined to be responding if more than 50% of the processes were directed, within a 30-degree cone, toward the center of the microhemorrhage. The microglia/macrophage exclusion diameter was measured as the distance between the closest cellular processes along a line through the center of the microhemorrhage core (average of 4 measurements per hemorrhage). The maximum distance of microglia/macrophage response was defined as the distance from the center of the microhemorrhage to the farthest cell that directed the majority of its processes towards the lesion site (average of 4-8 measurements per hemorrhage).

Post-mortem histology

We performed histology seven days after rupturing individual PAs in six C57BL/6 mice (n = 16 microhemorrhages located within the first 100 μm of the brain surface). Animals were transcardially perfused with 15 ml of phosphate buffered saline (PBS) (Sigma-Aldrich) and 30 ml of 4% (wt/vol) paraformaldehyde (Fisher Scientific) in PBS. The brain was extracted from the skull and cryoprotected by immersion in 30%

(wt/vol) sucrose in PBS for 24 hr and then in 60 % (wt/vol) sucrose in PBS. To facilitate identification of individual microhemorrhages in histological sections, fiducial marks were made at known locations relative to the microhemorrhage sites by insertion of a 30-gauge needle into the brain. The tissue was frozen and cut into 25-μm thick coronal sections on a cryostat and mounted onto microscope slides (Superfrost Plus, Fisher Sci.).

To label RBC breakdown products and neurons, we used Prussian blue and cresyl violet staining, respectively. Brain sections were dehydrated in a graded series of ethanol, immersed in deionized water (dH_2O), then incubated in a 1:1 solution of 20% hydrochloric acid and 10% potassium ferrocyanide. Sections were rinsed with dH_2O and incubated with cresyl violet solution (5% in dH_20), then rinsed with dH_2O, dehydrated in a graded series of ethanol, immersed in xylene, mounted using Permount (Fisher Scientific) and a coverslip was attached. Sections were imaged on a white-light microscope (Axio Examiner; Zeiss).

To visualize astrocyte activation, we immunostained for glial fibrillary acidic protein (GFAP)[49]. Brain sections were rinsed in 0.5% TritonX-100 (Sigma-Aldrich) before overnight incubation with a primary mouse monoclonal anti-GFAP antibody (G3893; Sigma) in a 1:400 dilution in PBS. Sections were then rinsed with PBS and incubated with a 1:500 dilution of a secondary FITC-conjugated donkey anti-mouse IgG antibody (Jackson ImmunoResearch) in PBS. Fluorescent images were collected on a wide-field fluorescent microscope (Axio Examiner; Zeiss) from sections with both primary and secondary antibody, as well as sections containing only the secondary antibody, using identical exposure settings. No staining was observed in

sections where the primary antibody was not applied.

Statistical analysis

A p-value of less than 0.05 was considered statistically significant. Data were tested for normality using a Lilliefors two-sided goodness-of-fit test. The Mann-Whitney U test was used on data populations that were non-parametric, while a Student's t-test was performed on parametric data. The Pearson Product-Moment correlation coefficient was used for statistical correlations on all non-parametric data while an analysis of covariance was used on all parametric data populations.

RESULTS

We used 2PEF imaging to visualize bleeding dynamics and tissue displacement immediately following the microhemorrhage of single PAs in the cortex of mice, and followed the inflammatory response and changes in dendrite structure over seven days after the lesion. The target PAs had a diameter of 19.1 +/- 6.7 μm (mean +/- standard deviation) and a centerline RBC speed of 11.3 +/- 6.2 mm/s. Microhemorrhages were produced by focusing femtosecond-duration laser pulses, 100 to 1500 nJ in energy, on the edge of the vessel lumen of the descending segment of a PA[8]. Nonlinear absorption of laser energy ruptured the vessel wall which enabled RBCs and blood plasma to enter the brain parenchyma.

Bleeding of a ruptured cortical penetrating arteriole produced a ~100-μm diameter hematoma, while blood plasma penetrated five times farther into the brain

Immediately after the rupture of a single PA, RBCs and blood plasma exited the lumen of the vessel and entered the brain parenchyma (Fig. 5.1b). The region immediately surrounding the target PA filled with densely packed RBCs that largely excluded the fluorescently-labeled blood plasma and thus appeared dark in the 2PEF image. This RBC core was surrounded by a ring of fluorescence, indicating extravasated blood plasma (Fig. 5.1a)[11]. The diameter of the RBC core expanded to 78 +/- 23 (mean +/- standard deviation; 14 hemorrhages in 11 mice) within 3 s and stabilized at 100 +/- 31 μm after 0.5 hrs (Fig. 5.1c). The blood plasma entered further into the parenchyma, reaching a diameter of 119 +/- 50 within 3 s, continued rapid expansion over 30 s, and

stabilized at a diameter of 504 +/- 237 μm after 0.5 hr (Fig. 5.1d; 13 hemorrhages in 11 mice). The bleeding time, characterized as the time required to reach half the final diameter, was 0.66 s for RBCs and 17 s for blood plasma. In repeated imaging experiments over one week (see below), we never observed any evidence of repeat bleeding of the ruptured vessel.

Fig. 5.1 Dynamics of RBC and blood plasma extravasation after laser-induced microhemorrhage. (a) Maximum intensity projection of a 2PEF image stack of cortical dendrites (green) and blood vessels (red), before and 1.5 hr after microhemorrhage. The spatial extent of the RBC core (blood plasma) is represented by a yellow (white) outline. **(b)** 2PEF imaging of bleeding dynamics after rupture of a single PA. Dendrites were displaced by extravasating RBCs (yellow outline in top panels). A RBC-filled core (yellow outline in bottom panels) and diffuse plasma (white outline) expanded into the parenchyma after PA irradiation. **(c)** RBC core and **(d)** blood plasma diameter as a function of time after microhemorrhage. The red bold lines are running medians of the diameters from individual hemorrhages (black lines). **(e)** Median RBC core diameter as a function of time for mice receiving heparin infusion (green) and controls (red). Bold lines are running medians with 95% confidence intervals indicated by shaded areas. **(f)** RBC core diameter as a function of time for a PA that was irradiated twice (indicated by red pulses).

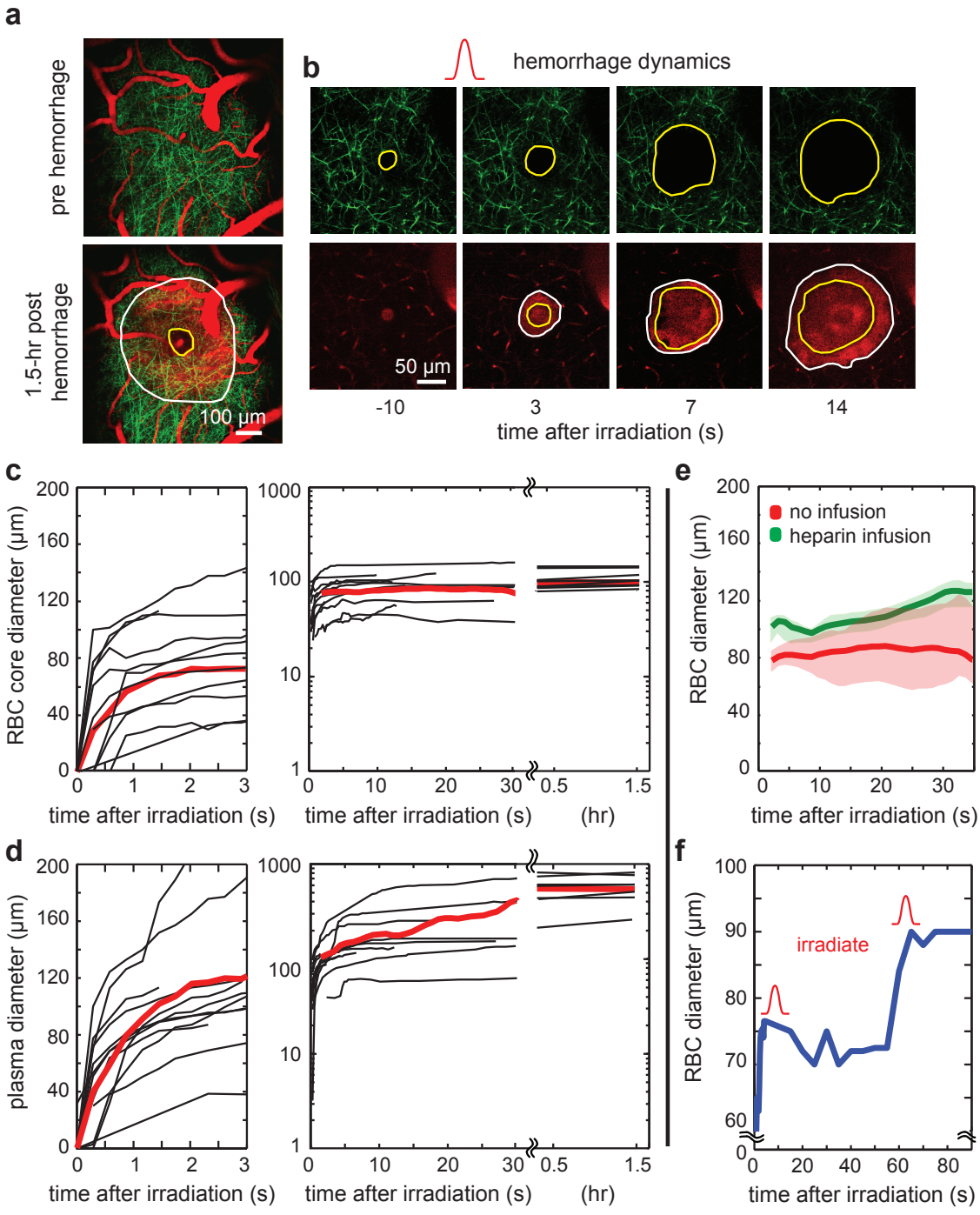
a
pre hemorrhage
1.5-hr post hemorrhage
100 μm
b
hemorrhage dynamics
50 μm
-10
3
7
14
time after irradiation (s)
c
RBC core diameter (μm)
time after irradiation (s)
time after irradiation (s)
(hr)
d
plasma diameter (μm)
time after irradiation (s)
time after irradiation (s)
(hr)
e
RBC diameter (μm)
no infusion
heparin infusion
time after irradiation (s)
f
RBC diameter (μm)
irradiate
time after irradiation (s)

Hematoma size was increased by administration of anticoagulants

To understand what limited the size of the microhemorrhage, we intravenously administered the anticoagulant heparin and ruptured PAs. We found heparin increased the final RBC core diameter measured at 1 min after microhemorrhage by 34% to 133.7 +/- 20.7 μm (Fig. 5.1e; $p < 0.006$; student t-test), and increased the RBC bleeding time to 1.37 s ($p < 0.016$; Mann-Whitney U test) (10 microhemorrhages in 3 mice). In one example, we irradiated a PA a second time after the RBCs stopped expanding and observed that the RBC core diameter grew by 25% after the second irradiation (Fig. 5.1f). The larger average RBC diameter with heparin and the increase in RBC core size after a second irradiation suggested that clotting of the vessel wall was a dominant limiting factor in microhemorrhage size. The ~25 times longer bleeding time for blood plasma as compared to RBCs suggests that the clot was initially porous, enabling blood plasma (but not RBCs) to exit the vessel.

Microhemorrhages compressed surrounding tissue but did not collapse nearby capillaries

We analyzed the spatial extent and magnitude of the compression of tissue surrounding a microhemorrhage by the extravasation of RBCs. We used 2PEF images of the apical dendrites of layer V pyramidal neurons to measure the direction and magnitude of the tissue displacement due to RBC and plasma extravasation as a function of distance from the microhemorrhage (Fig. 5.2a and 5.2b). A maximum tissue compression of around 20 μm was observed at the edge of the RBC core, which decreased to a few micrometers within 50 μm from the end of the RBC core (Fig.

5.2c). To group tissue compression data across multiple lesions (10 microhemorrhages in 8 mice), we defined a normalized distance from the center of the microhemorrhage by dividing the distance from the center of the microhemorrhage, r, by the RBC core radius, a_{RBC}, for each microhemorrhage. Fitting the average tissue displacement as a function of this normalized distance to Eq. (10), we found the contact stress between the RBC core and the surrounding tissue to be 1.5 kPa, assuming a shear modulus of brain tissue, G, of 2 kPa, and taking the average RBC core radius to be 50 μm (Fig. 5.2d)[12].

To determine if this tissue compression caused nearby capillaries to collapse, potentially causing ischemia, we identified individual capillary segments within 75 μm of the RBC core in image stacks taken before and 1.5 hr after the microhemorrhage (Fig. 5.2e). We classed these segments as stalled or flowing based on the motion of RBCs within the lumen. Of 240 capillary segments (11 micorhemorrhages in 8 mice) only one capillary was missing and three capillaries were stalled after the microhemorrhage (Fig. 5.2f), indicating that microhemorrhages did not lead to a substantial reduction in the number of flowing capillaries in the nearby brain tissue.

Fig. 5.2 Tissue displacement after a microhemorrhage. (a) Maximum intensity projections of 2PEF image stacks of cortical dendrites before and 1.5 hr after a microhemorrhage. **(b)** Tissue displacement map representing the magnitude and direction of dendrite displacement after the microhemorrhage shown in panel (A). Blue arrows represent shifts measured by the cross-correlation algorithm while red arrows represent manual displacement measurements. **(c)** Radially-averaged dendrite displacement as a function of distance from the center of the microhemorrhage for the example in panels (a) and (b). Manual (red) and automated (blue) measurements are both shown. **(d)** Average dendrite displacement (black circles) and fit to Eqn. (10) (green line) as a function of normalized distance from the center of the microhemorrhage. **(e)** Maximum intensity projections of 2PEF image stacks of blood vessels in the vicinity of the RBC core (yellow outline) before and 1.5 hr after a microhemorrhage. **(f)** Classification of capillary segments within 75-μm from the center of the microhemorrhage, identified before the lesion, as flowing, stalled, or missing at 1.5 hr after the lesion. Error bars represent binomial 95% confidence intervals.

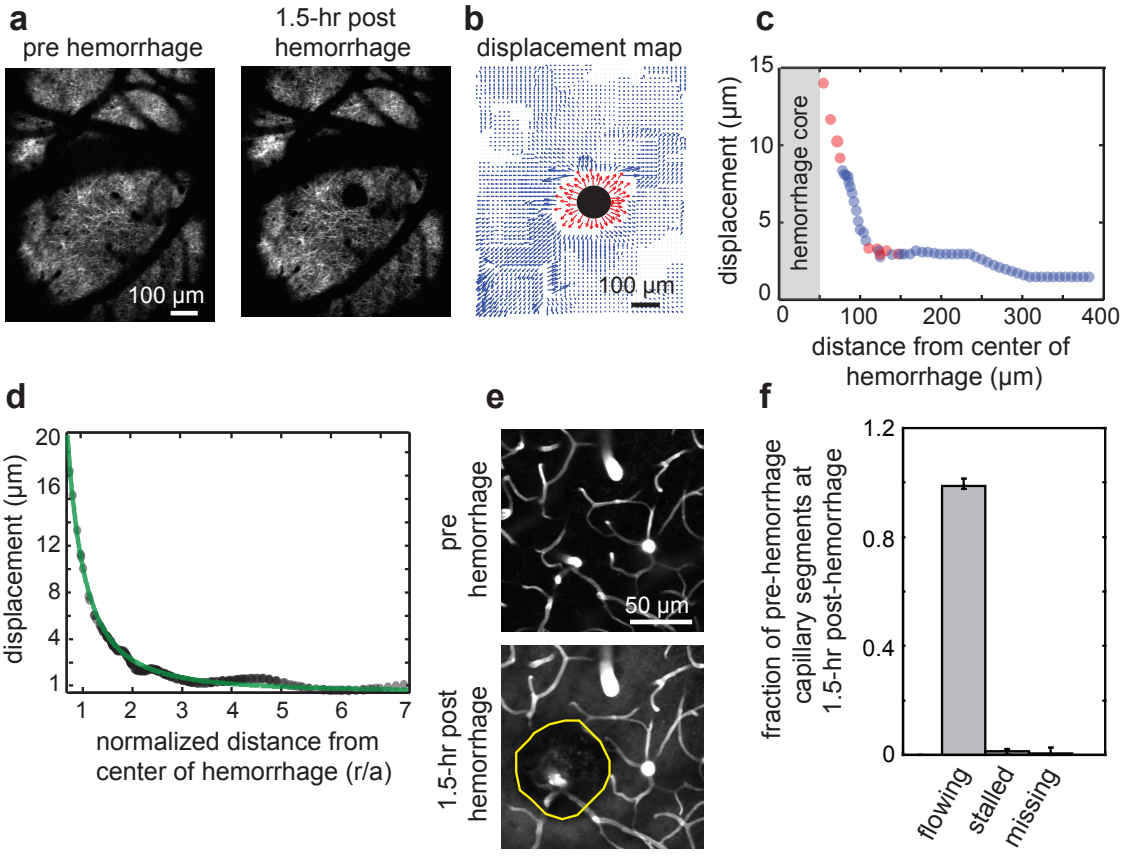
a
pre hemorrhage
1.5-hr post hemorrhage
100 μm
b
displacement map
100 μm
c
displacement (μm)
hemorrhage core
distance from center of hemorrhage (μm)
d
displacement (μm)
normalized distance from center of hemorrhage (r/a)
e
pre hemorrhage
50 μm
1.5-hr post hemorrhage
f
fraction of pre-hemorrhage capillary segments at 1.5-hr post-hemorrhage
flowing
stalled
missing

No acute or chronic dendrite degeneration was observed after microhemorrhage, and displaced dendrites relaxed back over several days

To assess the impact of cortical microhemorrhages on neuronal health, we evaluated morphological changes characteristic of dendrite degeneration (i.e. appearance of blebs) in the apical tufts of layer V pyramidal neurons acutely and over seven days following a microhemorrhage produced within the top 100 μm of the cortex (16 hemorrhages in 10 mice; Fig. 5.3a). Immediately after the microhemorrhage, we found no degeneration of the displaced dendrites surrounding the RBC-filled core (Fig. 5.3a). Over the following week, we saw no change in the number of dendrites (Fig. 5.3e), as well as no increase in the number of dendrites showing degenerative changes near the microhemorrhage as compared to control regions (8 control regions in 7 mice; Fig. 5.3b and 5.3f). We also placed microhemorrhages near the layer V neuronal cell bodies (300 – 500 μm below the cortical surface) and again saw no change in the number of dendrites and no increase in the number of degenerating dendrites (4 hemorrhages in 3 mice; Fig. 5.3c, 5.3e, 5.3f). In contrast, photothrombotic occlusion of a single PA[13, 14] led to a rapid and nearly complete degeneration of nearby dendrites that persisted to one week (4 clots in 5.3 mice; Fig. 5.3d), evidenced by both a decrease in the number of identifiable dendrites and the presence of degenerative changes on nearly all remaining dendrites (Fig. 5.3e and 5.3f). After one week, more dendrites were identifiable in the periphery of the imaged area (Fig. 5.3e), while a dark volume with no dendrites or fluorescent debris suggested an ischemic infarct (Fig. 5.3d).

Fig. 5.3 Acute and chronic imaging of dendrite morphology after microhemorrhage. Maximum intensity projections of 2PEF image stacks of cortical dendrites **(a)** after microhemorrhage of a single PA at 20-100 μm beneath the cortical surface (shallow hemorrhage), **(b)** in control regions, **(c)** after microhemorrhage of a single PA at 300-500 μm beneath the cortical surface (deep hemorrhage), and **(d)** after photothrombotic clotting of a single PA (RB clot). **(e)** Average number of dendrites in a fixed volume, normalized to the number identified 1.5 hr after the microhemorrhage, as a function of time for shallow and deep microhemorrhages, photothrombotic clots, and control regions. **(f)** Fraction of identified dendrites showing degenerative changes as a function of time **(g)** Dendrite exclusion diameter as a function of time after microhemorrhage (black). Red symbols indicate RBC core size. Error bars represent standard error of the mean (SEM). P-values compared to control region: ** $p<0.01$, *** $p<0.001$, # $p<0.0001$, ## $p<0.00001$; Mann Whitney U test.

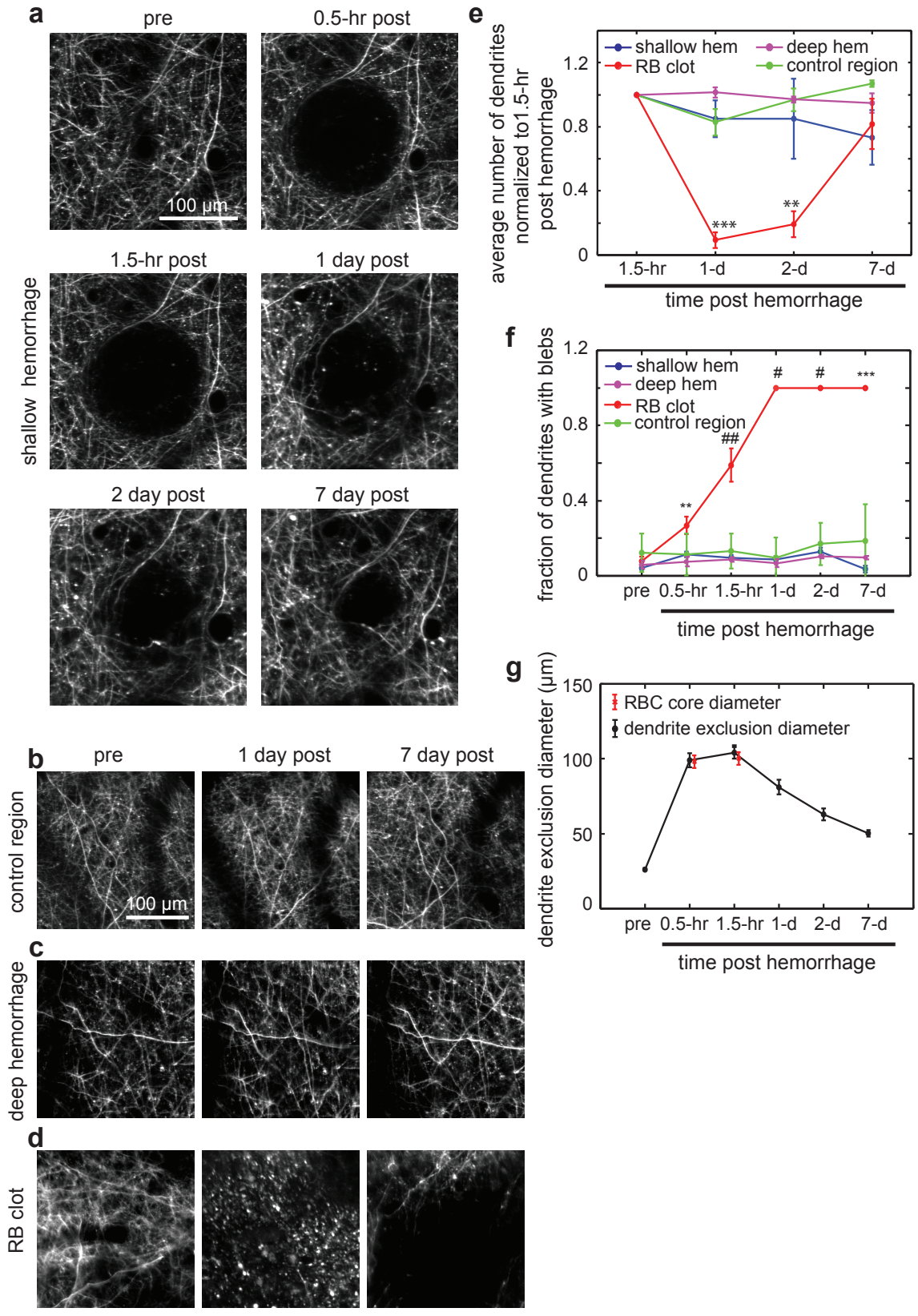
a
pre
0.5-hr post
100 μm
1.5-hr post
1 day post
shallow hemorrhage
2 day post
7 day post
b
pre
1 day post
7 day post
control region
100 μm
c
deep hemorrhage
d
RB clot
e
average number of dendrites normalized to1.5-hr post hemorrhage
shallow hem
deep hem
RB clot
control region
1.2
0.8
0.4
0
***
**
1.5-hr
1-d
2-d
7-d
time post hemorrhage
f
fraction of dendrites with blebs
shallow hem
deep hem
RB clot
control region
1.2
0.8
0.4
0
**
##
#
#
***
pre
0.5-hr
1.5-hr
1-d
2-d
7-d
time post hemorrhage
g
dendrite exclusion diameter (μm)
RBC core diameter
dendrite exclusion diameter
150
100
50
0
pre
0.5-hr
1.5-hr
1-d
2-d
7-d
time post hemorrhage

The extravasated RBCs from a microhemorrhage displaced dendrites, creating a dendrite-free region of 100 +/- 36-μm diameter (0.5-hr post-hemorrhage), consistent with the average diameter of the RBC core (Fig. 5.3g). Beginning one day after the microhemorrhage dendrites migrated back into the region from which they were excluded, approaching the baseline exclusion diameter after seven days (Fig. 5.3g).

Microglia/macrophage density near a microhemorrhage increases after one day and persists beyond a week

Next, we sought to examine the inflammatory response to cortical microhemorrhage. 2PEF imaging of microglia/macrophages in heterozygous and homozygous CX_3CR1-GFP mice (Fig. 5.4a) revealed an increase in microglia/macrophage density within 100 μm of the lesion beginning at one day and persisting beyond one week (Fig. 5.4b; heterozygous $p<0.01$, homozygous $p<0.05$; analysis of covariance; 5 (6) microhemorrhages in 4 (5) heterozygous (homozygous) mice). Microglia/macrophage density neither increased nor decreased at larger distances from the microhemorrhage.

Microglia/macrophages rapidly responded to the microhemorrhage by directing processes toward the injury and into the RBC-filled core

We next analyzed the spatial scale and temporal dynamics of microglia/macrophage responses after microhemorrhage. We measured the distance from the center of the hemorrhage to the farthest responsive cell, defined as a microglia/macrophage with more than half of its processes directed towards the site of injury. Within 1.5 hours, cells out to 200 μm from the center of the microhemorrhage were responsive for both

heterozygous and homozygous mice and this distance decreased over a week (Fig. 5.4c). In addition, we found that the fraction of microglia/macrophages near the microhemorrhage that responded peaked at 1.5 hours after the lesion (~75% responding) and decreased over the following week (Fig. 5.4d). To decouple the microglia/macrophage response due to laser ablation from the response due to the extravasation of blood components, we performed parenchymal tissue ablation using a laser energy similar to that used to induce a microhemorrhage. We found that the furthest responsive microglia was about 60 μm from the injury (3 ablations in 1 heterozygous mouse).

Fig. 5.4. Acute and chronic imaging of microglia/macrophage response after microhemorrhage. (a) Maximum intensity projection of 2PEF image stacks of microglia/macrophages (green) and blood vessels (red) before and after microhemorrhage (left). Chronic dynamics of microglia/macrophage behavior after microhemorrhage (right). Inset at right shows reactive processes invading the RBC-filled core (indicated by yellow outline) at 1.5 hr after the lesion. **(b)** Microglia/macrophage density relative to baseline at different distances from the microhemorrhage as a function of time for homozygous and heterozygous CX_3CR1-GFP mice (p-value compared to control: * <0.05, †† <0.01; analysis of covariance). **(c)** Maximal distance from the center of the microhemorrhage to the furthest responsive microglia/macrophage as a function of time after the lesion. Red symbol indicates distance to furthest responsive cell after laser ablation in the cortical parenchyma with an energy similar to that used to induce a microhemorrhage. **(d)** Fraction of microglia/macrophages with processes directed toward the lesion after a microhemorrhage (p-value compared to control for homozygous (heterozygous) mice: * (†) p<0.05, ** (††) p<0.01, *** (†††) p<0.001, # (%) p<0.0001, ## (%%) p<0.00001). **(e)** Diameter of region where microglia/macrophages are excluded after microhemorrhage as a function of time. Average RBC core diameter for the heterozygous (homozygous) animals is indicated in green (red) at 0.5 and 1.5 hr post hemorrhage. Error bars represent the standard error of the mean (SEM).

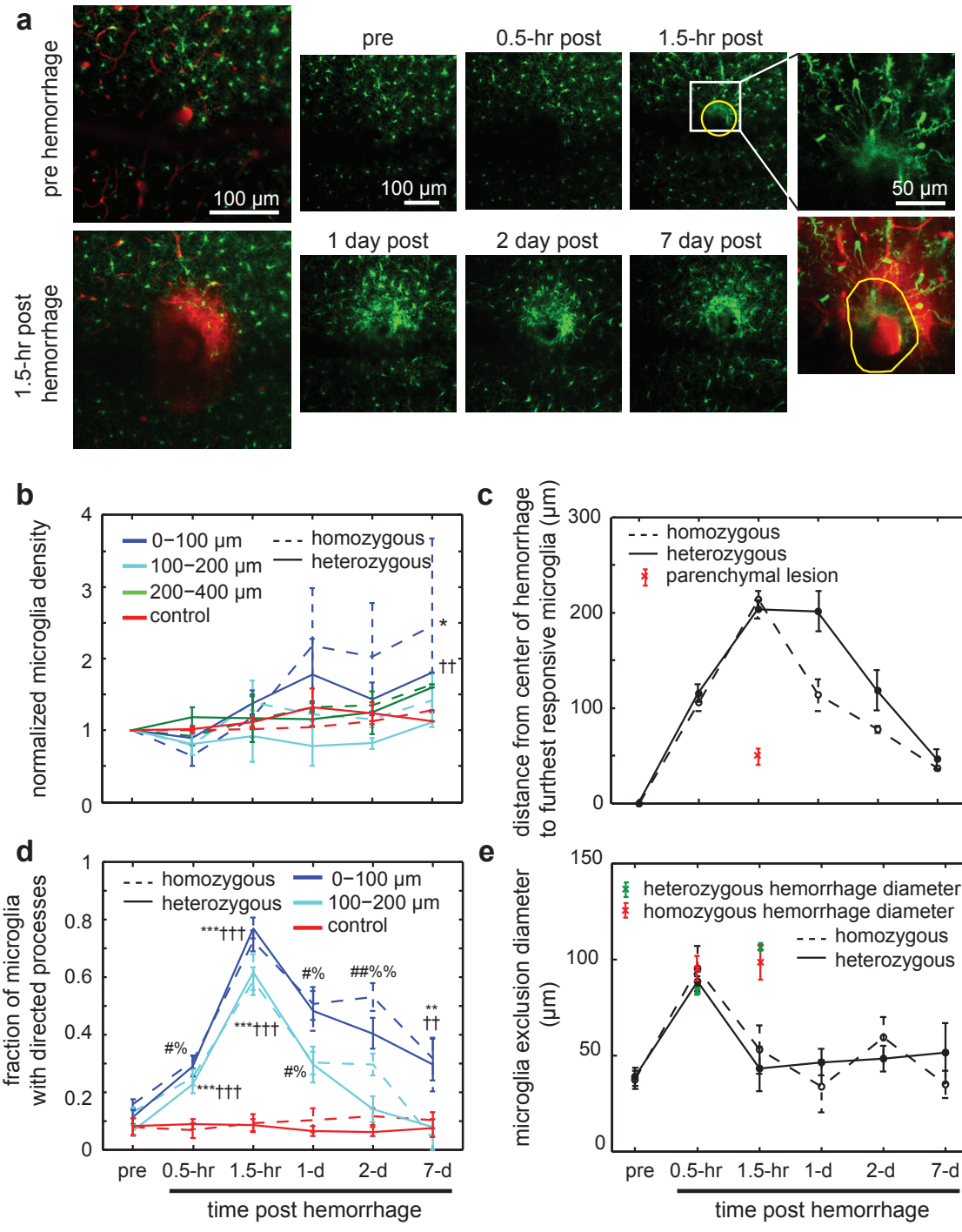
a
pre hemorrhage
pre
0.5-hr post
1.5-hr post
100 µm
100 µm
50 µm
1.5-hr post hemorrhage
1 day post
2 day post
7 day post
b
normalized microglia density
0–100 µm
100–200 µm
200–400 µm
control
homozygous
heterozygous
c
distance from center of hemorrhage to furthest responsive microglia (µm)
homozygous
heterozygous
parenchymal lesion
d
fraction of microglia with directed processes
homozygous
heterozygous
0–100 µm
100–200 µm
control
pre
0.5-hr
1.5-hr
1-d
2-d
7-d
time post hemorrhage
e
microglia exclusion diameter (µm)
heterozygous hemorrhage diameter
homozygous hemorrhage diameter
homozygous
heterozygous
time post hemorrhage

Microglia/macrophage cell bodies were displaced by extravasated RBCs immediately after the microhemorrhage. However, in both heterozygous and homozygous mice, microglia/macrophages extended processes into the RBC core as early as 1.5 hours after the microhemorrhage (Fig. 5.4a and 5.4e), further indicating rapid cellular response to the lesion.

GFAP was upregulated in astrocytes seven days after microhemorrhage but no infarction was observed

To corroborate our findings of increased inflammation with no neuron degeneration after a microhemorrhage, we analyzed astrocyte activation and tissue structure using post-mortem histology. Seven days after microhemorrhage, mice were euthanized and perfused (16 microhemorrhages in 6 mice). GFAP immunohistology showed astrocyte activation, indicative of an inflammatory response, in cells up to about 200 μm from the microhemorrhage (Fig. 5.5a). Punctate, iron deposits spanning a diameter of ~100μm were observed using Prussian blue staining, but no loss of neurons (visualized by Nissl staining) or tissue infarction was seen (Fig. 5.5b).

Fig. 5.5 Astrocyte activation and RBC breakdown products seven days after microhemorrhage. (a) Immunohistology for GFAP in coronally-sectioned tissue at lesion site and contralateral control region. **(b)** Bright-field image of coronally-sectioned tissue stained with cresyl violet (pink) and Prussian blue (black).

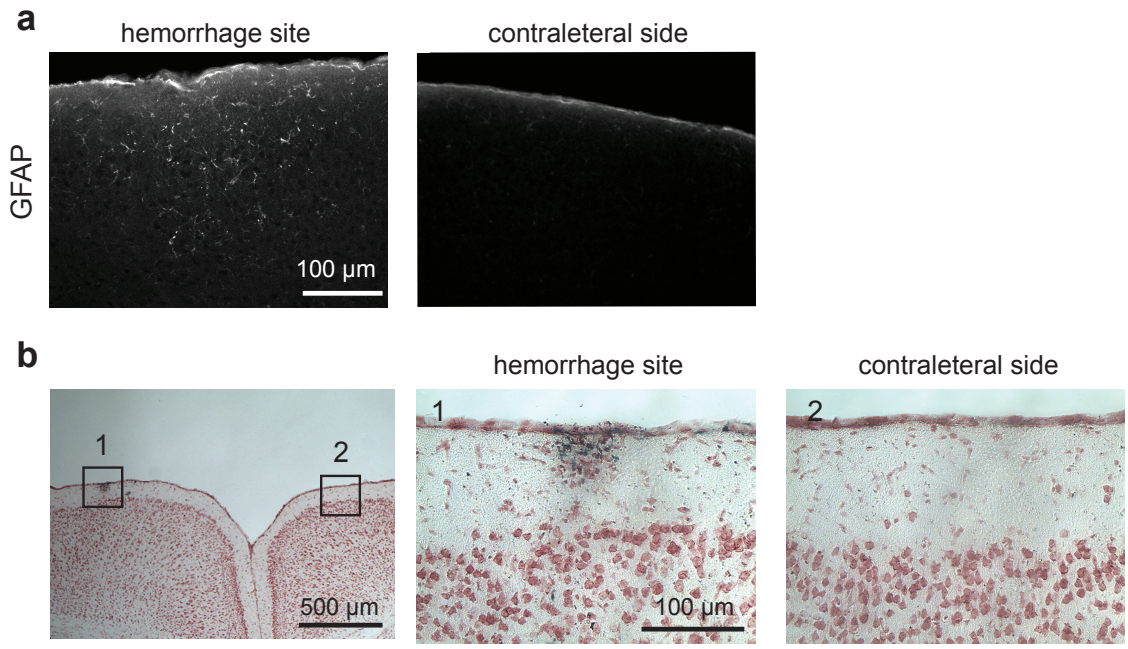
a
hemorrhage site
contraleteral side
GFAP
100 μm
b
hemorrhage site
contraleteral side
1
2
500 μm
1
100 μm
2

DISCUSSION

We used femtosecond laser ablation to rupture individual, targeted PAs in mice[11], to mimic the 100-μm sized hemorrhagic lesions found to be correlated with dementia and cognitive decline in humans[10, 15, 16]. We then followed the dynamics of multiple cellular constituents of the brain using chronic 2PEF imaging, allowing us to determine the physiological consequences of a microhemorrhage over seconds to weeks after the lesion was created. Immediately after microhemorrhage, RBCs and blood plasma extravasated 50 μm and 250 μm, respectively, from the ruptured vessel into the parenchymal tissue, respectively (Fig. 5.1). Microglia/macrophages responded within hours up to 200 μm from the microhemorrhage and sent cellular processes into the RBC core (Fig. 5.4). The tissue compression from the extravasated RBCs displaced cortical dendrites and microglia, but did not lead to dendrite degeneration or interruption of blood flow in nearby brain capillaries (Fig. 5.2). Over days following the microhemorrhage, displaced cortical dendrites returned to the region that was filled with RBCs (Fig. 5.3), microglia/macrophage density within 100 μm of the lesion increased, while the number of responsive microglia/macrophages outside this region decreased toward baseline over one week (Fig. 5.4).

Microvascular bleeding is limited by clotting of the ruptured vessel

The spatial extent of the bleeding after a microhemorrhage could be limited by at least two different mechanisms. First, because RBCs are too large to move through the parenchyma they must compress the tissue around the ruptured vessel to enter the brain. The size of the microhemorrhage could be limited by a balance between the

pressure in the ruptured vessel and the contact stress of the RBC core with the parenchymal tissue. However, we found the contact stress between the RBC core and surrounding tissue to be 1.5 kPa, or about 11 mmHg, well below the typical pressure of a cortical PA, suggesting that tissue compression is not the limiting factor. Alternatively, formation of a clot at the vascular rupture site could limit the microhemorrhage size. We found that intravascular infusion of heparin during microhemorrhage as well as additional laser irradiation of the target vessel after initial vessel rupture both led to an increase in RBC core size (Fig. 5.1), suggesting that bleeding is limited by vessel clotting. Anticoagulant therapies, such as warfarin, are known to increase the size of ICH in patients[17], and our data suggests these drugs will also increase the size of microhemorrhages.

Tissue compression due to the RBC core does not result in acute ischemia

Previous studies of acute blood flow changes after ICH have found decreased CBF in the tissue around the hematoma, but it remains unclear whether this decreased CBF leads to ischemic infarction[18] or not[5, 19, 20]. For the microhemorrhages studied here, it is unlikely that there is ischemia surrounding the lesion. We found that nearly all brain capillaries within 75 μm of the microhemorrhage remained patent and flowing after the lesion. Further, the contact stress at the RBC core/tissue border was significantly less than the expected intraluminal pressure of cerebral vessels, suggesting that the tissue compression is not sufficient to crush nearby blood vessels. Measurements of the intraluminal pressure in cortical microvessels in mice are not available, but measurements in cat mesentery for similar sized vessels suggests pressures of 50 (25)

mmHg for arterioles (venules)[21], well below the pressure we found from tissue compression by a microhemorrhage. We did not, however, quantify flow rates through nearby capillary segments after microhemorrhage, so we cannot rule out small decreases in tissue perfusion.

Microglia/macrophage response after microhemorrhage is rapid and persists locally over days

Both brain-resident microglia as well as blood-borne monocytes are GFP positive in the CX_3CR1-GFP transgenic mouse[22]. The hemorrhage could potentially push monocytes directly into the brain during bleeding, and later invasion of monocytes in response to the microhemorrhage is likely. Thus, we are unable to distinguish between microglia and blood-derived macrophages in our analysis.

We showed an increase in the number of responsive microglia/macrophages within 200 μm of a microhemorrhage at 1.5 hours after the lesion. Other investigators have observed similar microglial responses in cells very close to an injury to the parenchymal tissue produced by irradiation with a train of high repetition rate, low-energy femtosecond laser pulses[23, 24]. For the parenchymal lesions we produced using irradiation with a small number of higher-energy laser pulses, we found that microglia responded only within about 60 μm of the ablation site, showing that the response of microglia/macrophages after a laser-induced microhemorrhage is dependent on bleeding into the brain parenchyma, not just the laser ablation. The 400-μm diameter region over which microglia/macrophages respond correlates with the spatial extent of the extravasated blood plasma, suggesting that blood plasma components may trigger

the microglia/macrophage activity. The mechanical compression of tissue by the extravasated RBCs may also play a role in initiating the microglia/macrophage response.

We further observed that microglia/macrophage processes invaded the RBC core within 1.5 hours after microhemorrhage. Past work has shown that gradients in extracellular ATP[23] or chemokines released from neurons[25] cause microglia to extend processes toward focal injuries within minutes. In the case of a microhemorrhage, blood components such as fibrin, thrombin, RBC breakdown products, and blood plasma may induce cells to extend processes into the RBC core[26, 27].

We observed an increase in microglia/macrophage density within 100 μm of the microhemorrhage but no decrease in density farther from the lesion, suggesting that the increase in cell density is not due to microglial migration but rather to proliferation of brain-resident microglia or infiltration of blood-borne monocytes. Consistent with this, past work has shown proliferation of resident microglia two to three days following brain injury that leads to a three to six fold increase in the microglia population[28]. Previous work has also shown that blood-borne monocytes cross the blood-brain-barrier near the site of injury and differentiate into macrophages after brain injury[29-31]. Our observation of GFAP upregulation in astrocytes within 200 μm of the microhemorrhage further suggests increased brain inflammation as a result of the lesion.

Our experiments reveal similar microglia/macrophage response to a microhemorrhage for heterozygous and homozygous CX_3CR1-GFP mice. Past work has shown that mice lacking functional CX_3CR1 receptors exhibit a decrease in

microglia recruitment after focal ischemia that leads to reductions in infarct volume, blood-brain barrier damage, and inflammation[32]. Similarly, less dendrite loss following mechanical injury was observed in CX_3CR1-null animals[33]. In addition, a decrease in the number of amyloid plaques[34] as well as a decrease in neuronal loss[35] has been observed in CX_3CR1-null mouse models of Alzheimer's disease. In contrast, our work reveals that the CX_3CR1 receptor does not play a major role in microglia/macrophage recruitment and response after microhemorrhage and that other signaling mechanisms must be involved.

Despite multiple potential cell injury mechanisms, we observed no structural degeneration of dendrites

In vivo imaging or post-mortem assessment of dendrite morphology is a sensitive assay of cell damage that has been used to investigate the spatial scale and temporal dynamics of neuronal injury after focal ischemia[13, 36-38]. We found no evidence of dendrite degeneration up to seven days after microhemorrhage and observed a relaxation of dendrites displaced by extravasated RBCs back to the core region beginning at one day. No degeneration of layer II/III dendrites was observed for microhemorrhages placed either in the dendrite tuft or near the cell bodies (in layer V). Similar to previous studies[39], our results did not show dendrite blebbing following photothrombotic occlusion of a PA.

We have ruled out ischemia due to tissue compression as a mechanism of cellular damage after microhemorrhage (Fig. 5.2). However, several mechanisms of brain cell injury following large ICH have been identified that could still play a role

after microhemorrhage. Blood components that enter the brain during bleeding, such as thrombin and plasminogen, are potentially toxic to neurons and other cells[40]. Neuronal injury can also result from excitotoxicity caused by the sudden increase in extracellular glutamate originating from the blood[41]. RBC lysis products are observed as early as one day after hemorrhage and can cause cellular injury through oxidative stress[4, 42-44]. The lack of dendrite pathology we observed suggests that individual microhemorrhages are not sufficient to cause significant cellular damage through these processes. Our experiments, however, did not examine changes in neuronal function, which may be altered even though structure is maintained.

Conclusions

Taken together, our data show that microhemorrhages create a perihematomal region distinguished by a local but sustained inflammatory response, and by the absence of ischemia or dendrite degeneration. The inflammation is characterized by acute activation and chronic increase in microglia/macrophages, as well as activation of astrocytes. The spatial extent of this perihematomal region is coincident with the initial distance blood plasma pushes into the brain parenchyma, suggesting that acute exposure to blood plasma components may initiate the inflammatory process. This inflammation, in turn, may be a long-term driver of neural dysfunction or death that underlies the cognitive decline linked to the accumulation of microhemorrhages. For example, inflammation has been shown to affect dendrite spine turnover in animal models of ischemia[45] mild injuries[46, 47]. However, our work also shows that occlusion of individual microvessels leads to more severe neuropathology than bleeding from

these vessels. Thus the cost of small vessel bleeds appears to be smaller than the cost of such vessels becoming occluded, suggesting that patients with elevated cardiovascular risk factors, such as hypertension, would potentially benefit from therapeutic strategies that prevent small vessel occlusions, even if at the expense of small vessel bleeds.

REFERENCES

1. Cullen, K.M., Kocsi, Z. & Stone, J. Pericapillary haem-rich deposits: evidence for microhaemorrhages in aging human cerebral cortex. *J Cereb Blood Flow Metab* **25**, 1656-1667 (2005).

2. Farrall, A.J. & Wardlaw, J.M. Blood-brain barrier: ageing and microvascular disease--systematic review and meta-analysis. *Neurobiol Aging* **30**, 337-352 (2009).

3. Terai, K., Suzuki, M., Sasamata, M. & Miyata, K. Amount of bleeding and hematoma size in the collagenase-induced intracerebral hemorrhage rat model. *Neurochem Res* **28**, 779-785 (2003).

4. Xi, G., Keep, R.F. & Hoff, J.T. Mechanisms of brain injury after intracerebral haemorrhage. *Lancet Neurol* **5**, 53-63 (2006).

5. Yang, G.Y., Betz, A.L., Chenevert, T.L., Brunberg, J.A. & Hoff, J.T. Experimental intracerebral hemorrhage: relationship between brain edema, blood flow, and blood-brain barrier permeability in rats. *J Neurosurgery* **81**, 93-102 (1994).

6. Xi, G.*, et al*. Mechanisms of edema formation after intracerebral hemorrhage: effects of extravasated red blood cells on blood flow and blood-brain barrier integrity. *Stroke* **32**, 2932-2938 (2001).

7. Xue, M. & Del Bigio, M.R. Intracerebral injection of autologous whole blood in rats: time course of inflammation and cell death. *Neurosci Lett* **283**, 230-232 (2000).

8. Nishimura, N.*, et al*. Targeted insult to subsurface cortical blood vessels using ultrashort laser pulses: three models of stroke. *Nature Methods* **3**, 99-108 (2006).

9. MacLellan, C.L., Silasi, G., Auriat, A.M. & Colbourne, F. Rodent models of intracerebral hemorrhage. *Stroke* **41**, S95-98 (2010).

10. Cullen, K.M., Kocsi, Z. & Stone, J. Microvascular pathology in the aging human brain: Evidence that senile plaques are sites of microhaemorrhages. *Neurobiol Aging* **27**, 1786-1796 (2006).

11. Schaffer, C.B.*, et al*. Two-photon imaging of cortical surface microvessels reveals a robust redistribution in blood flow after vascular occlusion. *PLoS Biol* **4**, e22 (2006).

12. Basser, P.J. Interstitial pressure, volume, and flow during infusion into brain tissue. *Microvasc Res* **44**, 143-165 (1992).

13. Zhang, S., Boyd, J., Delaney, K. & Murphy, T.H. Rapid reversible changes in dendritic spine structure in vivo gated by the degree of ischemia. *J Neurosci* **25**, 5333-5338 (2005).

14. Nishimura, N., Schaffer, C.B., Friedman, B., Lyden, P.D. & Kleinfeld, D. Penetrating arterioles are a bottleneck in the perfusion of neocortex. *Proc Natl Acad Sci U S A* **104**, 365-370 (2007).

15. Werring, D.J., *et al*. Cognitive dysfunction in patients with cerebral microbleeds on T2*-weighted gradient-echo MRI. *Brain* **127**, 2265-2275 (2004).

16. Wardlaw, J.M., Sandercock, P.A.G., Dennis, M.S. & Starr, J. Is breakdown of the blood-brain barrier responsible for lacunar stroke, leukoaraiosis, and dementia? *Stroke* **34**, 806-811 (2003).

17. Flaherty, M.L., *et al*. Warfarin use leads to larger intracerebral hematomas. *Neurology* **71**, 1084-1089 (2008).

18. Mendelow, A.D., Bullock, R., Teasdale, G.M., Graham, D.I. & McCulloch, J. Intracranial haemorrhage induced at arterial pressure in the rat. Part 2: Short term changes in local cerebral blood flow measured by autoradiography. *Neurol Res* **6**, 189-193 (1984).

19. Qureshi, A.I., Wilson, D.A., Hanley, D.F. & Traystman, R.J. No evidence for an ischemic penumbra in massive experimental intracerebral hemorrhage. *Neurology* **52**, 266-272 (1999).

20. Zazulia, A.R., *et al*. Hypoperfusion without ischemia surrounding acute intracerebral hemorrhage. *J Cereb Blood Flow & Metabolism* **21**, 804-810 (2001).

21. Lipowsky, H.H. Microvascular rheology and hemodynamics. *Microcirculation* **12**, 5-15 (2005).

22. Jung, S., *et al*. Analysis of fractalkine receptor CX(3)CR1 function by targeted deletion and green fluorescent protein reporter gene insertion. *Molecular and Cellular Biology* **20**, 4106-4114 (2000).

23. Davalos, D., *et al*. ATP mediates rapid microglial response to local brain injury in vivo. *Nat Neurosci* **8**, 752-758 (2005).

24. Kim, J.V. & Dustin, M.L. Innate response to focal necrotic injury inside the blood-brain barrier. *J Immunol* **177**, 5269-5277 (2006).

25. Biber, K., Vinet, J. & Boddeke, H.W.G.M. Neuron-microglia signaling: Chemokines as versatile messengers. *J Neuroimmunol* **198**, 69-74 (2008).

26. Moller, T., Hanisch, U.K. & Ransom, B.R. Thrombin-induced activation of cultured rodent microglia. *Journal of Neurochemistry* **75**, 1539-1547 (2000).

27. Hanisch, U.K. & Kettenmann, H. Microglia: active sensor and versatile effector cells in the normal and pathologic brain. *Nature neuroscience* **10**, 1387-1394 (2007).

28. Ladeby, R., *et al*. Microglial cell population dynamics in the injured adult central nervous system. *Brain research reviews* **48**, 196-206 (2005).

29. Simard, A.R., Soulet, D., Gowing, G., Julien, J.-P. & Rivest, S. Bone marrow-derived microglia play a critical role in restricting senile plaque formation in Alzheimer's disease. *Neuron* **49**, 489-502 (2006).

30. Tanaka, R., *et al*. Migration of enhanced green fluorescent protein expressing bone marrow-derived microglia/macrophage into the mouse brain following permanent focal ischemia. *Neuroscience* **117**, 531-539 (2003).

31. Malm, T.M., *et al*. Bone-marrow-derived cells contribute to the recruitment of microglial cells in response to beta-amyloid deposition in APP/PS1 double transgenic Alzheimer mice. *Neurobiol Dis* **18**, 134-142 (2005).

32. Dénes, A., Ferenczi, S., Halász, J., Környei, Z. & Kovács, K.J. Role of CX3CR1 (fractalkine receptor) in brain damage and inflammation induced by focal cerebral ischemia in mouse. *J Cereb Blood Flow Metab* **28**, 1707-1721 (2008).

33. Rappert, A., *et al*. CXCR3-dependent microglial recruitment is essential for dendrite loss after brain lesion. *Journal of Neuroscience* **24**, 8500-8509 (2004).

34. Lee, S., *et al*. CX3CR1 deficiency alters microglial activation and reduces beta-amyloid deposition in two Alzheimer's disease mouse models. *Am J Pathol* **177**, 2549-2562 (2010).

35. Fuhrmann, M., *et al*. Microglial Cx3cr1 knockout prevents neuron loss in a mouse model of Alzheimer's disease. *Nature neuroscience* **13**, 411-413 (2010).

36. Nishino, H., *et al*. Neuronal damage following transient cerebral ischemia and its restoration by neural transplant. *Neurobiology (Bp)* **2**, 223-234 (1994).

37. Petito, C.K. & Pulsinelli, W.A. Sequential development of reversible and irreversible neuronal damage following cerebral ischemia. *J Neuropathol Exp Neurol* **43**, 141-153 (1984).

38. Mostany, R. & Portera-Cailliau, C. Absence of large-scale dendritic plasticity

of layer 5 pyramidal neurons in peri-infarct cortex. *J Neurosci* **31**, 1734-1738 (2011).

39. Enright, L.E., Zhang, S.X. & Murphy, T.H. Fine mapping of the spatial relationship between acute ischemia and dendritic structure indicates selective vulnerability of layer V neuron dendritic tufts within single neurons in vivo. *J Cerebr Blood F Met* **27**, 1185-1200 (2007).

40. Fujimoto, S., *et al*. Plasminogen potentiates thrombin cytotoxicity and contributes to pathology of intracerebral hemorrhage in rats. *J Cerebr Blood F Met* **28**, 506-515 (2008).

41. Beal, M.F. Does impairment of energy metabolism result in excitotoxic neuronal death in neurodegenerative illnesses? *Ann Neurol* **31**, 119-130 (1992).

42. Gong, C., *et al*. Intracerebral hemorrhage-induced neuronal death. *Neurosurgery* **48**, 875-882 (2001).

43. Wu, J.M., *et al*. Oxidative brain injury from extravasated erythrocytes after intracerebral hemorrhage. *Brain Research* **953**, 45-52 (2002).

44. Xi, G.H., Keep, R.F. & Hoff, J.T. Erythrocytes and delayed brain edema formation following intracerebral hemorrhage in rats. *Journal of neurosurgery* **89**, 991-996 (1998).

45. Wake, H., Moorhouse, A.J., Jinno, S., Kohsaka, S. & Nabekura, J. Resting microglia directly monitor the functional state of synapses in vivo and determine the fate of ischemic terminals. *J Neurosci* **29**, 3974-3980 (2009).

46. Yang, G., Pan, F., Parkhurst, C.N., Grutzendler, J. & Gan, W.B. Thinned-skull cranial window technique for long-term imaging of the cortex in live mice. *Nat Protoc* **5**, 201-208 (2010).

47. Holtmaat, A., *et al*. Long-term, high-resolution imaging in the mouse neocortex through a chronic cranial window. *Nature Protocols* **4**, 1128-1144 (2009).

48. Feng, G., *et al*. Imaging neuronal subsets in transgenic mice expressing multiple spectral variants of GFP. *Neuron* **28**, 41-51 (2000).

49. Bignami, A., Eng, L.F., Dahl, D. & Uyeda, C.T. Localization of Glial Fibrillary Acidic Protein in Astrocytes by Immunofluorescence. *Brain Research* **43**, 429-& (1972).

CHAPTER SIX

LONG-TERM IMAGING OF CORTICAL DENDRITES REVEALS INCREASED GROWTH AND RETRACTION OF SPINES AFTER A MICROHEMORRHAGE

Nathanael L Rosidi[1], Weiyang Jin[1], Adam Bisogni[2], Sanket Pattanaik[1], Chris B. Shaffer[2]

[1]Department of Biomedical Engineering, Cornell University, Ithaca, NY

[1]Department of Biological and Biomedical Sciences, Cornell University, Ithaca, NY

ABSTRACT

Microbleeds, or ruptures to single blood vessels in the brain, have been correlated with the development of cognitive decline, dementia, and neurodegenerative disease. Recovery from these lesions is believed to be mediated primarily through the restructuring of surviving neuronal circuits. Dendrite spines are small membranous protrusions where single synapses are formed with axons, facilitating cellular communication. Changes in dendrite spine growth and retraction are thought to contribute to memory and learning in the mammalian brain. Under basal conditions, dendrite spines in adults are relatively stable and have a half-life of months, however, environmental changes and injuries to the brain can affect the stability of spines. Using two-photon excited fluorescence microscopy coupled with tightly-focused femtosecond laser pulses to rupture individual microvessels in mice, we explored the temporal and spatial impact of a microhemorrhage on spine plasticity. Our imaging of dendrite spines revealed an increased rate of spine loss and formation in the neural tissue within the vicinity of the microhemorrhage. Although previous work shows minimal dendrite structural degeneration after microhemorrhage, this work suggests an increase in dendrite rewiring after microhemorrhage, which could underlie the pathological alterations in neuronal function associated with these injuries in humans.

INTRODUCTION

Clinical evidence suggests that microhemorrhages may play a role in neurodegenerative diseases such as cognitive decline and Alzheimer's disease [1]. Recent work in rodents models induced with a microhemorrhage to a single penetrating arteriole (PA) has revealed that dendrites do not undergo structural degeneration (i.e., structural changes leading to circular swelling of dendrites) and relax back into the region in which they were displaced, over several days [2].

In larger intracerebral hemorrhage (ICH) models such as collagenase injection, neurons undergo apoptosis and necrosis in the vicinity of the hematoma over several days [3]. Microbleeds that affect small areas of the brain lead to iron and hemosiderin deposits in the area around the ruptured microvessel that can impact surrounding neurons [1]. Furthermore, dendrites have been observed to degenerate into blebs minutes after an occlusion to a single cortical blood vessel and can lead to cellular death in the brain days after the lesion if reperfusion of the occluded vessel does not occur [4]. In ischemia injury models, microglia-dendrite interactions are greatly reduced and can lead changes in synaptic activity [5].

In injuries where dendrite degeneration and cellular death are not observed, such as in open craniotomies where a portion of the skull is removed in rodents [6], the effects of an injury to the brain can affect the stability of the spine, leading to altered neuronal functions and rewiring of synapses. Dendrite spine dynamics is a subtle assay to assess the affects of an injury that does not result in complete structural degeneration of dendrites. Imaging preparations have been observed to affect dendrite spine dynamics. Craniotomies in which a portion of skull is removed and replaced with a coverglass have shown a 22% net loss of spines while imaging preparations where the skull is thinned have resulted in no net loss of spines over 30 days [7]. Furthermore, extravasated blood components have been known to have deleterious

effects on the brain. One potential mechanism known to affect the brain is the lysis of extravasated red blood cells (RBCs). Bi-products such as heme and iron cause oxidative stress and free radical damage to surrounding tissue that can result in brain injury [8]. Another mechanism that may affect the rate at which spines are gained or loss is the inflammatory response observed after lesioning. Injury to the brain leads to an invasion of microglia, macrophages, and neutrophils to the hemorrhage site and persists for weeks [2, 9]. This inflammatory response invoked by brain injury, while not affecting dendrite structure, can result in dendrite spine modulation and result in elimination of spines[7]. Although, dendrite structure remains intact, neuron function may be altered due to the blood components and inflammatory response resulting from the microhemorrhage.

In this chapter, we present preliminary work on the effect of dendrite spines after a microhemorrhage of a single PA. We used tightly focused femtosecond laser pulses to rupture single blood vessels in the cortex of the brain [10] and two-photon excited fluorescence (2PEF) imaging to track individual dendrite spines minutes to days after a microhemorrhage. We track the generation and deletion of dendrite spines over 14 days as a function of distance from the microhemorrhage. The rupture of a single PA led to extravasation of blood components into the brain resulting in a red blood cell (RBC) core 100 μm in diameter and blood plasma 500 μm in diameter [2]. These lesions are 10,000 times smaller than other intracerebral hemorrhage (ICH) models but match what has been histologically observed in human brains [1]. These data suggest that although structure is preserved, the function of neurons may be altered due to deleterious mechanisms resulting from the microhemorrhage.

METHODS

Transgenic animals

We used 2 adult C57BL/6 mice (~5 to 8 months of age, both sexes, 21-32 g in mass) expressing green fluorescent protein (GFP) in a subset of cortical neurons (Thy1-EGFP line; stock# 7788; The Jackson Laboratory)[11].

Chronic cranial imaging window preparation

A chronic cranial window was prepared using identical procedures as described in Rosidi et. al. [2]. Briefly, a 5-mm diameter circuluar bilateral craniotomy was performed over the parietal cortex on an anesthetized mouse. An 8-mm cover slip was attached and the animal was allowed to recover for a minimum of five days before in vivo imaging and laser induced microhemorrhaging. All animal procedures were approved by the Cornell University Institutional Animal Care and Use Committee.

Two-photon excited fluorescence microscopy

Before imaging sessions, mice were anesthetized with isoflurane (1.5-2%) and retro-orbitally injected with 0.1-mL of 2.5% (wt/vol) neutral (D1830; Invitrogen) or lysine-fixable (D1864; Invitrogen) Texas-Red dextran (70 kDa) in physiological saline to fluorescently label the blood plasma. Animals were transferred to a custom-built two-channel 2PEF microscope with 645/65 emission filters for Texas-Red and 517/65 filters for GFP. We used a 920-nm, 87-MHz, 100-fs pulse train from a Ti:sapphire laser oscillator (MIRA HP; Coherent), pumped by a continuous wave laser (Verdi-V18; Coherent), was used to image GFP and Texas-Red in the mice.

We identified penetrating arterioles (PAs), i.e., arterioles that branch from the surface arteriole network and dive into the brain to feed capillary beds, as target vessels [12]. To rupture the target PA, we used an identical technique adapted from

Rosidi et al [2]. Briefly, to induce a microhemorrhage, femtosecond laser pulses were tightly focused on the outer edge of the lumen vessel. We used an energy of about 500 nJ/pulse to rupture the target PA. If the vessel did not rupture, the last energy was increased by about 50% and the vessel was irradiated again until extravasation of RBCs and blood plasma into the parenchyma was observed.

Quantification of dendrite spines before and after microhemorrhage

2PEF image stacks spaced 1-μm apart in the axial direction were taken of dendrites and blood vasculature in layer I/II of the cortex. Time lapse stacks were collected before, after, one day, two days, seven days, and fourteen days after microhemorrhage. In each stack, we scored clear instances of dendrite spine appearance or disappearance as well as the presence of any spines counted from previous 2PEF image sessions. All changes in spine structure were determined relative to the previous time lapse image stacks. Due to varations in 2PEF image quality after the rupture of a blood vessel over time, changes to dendrite spines that occurred only within one 24-hr period were not analyzed (e.g., a dendrite spine present immediately after a microhemorrhage, then absent one day after the microhemorrhage, but present in the same location two days after a microhemorrhage was counted as present throughout all three imaging sessions). The axial resolution of the microscope was poor, so we only counted spines protruding normal to the optical axis. Only spines that were easily distinguishable from the background signal were counted. Turnover rates were calculated as $(N_{gained} + N_{lost})/(N_{total})$ where N_{gained} is the number of new spines, N_{lost} is the number of spines that disappeared, and N_{total} is the total number of spines.

RESULTS

We used 2PEF imaging to visualize dendrite spine dynamics immediately and up to 14 days following a microhemorrhage of single PAs in the cortex of mice. Using tightly focused femtosecond laser pulses, we produced microhemorrhages leading to extravasation of RBCs and blood plasma out to 100 μm and 500 μm in diameter, respectively [2]. We tracked the gain and loss of dendrite spines within 700 μm from the center of the microhemorrhage and on the contralateral side up to 14 days after the microhemorrhage (Fig. 6.1).

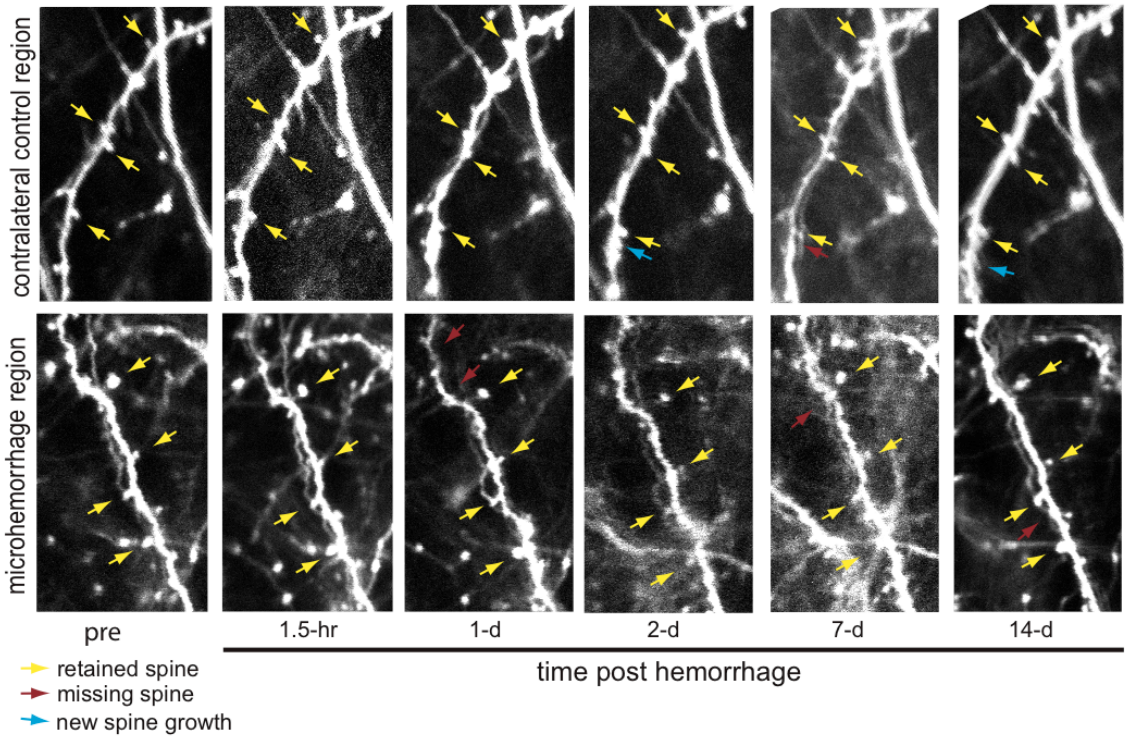

Figure 6.1 Time-lapse 2PEF images of dendrite spines. 2PEF images of fluorescently labeled dendrite spines, 20-100 µm beneath the cortical surface, before and up to 14 days after microhemorrhage. Control region is on the contralateral side of the microhemorrhage, where no microhemorrhage induced.

Increased dendrite spine turnover rate after microhemorrhage

Immediately after microhemorrhage, we tracked individual dendrite spines out to 14 days and found an increase in the fractional spine change, defined as the number of

spines gained and lost over the total number of spines, in the microhemorrhage region (Fig. 6.2a). Dendrite spines on the contralateral control side, where no injury was induced, exhibited a lower fractional spine change compared to the microhemorrhage region at all time points over 14 days. Although, the fractional spine change between the microhemorrhage region and contralateral control side was statistically non-significant, the difference in spine changes between the microhemorrhage and contralateral region is apparent. We compared the cumulative number of dendrite spines gained and lost in the microhemorrhage region up to 14 days and found that the number of spines gained per dendrite was higher at every time point compared to spines on the contralateral control region (Fig. 6.2b; $p < 0.04$; analysis of covariance). Furthermore, the number of spines lost in the microhemorrhage region was higher than the contralateral control region ($p < 0.004$; analysis of covariance).

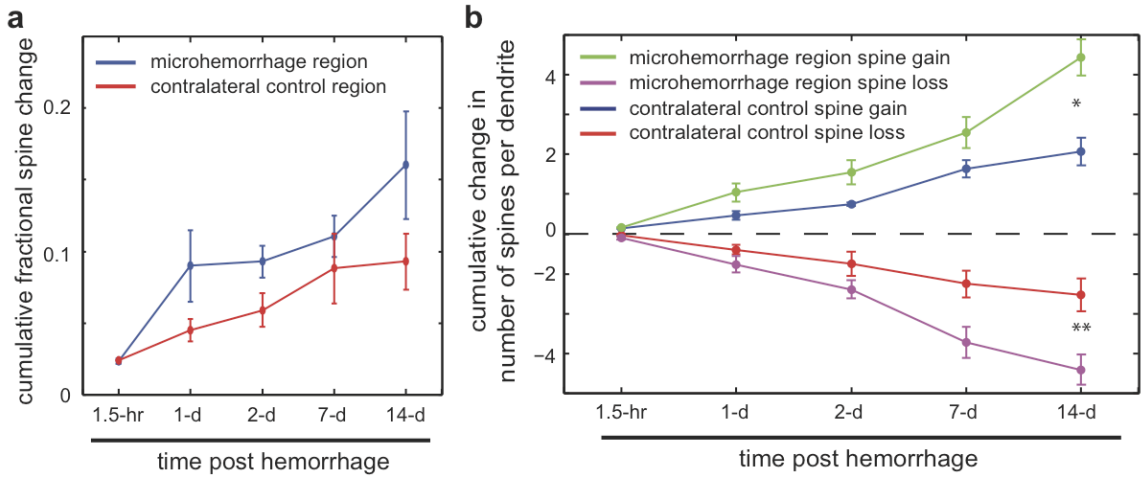

Figure 6.2 Dendrite spine change is increased in microhemorrhage region. (a) Cumulative spine change (i.e., total number of spine gain and loss) over the total number of spines counted out to 14 days after microhemorrhage. The fractional spine change within the microhemorrhage region (contralateral control region) is represented with a blue (red) line. **(b)** Cumulative change in the number of spine gained and lost per dendrite in the microhemorrhage and contralateral control region out to 14 days after microhemorrhage. Dendrite spine gain (loss) in the microhemorrhage region is represented by the green (purple) line. Dendrite spine gain (loss) in the contralateral control region is represented by the blue (red) line.

The microhemorrhage region led to an increase in dendrite spine loss and gain compared to the contralateral control region where no injury was induced, so we next looked at the number of stable spines that were retained in all imaging sessions up to 14 days. We found that the number of stable spines in the microhemorrhage region was significantly lower than the number of stable spines in the contralateral control side (~83% stable spines in the microhemorrhage region vs ~91% stable spines in the contralateral control region; $p < 0.05$; student t-test).

Dendrite spine turnover rate as a function of distance from the microhemorrhage

We next assessed the spatial scale of the dendrite spine change after microhemorrhage. We analyzed the spatial scale of dendrite spine change by counting the number of spine gain and loss as a function of distance from the center of the microhemorrhage. Dendrite spine change remained constant up to 700 μm from the center of the microhemorrhage (Fig. 6.3).

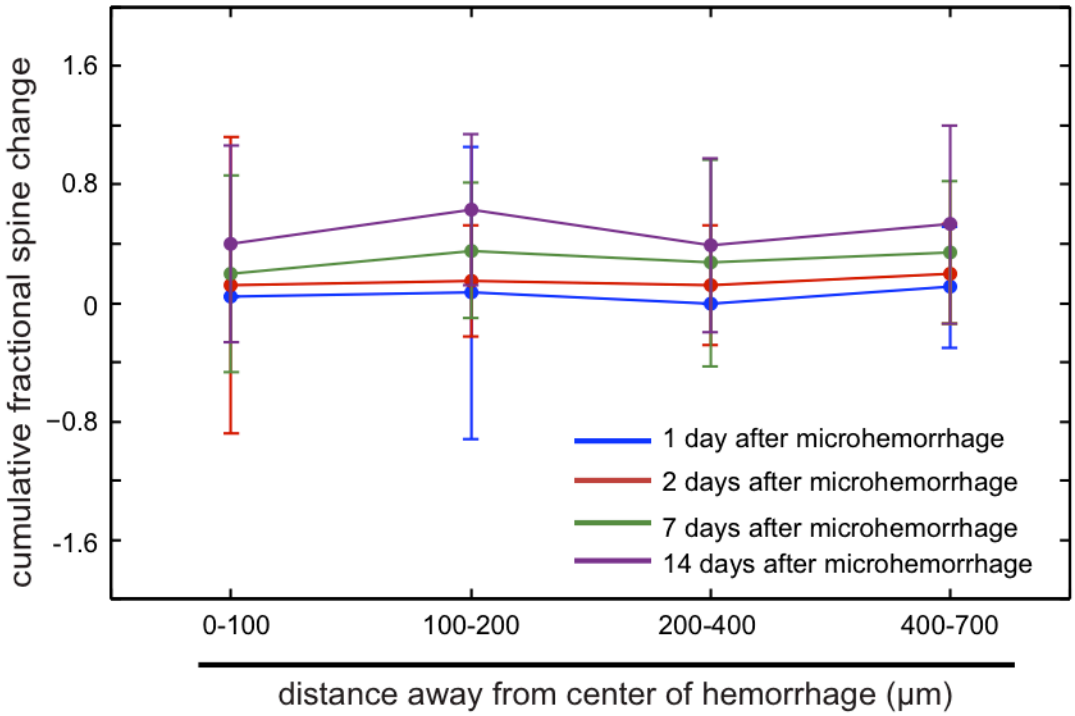

Figure 6.3 Spine change as a function of distance from the center of the microhemorrhage. Cumulative spine change (i.e., total number of spine gain and loss) over the total number of spines counted as a function of the distance from the center of the microhemorrhage. Fractional spine change as a function of distance from the microhemorrhage 1 day, 2 days, 7 days, and 14 days after microhemorrhage is represented by blue, red, green, purple lines, respectively.

DISCUSSION

In vivo dendrite structure analysis is a sensitive assay for cellular damage and has been used to assess the spatial and temporal scale of neuronal health after an injury [2, 13]. In animal models where severe ischemia is present, dendrite structure is observed to degenerate into blebs within 10 minutes of vessel occlusion [4]. Our microhemorrhages do not lead to a blockage in blood flow but does lead to extravasation of RBCs and blood plasma. We show that our lesions do not lead to dendrite degeneration at any time point up to 14 days after microhemorrhage and is consistent with previous work of similar injury [2].

Dendrite spine stability and choice of imaging preparation

There are several mechanisms present that may affect dendrite spines after brain injury. The choice of cranial window for in vivo imaging affects dendrite spines in the cortex, as these preparations cause mild trauma. ~95% of total spines remain stable over two weeks in preparations where the skull of the rodent is thinned to allow transmission of light for imaging, while ~60% of spines remain stable in open craniotomy preparations where a portion of skull is removed and replaced with a coverglass [7, 14]. In our work we replaced a portion of the skull with a coverglass for imaging. We counted the number of dendrite spines that persist through all imaging sessions and found that ~85% of spines, in the vicinity of the microhemorrhage, were stable out to 14 days after microhemorrhage. In contrast, ~91% of spines were found to persist throughout all imaging sessions out to 14 days after microhemorrhage in the contralateral control region where no microhemorrhage was induced. We counted a higher population of stable spines in our open craniotomy preparation compared to other investigators using the same cranial preparation [14], suggesting either a bias in dendrite spine counting or a cleaner open craniotomy preparation that causes less brain

trauma. 2PEF image quality varied throughout imaging sessions due to extravasation of RBCs and blood plasma as well as inflammation after microhemorrhage, which may have biased spine counting towards more robust, larger spines that are easier to distinguish in vivo [15]. These larger spines are typically more stable than smaller spines and have a greater probability of persisting for weeks after a microhemorrhage. However, we counted every dendrite spine in identical image volumes across all imaging sessions and do observe a difference in dendrite spine growth and retraction rates between the contralateral and injury side. This difference in spine growth and retraction rates indicate that our imaging preparations may cause less brain injury than the preparations of other investigators.

Increased dendrite spine change after microhemorrhage

We assessed the spatial and temporal dynamics of dendrite spines and show that although no dendrite degeneration was observed, the number of dendrite spines gained and lost were increased over 14 days. We compared the dendrite spine change, defined as the number of spines gained and loss as a fraction of the total population of spines counted, between the contralateral control region and the microhemorrhage region to analyze the cellular impact due to a microhemorrhage. We found that the spine change in the vicinity of the microhemorrhage was greater than on the contralateral control region where no microhemorrhage was induced. However, we found no spatial trend in dendrite spine change out to 700 μm from the center of the microhemorrhage. Spine change appeared to be constant throughout the microhemorrhage region.

Dendrite spines changes have been found to increase after sensory deperivation and/or injury. Investigators have used dendrite spine dynamics as assays in neuronal rewiring and plasticity. Sensory deprivation have resulted in an increase in transient spines, defined as spines present for only a single day, over four days of imaging while

the pool of stable spines decreased over the same time frame [14]. Visual sensory deprivation in month old mice resulted in a 60% increase in spine turnover rates, elongation and retraction of spines, changes in the position and shape of the spine head, and the appearance of filopodia (ie, unstable dendrite spines) by compared to controls [16]. Furthermore, increased changes in dendrite structure and network have been observed after transient middle cerebral artery occlusion (MCAo). Analyzing dendrite structure of layer V pyramidal neurons over 30 days after MCAo, dendrite length is observed to decrease which is then followed by pruning of dendrite branches [17]. Finally, neural network models have shown interactions between neighboring dendrite spine synapses by depolarizing a single dendrite spine and measuring the potential to depolarize nearby spines. The nearby spines are measured to have a lower potential, therefore any change in spines such as an increase or decrease in spine numbers may lead to a changes in the neuronal network [18]. We see ~85% of spines through all imaging sessions on the injury side and 91% of spines on the contralateral control side, indicting less rewiring than previously observed in similar imaging preparations [14].

Extravasated blood and inflammation effects lead to deleterious effects on the microenvironment after microhemorhage

Brain injury is known to result in an acute and persistent inflammatory response by microglia, macrophages, and astrocytes. These inflammatory cells respond to changes in parenchymal tissue that come from the lesion. For example, after a microhemorrhage, RBCs extravasate into the parenchyma and cause secondary damage due to lysed RBC, which can cause DNA and cellular damage to surrounding tissue as early as 24-hr after ICH. [19, 20]. Hemoglobin break down products, oxidative stress, inflammation through RBC lysis can affect the neuronal health near the

microhemorrhage [21]. Moreover, blood entering the parenchyma carries components toxic to neurons and other cells including thrombin and plasminogen. These blood components have been shown to potentiate neuronal injury when injected into the brain parenchyma [22]. Other brain injuries such as open craniotomies can lead to an inflammatory response. Within two days after craniotomy, microglia/macrophages in layer I/II of the brain assume an activated amoeboid shape form or displayed processes towards the pial surface [23]. Ischemia from occlusions in the brain show reduced microglia activity in contrast to other brain injuries. Microglia are known to survey their surroundings and establish transient connections with dendrite spines. Under ischemia, microglia show a prolonged connection with dendrite spines. This prolonged contact is on average 15 times longer than during states of no ischemia and can lead to synaptic loss and reduced overall synaptic activity [5]. These brain injury models lead to several mechanisms of damage and results in an inflammatory response.

In addition to brain injury, bi-products produced by inflammatory cells result in deleterious effects on the brain. Reactive oxygen species (ROS) and cytokines produced by activated microglia can damage neurons [24]. Activated microglia, defined as a morphological change and response to a brain injury, can effect glutamate transmission resulting in synaptic defects of neurons. Cytokines released by microglia has been shown to affect astrocyte activity by inhibiting the astocyte gap junction needed for communication [25]. Microglia also contribute to neuron loss in chronic disease states such as Alzhemier's disease. Neurons in the vicinity of Aβ-plaques have been shown to disappear during microglia invasion and response [26].

Conclusion

We do not observe any dendrite degeneration after microhemorrhage, consistent with past investigations, and looked for subtle changes in spine dynamics after an injury.

We have shown that dendrite spines are less stable in the vicinity of a microhemorrhage out to 14 days after lesioning. This change in dendrite spine stability can have altered effects on neuronal function. These changes in the brain can lead to cognitive decline, neurodegenerative diseases and post-traumatic epilepsy.

REFERENCES

1. Cullen, K.M., Kocsi, Z. & Stone, J. Pericapillary haem-rich deposits: evidence for microhaemorrhages in aging human cerebral cortex. *J Cereb Blood Flow Metab* **25**, 1656-1667 (2005).

2. Rosidi, N.L., *et al*. Cortical microhemorrhages cause local inflammation but do not trigger dendrite pathology. *submitted* (2011).

3. Felberg, R.A., *et al*. Cell death in experimental intracerebral hemorrhage: the "black hole" model of hemorrhagic damage. *Ann Neurol* **51**, 517-524 (2002).

4. Zhang, S., Boyd, J., Delaney, K. & Murphy, T.H. Rapid reversible changes in dendritic spine structure in vivo gated by the degree of ischemia. *J Neurosci* **25**, 5333-5338 (2005).

5. Wake, H., Moorhouse, A.J., Jinno, S., Kohsaka, S. & Nabekura, J. Resting microglia directly monitor the functional state of synapses in vivo and determine the fate of ischemic terminals. *J Neurosci* **29**, 3974-3980 (2009).

6. Shepherd, G., Zhang, X., Knott, G. & Svoboda, K. Transient and persistent dendritic spines in the neocortex in vivo. *Neuron* (2005).

7. Xu, H.T., Pan, F., Yang, G. & Gan, W.B. Choice of cranial window type for in vivo imaging affects dendritic spine turnover in the cortex. *Nature neuroscience* **10**, 549-551 (2007).

8. Xi, G., *et al*. Intracerebral hemorrhage: pathophysiology and therapy. *Neurocrit Care* **1**, 5-18 (2004).

9. Xue, M. & Del Bigio, M.R. Intracerebral injection of autologous whole blood in rats: time course of inflammation and cell death. *Neurosci Lett* **283**, 230-232 (2000).

10. Nishimura, N., *et al*. Targeted insult to subsurface cortical blood vessels using ultrashort laser pulses: three models of stroke. *Nature Methods* **3**, 99-108 (2006).

11. Feng, G., *et al*. Imaging neuronal subsets in transgenic mice expressing multiple spectral variants of GFP. *Neuron* **28**, 41-51 (2000).

12. Nishimura, N., Schaffer, C.B., Friedman, B., Lyden, P.D. & Kleinfeld, D. Penetrating arterioles are a bottleneck in the perfusion of neocortex. *Proc Natl Acad Sci U S A* **104**, 365-370 (2007).

13. Enright, L.E., Zhang, S.X. & Murphy, T.H. Fine mapping of the spatial relationship between acute ischemia and dendritic structure indicates selective vulnerability of layer V neuron dendritic tufts within single neurons in vivo. *J Cerebr Blood F Met* **27**, 1185-1200 (2007).

14. Trachtenberg, J., Chen, B., Knott, G. & Feng, G. Long-term in vivo imaging of experience-dependent synaptic plasticity in adult cortex. *Nature* (2002).

15. Kasai, H., Matsuzaki, M., Noguchi, J., Yasumatsu, N. & Nakahara, H. Structure-stability-function relationships of dendritic spines. *Trends Neurosci* **26**, 360-368 (2003).

16. Majewska, A. & Sur, M. Motility of dendritic spines in visual cortex in vivo: changes during the critical period and effects of visual deprivation. … *of the National Academy of Sciences* … (2003).

17. Mostany, R. & Portera-Cailliau, C. Absence of large-scale dendritic plasticity of layer 5 pyramidal neurons in peri-infarct cortex. *J Neurosci* **31**, 1734-1738 (2011).
18. Harvey, C. & Svoboda, K. Locally dynamic synaptic learning rules in pyramidal neuron dendrites. *Nature* (2007).

19. Gong, C., *et al*. Intracerebral hemorrhage-induced neuronal death. *Neurosurgery* **48**, 875-882 (2001).

20. Xi, G., Keep, R.F. & Hoff, J.T. Mechanisms of brain injury after intracerebral haemorrhage. *Lancet Neurol* **5**, 53-63 (2006).

21. Wu, J.M., *et al*. Oxidative brain injury from extravasated erythrocytes after intracerebral hemorrhage. *Brain Research* **953**, 45-52 (2002).

22. Fujimoto, S., *et al*. Plasminogen potentiates thrombin cytotoxicity and contributes to pathology of intracerebral hemorrhage in rats. *J Cerebr Blood F Met* **28**, 506-515 (2008).

23. Holtmaat, A., *et al*. Long-term, high-resolution imaging in the mouse neocortex through a chronic cranial window. *Nature Protocols* **4**, 1128-1144 (2009).

24. Vilhardt, F. Microglia: phagocyte and glia cell. *Int J Biochem Cell Biol* **37**, 17-21 (2005).

25. Walter, L. & Neumann, H. Role of microglia in neuronal degeneration and regeneration. *Semin Immunopathol* **31**, 513-525 (2009).

26. Fuhrmann, M., *et al*. Microglial Cx3cr1 knockout prevents neuron loss in a mouse model of Alzheimer's disease. *Nature neuroscience* **13**, 411-413 (2010).

CHAPTER SEVEN

TISSUE PLASMINOGEN ACTIVATOR THERAPY AFTER INTRACEREBRAL HEMORRHAGE DOES NOT LEAD TO AN INCREASE IN BLOOD VOLUME

This research is my work from a collaboration resulting in a manuscript submitted to a peer-reviewed journal.

Nathanael L. Rosidi[1], Flor A. Cianchetti[1], Chris B. Schaffer[1]

[1]Department of Biomedical Engineering, Cornell University, Ithaca, New York, USA

The original work was submitted to a peer-reviewed journal.

Christian Foerch[1,2], Nathanael L. Rosidi[3], Frieder Schlunk[1,2], Arne Lauer[1,2], Flor A. Cianchetti[3], Kazim Yigitkanli[1], Klaus van Leyen[1], Helmuth Steinmetz[2], Chris B. Schaffer[3], Eng H. Lo[1]

[1]Neuroprotection Research Laboratory, Massachusetts General Hospital, Harvard Medical School, Boston, Massachusetts, USA

[2]Department of Neurology, Johann Wolfgang Goethe-Universität, Frankfurt am Main, Germany

[3]Department of Biomedical Engineering, Cornell University, Ithaca, New York, USA

Intravenous tPA therapy does not increase hematoma volume in acute intracerebral haemorrhage.

ABSTRACT

Tissue plasminogen activator (tPA) is the only FDA-approved drug for the treatment of ischemic stroke. It is used to dissolve clots and re-establish blood flow in the brain. In current clinical practice, patients with intracerebral hemorrhages (ICH) are not administered tPA which can delay treatment times for patients displaying stroke like symptoms. However, no data exists on the effect of tPA therapy on acute ICH. To study the effects of an ICH under tPA treatment, we used two-photon excited fluorescence (2PEF) together with tightly focused femtosecond laser pulses to rupture individual cortical microvessels in mice and causing an ICH. We found no difference in both extravasated red blood cell (RBC) and blood plasma diameters between intravenous saline and tPA treatments after ICH. However, intravenous anticoagulant, heparin, treatment led to a 44% increase in hematoma size. Taken together, tPA treatment does not lead to an increase in hematoma size and does not support the assumption that tPA has a deleterious effect on acute ICH.

INTRODUCTION

A current therapeutic for ischemic stroke is the application of intravenous tissue plasminogen activator (tPA) [1]. Patients are administered tPA to dissolve clots in the brain and re-establish blood flow. The timing of tPA application is important when trying to save tissue in the ischemic zone of the stroke as occlusions can lead to neuronal degeneration as early as 10 minutes after blockage of blood flow. The sooner the patient is administered tPA treatment, the higher the probability for improved outcome [2]. Investigators have found that neuronal degeneration can be reversed if blood flow is restored within 20 to 60 minutes after occlusion, thereby establishing a therapeutic window [3]. However, there is currently a treatment delay for patients showing signs of stroke. Patients must first be scanned to rule out the possibility of a hemorrhage, as it is believed that tPA treatment may enlarge hematoma volume and negatively impact the health of the patient [4, 5]. However, the assumption that tPA may enlarge hematoma volume lacks scientific validation. We use two-photon excited fluorescence (2PEF) imaging coupled with a femtosecond laser to rupture penetrating arterioles (PAs) i.e., arterioles that plunge into the brain, leading to extravasation of red blood cells (RBCs) and plasma into the brain, to test the affects of tPA on hemorrhage size.

METHODS

All animal procedures were approved by Cornell University Institutional Animal Care and Use Committee. Eleven C57BL/6J (The Jackson Laboratory) mice (5 female, 6 male) ranging from 21 to 32g in mass were used to image the size of femtosecond laser induced microhemorrhages. To prepare a chronic cranial window for imaging, mice were anesthetized using 5% isoflurane (VetOne) and maintained at 1.5-2%. Body temperature was kept at a constant temperature of 37.5°C with a heating blanket and thermometer (50-7053P; Harvard Apparatus). Glycopyrrolate (0.005mg/kg mouse (Baxter Healthcare Corp.)) was administered intramuscularly while ketoprofen (5 mg/kg mouse (Ketofen)) and dexamethasone sodium phosphate (0.2mg/kg mouse (American Regent, Inc.)) were both administered subcutaneously prior to surgery. A 6-mm diameter bilateral craniotomy was performed over the parietal cortex. An 8-mm glass cover slip (Deckglaser; WPI) was then glued over the exposed brain using cyanoacrylate and dental cement (Lang Dental Mfg Co. & Co-Oral-Ite Dental Mfg Co.). Animals were administered 5% (wt/vol) glucose in physiological saline (0.1ml/100g mice) subcutaneously and gradually transitioned off isoflurane anesthesia. Mice were then administered ketoprofen (5 mg/kg) every 24 hrs for 72 hrs and allowed a minimum of five days recovery before jugular vein cannulation, in vivo imaging, and vessel hemorrhaging.

Under isoflurane anesthesia (1.5% to 2%) with spontaneous respiration in a nitrous oxide–oxygen mixture, the right jugular vein was prepared. After ligating the distal part of the vessel, a PE-10 tube was inserted into the jugular vein and moved forward in the proximal direction. After properly fixing the tube and closing the suture, the animals were placed in a stereotactic frame. Under ongoing anesthesia, a small borehole was drilled, and a 32-gauge 0.5-mL microinjection needle (Hamilton, 7000 series, Hamilton, Reno, NV, USA) was slowly lowered into the right striatum at

the following stereotactic coordinates from the bregma: 0.0mm anterior, 2.0mm lateral, and 3.5mm depth. Over a period of 5 mins, 0.5mL of saline containing 0.2U of collagenase VII-S (Sigma-Aldrich, St Louis, MO, USA) was injected. The needle was left in place for 10 mins, and then slowly removed over a period of 5 mins. Thereafter, the borehole was sealed with bone wax and the scalp closed. The mice were then allowed to wake up and were put in a mouse restrainer under light restraint. Beginning 30 min after microhemorrhage induction, saline (500μl, 9 microhemorrhages), recombinant human tPA (10mg/kg, diluted in 500μl saline, 11 microhemorrhages) or heparin (100U/kg, diluted in 500μl saline, 10 microhemorrhages) was continuously injected through the jugular vein catheter for 30 min using an injection pump (10% bolus injection over the first minute). The correct intravenous position of the catheter was double-checked by drawing some blood into the tube after the injection. The catheter was then ligated and cut near the skin and the mice were returned to their cages.

Two-photon excited fluorescence microscopy

Before imaging sessions, mice were anesthetized on isoflurane and the jugular vein was cannulated, as described above. Mice were intravenously injected with 0.1mL of 5% (wt/vol) lysine-fixable Texas-Red dextran (70 kDa) fluorescent dye (D1864; Invitrogen) in physiological saline to label the vasculature. In-vivo imaging was conducted with a custom-designed two-photon excited fluorescence (2PEF) microscope using a 1045-nm, 1-MHz, 350-fs pulse train from a Yb-fiber oscillator/amplifier system (μJewel FCPA, IMRA America, Inc.) as the excitation source. Fluorescence emission was collected with a 65-nm wide filter centered at 645 nm (Chroma). 2PEF imaging revealed surface blood vessels and sub-surface capillaries. In addition to visualizing vascular topology, we measured the diameter and blood flow speed and direction in individual vessels, as described previously by

Schaffer et al [6]. For microhemorrhages, we targeted penetrating arterioles (PA), i.e. arterioles that branch from the surface arteriole network and dive into the brain to feed capillary beds. These vessels were identified by tracing through the vascular network from readily-identifiable surface arterioles and we confirmed they were penetrating arterioles by checking that the blood flow direction was into the brain.

Penetrating arteriole microhemorrhage by femtosecond laser ablation

Each mouse was subjected to one to four microhemorrhages with a minimum of 1-mm spacing between ruptured vessels. 2PEF image stacks of each microhemorrhage site as well as diameter and blood flow speed measurements of the target PAs were collected before microhemorrhages were induced. A 50-μL bolus injection of saline (9 microhemorrhages across 4 animals), tPA (11 microhemorrhages across 4 animals), or heparin (10 microhemorrhages across 3 animals) was infused through the jugular vein catheter, then after five minutes a constant infusion rate (15 μL/min) was set using a syringe pump (PHD2000; Harvard Apparatus), as described above.

During the period of steady infusion, the targeted PAs were once again located and microhemorrhages were produced in the descending segment of the PA, about 50-100μm below the surface of the brain. To induce a microhemorrhage, 50-fs duration laser pulses were tightly focused (1.0 numerical aperture) on the wall of the targeted PA, as described by Nishimura, et al [7]. Briefly, a laser energy of about 700 nJ was initially applied for a 10 pulse burst (1-kHz repetition rate). If the vessel did not rupture, the laser energy was increased by about 50% and the vessel was irradiated again. This process was repeated until extravasation of RBCs and blood plasma into the parenchyma of the brain was observed. The variation of required laser energy to trigger a microhemorrhage depends mainly on the depth of the target vessel beneath the brain surface and the presence or absence of large blood vessels on the brain

surface above the target vessel. We use the minimum laser energy required to rupture the vessel wall of the targeted PA and initiate bleeding into the brain. 2PEF image stacks were taken immediately, 30 min, and 1.5-hr after each PA hemorrhage.

Red blood cell and plasma diameter measurements

During the microhemorrhage, RBCs and plasma exit the lumen of the targeted PA. Since the fluorescent marker only labels blood plasma, under 2PEF imaging the RBCs are visualized as dark patches in a sea of fluorescently-labeled blood plasma leaving the vessel. After the microhemorrhage, the region immediately surrounding the targeted PA is filled with RBCs. This region appears dark in the 2PEF image because the RBCs are densely packed and largely exclude the fluorescently labelled blood plasma. Blood plasma exiting the lumen of the target vessel moves further into the brain parenchyma than the RBCs and can be visualized by a ring of increased fluorescence surrounding the RBC filled hemorrhage core. RBC core and plasma extravasation diameters were calculated from a maximal projection of 20-μm of the 2PEF image stack (ImageJ) taken 1.5-hr after the microhemorrhage, with the stack centered on the depth where the microhemorrhage was created.

Post-mortem histology

At the end of each imaging session, animals were transcardially perfused with 20-ml of phosphate buffered saline (PBS) (Sigma-Aldrich) and 30-ml of 4% (wt/vol) paraformaldehyde (Fisher Scientific) in PBS. The brain was extracted from the skull and cryoprotected by immersion in 30% (wt/vol) sucrose in PBS for 24 hrs and then in 60% sucrose in PBS. Fiducial marks were made in the left corners of the craniotomy window by vertically inserting a 25-gauge needle 2 mm into the brain. The needle was externally tinted with black ink (Parker). The fiducial marks were placed in known locations relative to the microhemorrhage sites. The brain was then frozen and cut into

50-μm thick coronal sections on a cryostat. The sections were mounted onto microscope slides (Superfrost Plus, Fisher Sci.) and incubated for 12 min with diaminobenzadine (DAB) (Peroxidase Substrate kit, Vector labs, no. SK-4100) to stain endogenous peroxidase in RBCs and then rinsed with deionized water. The sections were photographed under brightfield and fluorescence microscopy. Fiducials were mapped and used to identify the slices and location within slices where microhemorrhages were located. Microhemorrhages were identified on the basis of both DAB stained RBCs and Texas Red-dextran fluorescence in the parenchymal space.

Statistical analysis

A p-value of less than 0.05 was considered statistically significant. Parametric statistical tests (student t-test, Pearson's correlation coefficient) were used on normal distributions, while non-parametric statistical tests (Mann-Whitney U test, Spearman's rank correlation coefficient) were used on non-normal population distributions using Matlab 7.6 (The Mathworks, Inc.) and JMP7 statistical software (SAS Institute Inc.). A goodness-of-fit test (JMP7 statistical software) was used to determine normal and non-normal populations.

Box plots were generated with Matlab 7.6 using the boxplot function, displaying the 25th percentile (first quartile), 50th percentile (median), 75th percentile (third quartile) values of the data set. Whiskers denote the minimum and maximum values that were not outliers. Data points were considered outliers if points fell below 1.5 time the interquartile range (IQR) from the first quartile or above 1.5 times the IQR from the third quartile. The IQR is defined as the difference between the third quartile and first quartile. Means were calculated without statistical outliers and indicated by a red x on the box plot.

RESULTS

We used 2PEF imaging and tightly focused femtosecond laser pulses to rupture a PA within the first 100 μm of the cortex in 11 mice, causing extravasation of RBCs and blood plasma into the parenchyma [8]. The region immediately surrounding the target PA filled with densely packed RBCs that largely excluded the fluorescently labelled blood plasma, thus appearing dark in the 2PEF image. The RBC core was surrounded by fluorescence, indicating extravasated blood plasma. During the production of microhemorrhages, animals received intravenous saline (9 microhemorrhages in 4 mice), tPA (11 microhemorrhages in 4 mice), or heparin (microhemorrhages in 3 mice) (Fig. 7.1).

The diameter of the RBC core expanded to 91 +/- 16 μm (mean +/- standard deviation) and 89 +/- 26 μm after 1.5-hr for microhemorrhages with intravenous tPA and saline, respectively. We found no difference in the size of the RBC-filled core between saline and tPA infused mice (Fig. 7.2). We found that intravenous heparin led to an increase in the final RBC core size by 44% to 134 +/- 21 μm 1.5-hr after microhemorrhage (Fig. 7.2; $p < 0.0025$; Mann Whitney U test).

We measured the diameter of extravasated

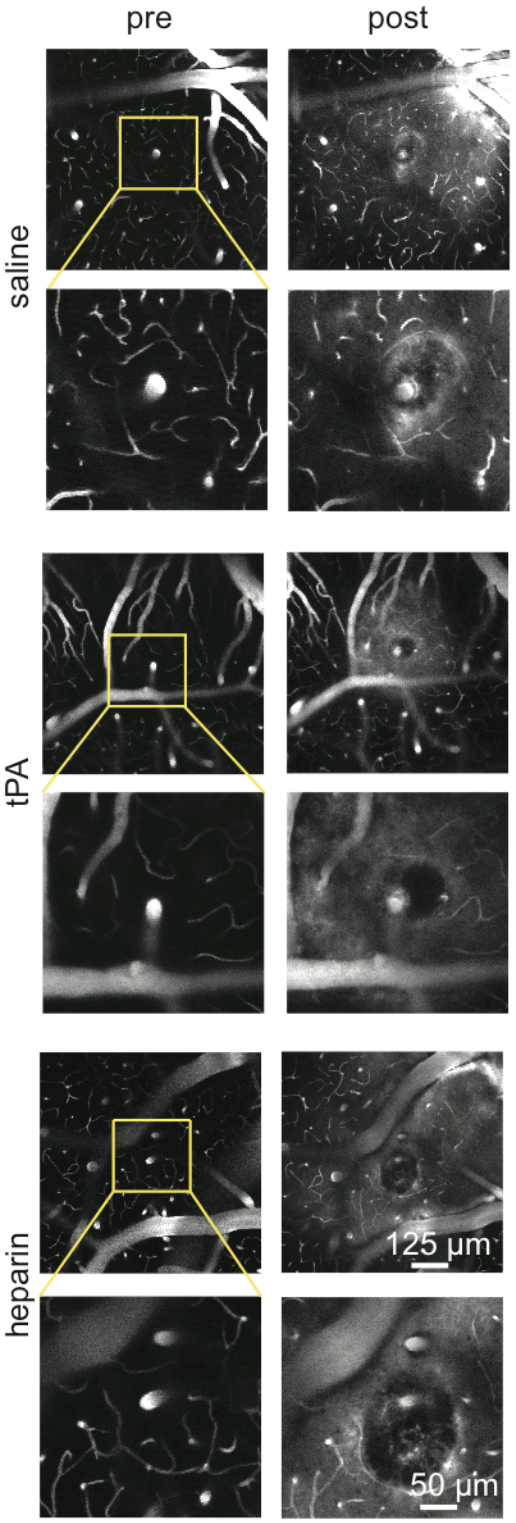

Figure 7.1 2PEF in vivo image projections of fluorescently-labeled blood plasma spanning a 20-µm depth centered at the hemorrhage origin

blood plasma 1.5-hr after microhemorrhage and found diameters of 485 +/-148 μm for saline and 526 +/- 213 μm for tPA treatment. We found no difference in the size of the blood plasma for both saline and tPA. Intravenous heparin led to an increase in blood plasma diameter size to 707 +/-187 μm ($p < 0.025$; Mann Whitney U test).

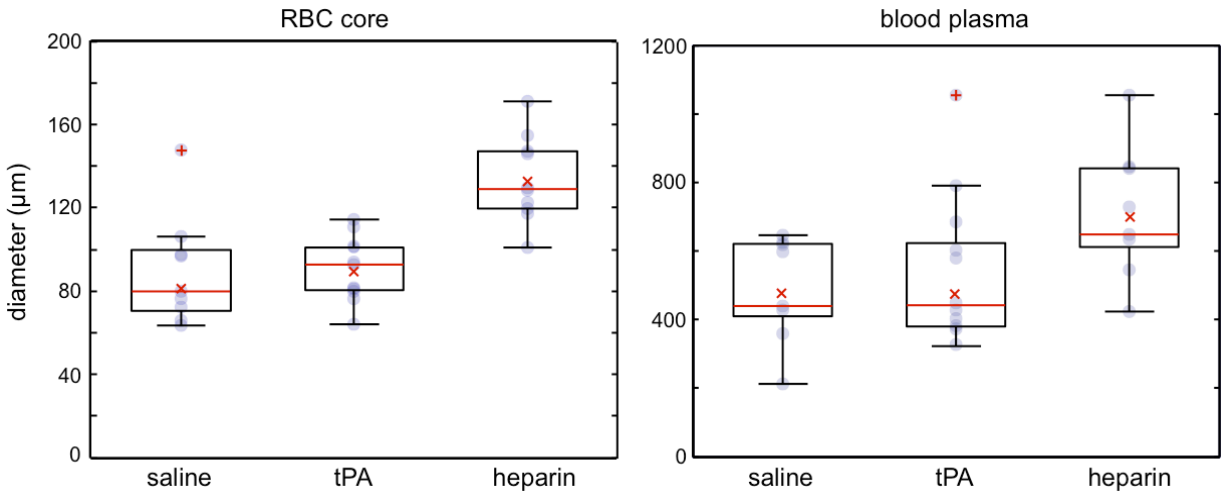

Figure 7.2 Boxplots for post-hemorrhage red blood cell and blood plasma extravasation diameters are shown for the three treatments: saline (n=9 microhemorrhages), tPA (n=11), and heparin (n=10).

We identified 18 of the femtosecond laser-induced ICH in post-mortem tissue sections. Across all treatments, we found that RBCs spread vertically along the perivascular space surrounding the targeted PA (Fig. 7.3a,b,c). Blood plasma, however, was able to diffuse through the parenchyma tissue and exhibited a more extended spatial pattern (Fig. 7.3d,e,f). We consistently observed that heparin treatment led to a larger spherical RBC-filled core compared to saline and tPA treatments.

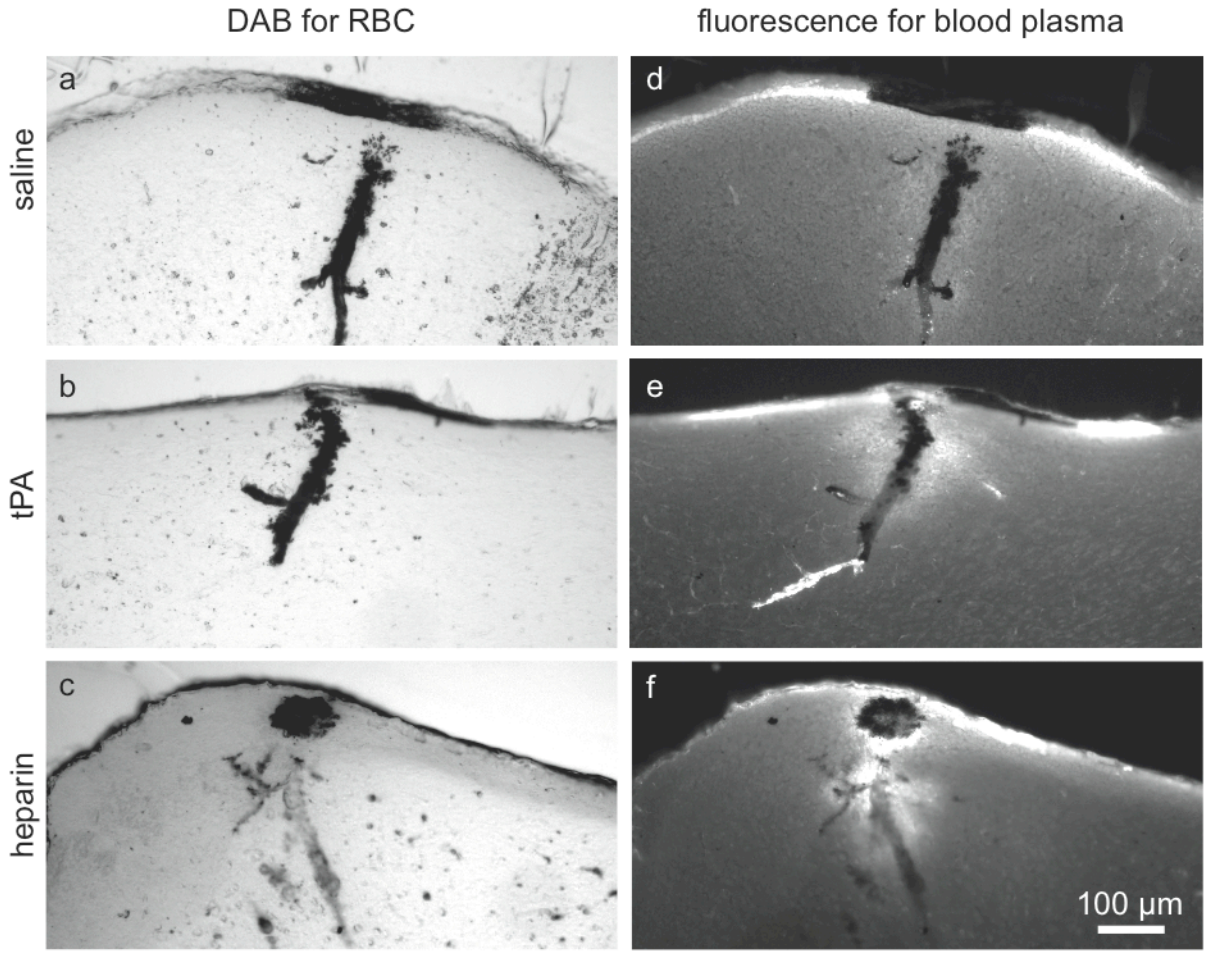

Figure 7.3 Histology sections post-ICH. (Left) 3,3'-Diaminobenzidine (DAB) staining reveals RBCs after ICH. (Right) Texas-Red dextran fluorescence reveal extravasated plasma post ICH.

Penetrating arteriole volume blood flux and laser energy used to make hemorrhage do not influence hemorrhage sizes

We tested whether there was any correlation between the measured RBC and plasma extravasation areas and the volume blood flux of the targeted PA or the laser energy used to trigger the microhemorrhage. Within the range of laser energies and PA blood fluxes studied here, there were no significant correlations between the RBC and plasma areas with penetrating arteriole flux rates or deposited energy across all three treatment groups (Pearson product-moment correlation coefficient for RBC

hemorrhage diameter, Spearman's rank correlation coefficient for plasma diameter).

DISCUSSION

TPA treatment after stroke may theoretically increase ICH size and negatively impact the health of the patient. We demonstrated that tPA application during ICH, using a femtosecond laser to rupture single PAs in the cortex of mice, did not acutely increase the size of the RBC core and extravasated blood plasma compared to saline treatments during ICH. However, we found that anticoagulant heparin significantly increased the RBC core and blood plasma size compared to saline treatments, and is consistent with previous findings involving other anticoagulants, such as warfarin [9]. TPA activates the fibrinolytic cascade and could possibly have an effect on rebleeding after blood vessel coagulation and hemostatis, which can negatively impact the health of patients [10]. We looked at extravasated RBC core and blood plasma diameters out to 1.5-hr after initial ICH but did not look at diameter changes at further time points, so it is possible that tPA can worsen the affects of an ICH. However, parameters of clot structure effects fibrinolytic activity of tPA, which can play a role in the maintenance of the clot. Platelet-rich thrombi are more stable than erythrocyte-rich thrombi during tPA treatment due to the release of platelet-derived plasminogen activator inhibitor [11]. Our work with ICH consists of whole blood extravasation into the brain, which carries a large amount of platelets, theoretically making the thrombus more resistant to tPA. The hematoma volume is dominated by target vessel clotting which limits the size of the hematoma[8]. This clot would need to be broken in order for extravasation of blood to re-establish.

Our results show that tPA does not enlarge hematoma sizes acutely after ICH. This result has profound implications on the clinical treatment and diagnostics for stroke patients. TPA can potentially be administered at earlier time points without the need to distinguish the type of stroke prior to treatment (i.e., occlusion or hemorrhage). In addition, our work can theoretically alter the treatment times for

stroke to earlier time points, which increases the effectiveness of the drug and can increase the physiological outcome of the patient.

REFERENCES

1. Zivin, J.A., Fisher, M., Degirolami, U., Hemenway, C.C. & Stashak, J.A. Tissue Plasminogen-Activator Reduces Neurological Damage after Cerebral Embolism. *Science* **230**, 1289-1292 (1985).

2. Marler, J.R. & Goldstein, L.B. Medicine - Stroke - tPA and the clinic. *Science* **301**, 1677-1677 (2003).

3. Zhang, S., Boyd, J., Delaney, K. & Murphy, T.H. Rapid reversible changes in dendritic spine structure in vivo gated by the degree of ischemia. *J Neurosci* **25**, 5333-5338 (2005).

4. Adams. Guidelines for the early management of adults with ischemic stroke: A guideline from the American Heart Association/American Stroke Association Stroke Council, Clinical Cardiology Council, Cardiovascular Radiology and Intervention Council, and the Atherosclerotic Peripheral Vascular Disease and quality of care outcomes in research interdisciplinary working groups (vol 38, pg 1655, 2007). *Stroke* **38**, E96-E96 (2007).

5. Morrison, L.J., Verbeck, P.R., McDonald, A.C., Sawadsky, B.V. & Cook, D.J. Mortality and prehospital thrombolysis for acute myocardial infarction - A meta-analysis. *Jama-J Am Med Assoc* **283**, 2686-2692 (2000).

6. Schaffer, C.B., *et al*. Two-photon imaging of cortical surface microvessels reveals a robust redistribution in blood flow after vascular occlusion. *PLoS Biol* **4**, e22 (2006).

7. Nishimura, N., *et al*. Targeted insult to subsurface cortical blood vessels using ultrashort laser pulses: three models of stroke. *Nature Methods* **3**, 99-108 (2006).

8. Rosidi, N.L., *et al*. Cortical microhemorrhages cause local inflammation but do not trigger dendrite pathology. *submitted* (2011).

9. Foerch, C., *et al*. Experimental Model of Warfarin-Associated Intracerebral Hemorrhage. *Stroke* **39**, 3397-3404 (2008).

10. Murray, V., *et al*. The molecular basis of thrombolysis and its clinical application in stroke. *J Intern Med* **267**, 191-208 (2010).

11. Jang, I.K., *et al*. Differential Sensitivity of Erythrocyte-Rich and Platelet-Rich Arterial Thrombi to Lysis with Recombinant Tissue-Type Plasminogen-Activator - a Possible Explanation for Resistance to Coronary Thrombolysis. *Circulation* **79**, 920-928 (1989).

CHAPTER EIGHT

THE DEVELOPMENT OF A HIGH SCHOOL SCIENCE CURRICULUM TO FURTHER DEVELOP THE UNDERSTANDING OF ENGINEERING AND PHYSICS APPROACHES TO SOLVING BIOLOGICAL PROBLEMS

Nathanael L. Rosidi[1], Karrie Frey[2], Shivaun Archer[1], Chris B. Schaffer[1]

[1]Department of Biomedical Engineering, Cornell University, Ithaca, NY

[2]Tully High School, Tully, NY

ABSTRACT

We have developed a curriculum to help high school students apply their quantitative approaches in physics to biological concepts and real-world applications. High school students in grades 11 to 12 in the Advance Placement physics and biology classes as well as the New York State Reagents chemistry class developed their understanding of physics and biology with our laboratories. A series of discussions and laboratory exercises held at Tully High School and Cornell University was conducted to help the students understand concepts in fluid dynamics. These exercises help develop concepts in biology that are analogous to the experiments conducted, such as physiological consequences to flow and nearby tissue after a stroke. An evaluation of the curriculum in the form of a lab report and survey, yielded an increase in understanding of concepts in biology and physics as well as how these two fields can be applied to real-world applications.

INTRODUCTION

A fundamental understanding of core concepts in physics and biology is important for the further development of advance topics in science as well as applications in real-world problems. The development of these fundamentals start in grade school where physics and biology concepts are introduced. These classes develop core concepts but a bridge between concept and application are not always present in curriculum [1].

Moreover, concepts in physics and biology are often isolated to their respected fields when real-world applications are introduced. For example, problems in biology use biological approaches to solve problems in the field. There is a need in research laboratories for scientists of different backgrounds to collaborate and help solve problems that may span several scientific disciplines. For example, the work in Dr. Chris Schaffer's laboratory uses engineering approaches to examine issues in neuroscience.

Students developing knowledge in the sciences often are not exposed to the connection between different science fields and how these fields can benefit one another.

With this realization, we have developed a curriculum that bridges the gap between physics and biology. Students are asked to use concepts in physics with concepts in biology to understand consequences and changes in disease state systems. Students will learn and develop several concepts in physics and biology such as microscopy, fluorescence labeling, role of redundancy in fluid flow networks, quantitative measurements and analysis. Finally, students will be able to apply these techniques with concepts in disease such as stroke.

CURRICULUM STRUCTURE

Two laboratories were conducted to develop the students' understanding of applied physics and how these approaches can be used to examine questions in biology. Our laboratories used optical techniques to study concepts in flow that are analogous to blood flow in the brain and consequences to the flow after injury, such as a blockage.

The laboratories involved 90 Advance Placement (AP) physics and AP Biology high school seniors at both Tully High School in Tully, NY and Cornell University in Ithaca, NY.

Laboratory 1 – Fluorescence in leaves

The first lab involved observing fluorescence in leaves using a series of optical filters and light sources. The purpose of the lab is to develop an understanding of flow in nature. We seek to understand consequences of the flow after injury and use inquiry based learning, applied physics, and engineering approaches to understand this concept.

Laboratory component

This lab took place at Tully High School in Tully, NY involving 30 Regeants Chemistry, 30 AP Biology, and 30 AP Physics High School students. The students were given a set of optical filters and a light source to build a device that enables the visualization of fluorescence in the veins of leaves. A table of components involved in the lab is listed in Table 8.1. The students were given no prior instructions or information about the optical filters or type of fluorescent dye used, enabling the development of inquiry based learning through a series of questions with instructors of

the lab.

Light source with yellow light emitting diode (LED)
Rhodamine b solution in dH20
Short-pass filter, 550-nm
Long-pass filter, 590-nm
SM1 lens tube

Table 8.1: List of components to build optical filter set

Prior to the start of the experiment, leaves were soaked in a rhodamine b fluorescent dye solution for several hours. Students were asked to draw the veins of a leaf and formulate an initial hypothesis of the consequences of flow through the vein if a blockage or injury were to occur. Students were then asked to set up multiple light filters and a light source to visualize the fluorescence in the veins of leaves without injury. Next, the students were asked to visualize the fluorescence in the veins of leaves with injuries such as tears along the veins of the leaf. Students were asked how the flow would change and if the area nearby the injury site would degrade or die. Figure 8.1 shows fluorescent visualization of an injured leaf soaked in fluorescent solution [2].

Figure 8.1 Visualization of fluorescence in the veins of a leaf. Reprinted figure with permission from Katifori, E., Szollosi, G.J. & Magnasco, M.O. Damage and Fluctuations Induce Loops in Optimal Transport Networks. Phys Rev Lett 104, (2010).. Copyright 2010 by the American Physical Society[2].

Class discussion

At the end of the laboratory experiment an open-class discussion was held to explain the concept of flow in biology and how this lab is analogous to flow in the brain and physiological consequences that may arise from complications in blood flow.

A presentation was held to show images of fluorescence in a rodent's brain representing blood flow and the physiological consequences after a blockage. The presentation was used to connect the concepts discovered in the leaf lab with concepts in neurobiology using physics and engineering approaches.

Laboratory 2 – Custom network flow lab at Cornell University

This lab involved 23 AP Biology and Physics senior and took place in the Biomedical

Engineering teaching laboratory at Cornell University. The purpose of this lab was to develop an understanding of how engineering and physics is involved in science such as biology and neurobehavior. Students also took a tour of Dr. Schaffer's laboratory to observe how research is applied from the classroom to research labs and the types of tools Dr. Schaffer's lab uses to approach biological questions. A tour of Cornell University's Nano Fabrication (CNF) lab took place after the Dr. Schaffer's lab tour and network flow lab had finished.

Laboratory Component

The implementation of the lab took place in the Biomedical teaching laboratory at Cornell University. Students were asked to build a network of serial and parallel connecting tubes in which 100-µm bead solution can flow through. Students were asked to draw a schematic of the network and measure the dimensions of each segment of tubing for future analysis. Finally, the students were asked to hypothesize the flow direction of the bead solution through the network of tubing before and after a blockage in one of the channels in the tube. Figure 8.2 shows a schematic tube network made during the lab.

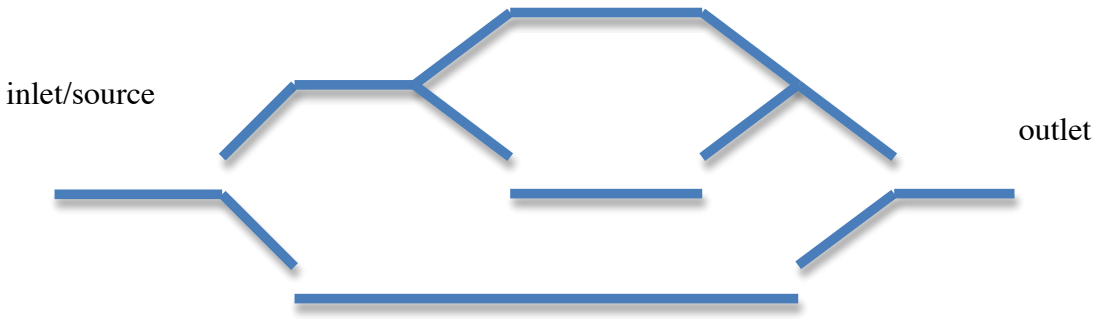

Figure 8.2 Schematic of microvascular network that can be made with tubing and connectors

Students then connected their network of tubes to a syringe pump and syringe containing bead solution. The bead solution was set to flow at a constant flow rate while the students measured the time it took for beads to travel a given distance, yielding velocity, using a bright-field microscope.

Once velocity measurements were taken for all tube segments in the network, students were asked to block a segment to study the rearrangement and distribution of flow after blockage. Students blocked a segment then repeated velocity measurements as described above for each segment of the network.

Laboratory discussion

Concepts pertaining flow through a network and its connection to blood flow in the brain took place during the laboratory and tour of Dr. Schaffer's research lab. Concepts pertaining to using engineering and physics approaches to solving biological problems took place at the CNF and Dr. Schaffer's research lab.

Flow in a network was discussed and how it pertained to neurobiology and the leaf lab. The discussions took place during the laboratory to help familiarize students with the equipment and provide a better understanding of concepts while performing the laboratory exercise. Other applications of physics in biology discussion took place at the CNF and Dr. Schaffer's research lab where engineering techniques were being applied to biological problems while the students observed.

EVALUATION OF CURRICULUM

Students were asked to complete a laboratory report on the network flow laboratory. The students were to answer a series of questions pertaining to the network they designed and to core concepts in flow and how it related to biology. The following questions were asked:

1. How would different pressures for each channel affect flow through the network?
2. What are some physiological examples of pressure changes our body undergoes?
3. Would a change in vessel diameter or vessel flow rate contribute to a greater change in pressure? What do you think our body does to compensate for changes in pressure?
4. What does a block in one channel do to network flow and direction? Is a blockage necessarily bad? Explain why it is or is not.
5. When a vessel branches, what will happen to the resistance? pressure drop? Relate this to the picture shown in the introduction graphing pressure from arteries to the capillary beds

The students were also asked to calculate the pressure drop for each tube segment and resistances in teach tube segment. The laboratory report was to contain introduction, materials and methods, results, and a discussion section similar to formatting in scientific journals. Laboratory reports were graded for completeness and competency.

Curriculum Assessment

Students were asked to fill out a series of survey questions to evaluate the both the leaf laboratory and the microvasculature laboratory at Cornell University. Students filled out the survey after each lab. The statements they were asked to evaluate were:

1. After conducting this experiment, I feel I understand how science can be applied to real-world applications
2. After conducting this experiment, I feel I understand how different science disciplines, such as physics, can be applied to other fields such as neuroscience.
3. I am more excited about science than before.
4. I enjoy this research experiments more than most labs.
5. After conducting this experiment, I feel I understand how scientists design their own experiments.
6. This experiment was more difficult than most labs.

Students were to evaluate these statements based on a numerical score between 1 and 5, with 5 being that the student agreed strongly with the statement and 1 being that the student disagreed strongly with the statement.

Table 1 shows the average numerical response after completion of the lab. Students after only completing the leaf lab scored question 1-5 between 3.0 and 3.81 but scored question 6, this experiment was more difficult than most labs, a 1.45. This shows that the students enjoyed and understood the science and experiments but thought the leaf laboratory experiment was not as difficult as other labs they conducted in the past.

Students after completing both the leaf lab and the microvasculature lab at Cornell

University scored between 2.95 and 4.3 across statements 1 through 6, indicating that the students enjoyed and understood the experiments and were academically challenged with the lab taught at Cornell University. These numbers can be seen in Table 8.2.

Statement	Average Evaluation score from students completing only leaf lab	Average Evaluation score from students completing both labs
After conducting this experiment, I feel I understand how science can be applied to real-world applications	3.8	4.1
After conducting this experiment, I feel I understand how different science disciplines, such as physics, can be applied to other fields such as neuroscience	3.5	4.3
I am more excited about science than before	3	2.95
I enjoy this research	3.5	3.13

experiment more than most labs		
After conducting this experiment, I feel I understand how scientists design their own experiments	3.6	3.6
This experiment was more difficult than most labs	1.45	3.4

Table 8.2: Student assessment of laboratory exercises

CONCLUSIONS

We have developed a curriculum to help students understand the application of their classroom knowledge in real-world problems. Moreover, we introduce the concept of using engineering and physics approaches to solve biological problems in a research setting, therefore applying much of their classroom knowledge in physics with laboratories containing biology concepts. Students were provided with guidance from professors and graduate students in the laboratories and were encouraged to use inquiry-based learning to solve challenges faced in the labs.

The laboratory report after the network tube lab showed that the majority of the students understood the concepts of flow in the network of tubes and could relate it to biological topics, such as blood flow in the brain and the physiological consequences after a clot.

Students, according to the post-curriculum survey enjoyed and understood the laboratories both at Cornell University and at Tully High School. The students thought that the leaf lab conducted at Tully High school was not as difficult than other labs they have previously conducted. However, students that conducted both the leaf lab and the microvasculature lab at Cornell University thought the lab was more difficult than past labs.

A number of changes can be made for the upcoming years to help students better understand concepts pertaining to the labs. With the leaf lab, additional light sources with different colors could be used to test inquiry based learning and development of optical knowledge to help visualize fluorescence in the veins of the leaf. At the end of the lab, explanation of fluorescence will help with the understanding of physics inherent in the lab.

Several changes can be made to the network tube lab. Prior discussions on network resistances and pressure-mediated flow through tubes could help strengthen the understanding of the physics involved in the lab. Homework assignments that ask students to hypothesize the flow through networks when resistances and pressure change along networks would help students understand core concepts when running the lab.

Lastly, other learning techniques could be implemented to compliment inquiry-based learning. These techniques can help students understand concepts and come out with a deep understanding of the physics and biology of the topics taught.

REFERENCES

1. Roth, W. Bridging the Gap Between School and Real Life: Toward an Integration of Science. *Mathematics, and Technology in the Context of Authentic Practice, School Science and Mathematics* **92**, 307-317 (2010).

2. Katifori, E., Szollosi, G.J. & Magnasco, M.O. Damage and Fluctuations Induce Loops in Optimal Transport Networks. *Phys Rev Lett* **104**, - (2010).

CHAPTER NINE

CONCLUSIONS AND FUTURE DIRECTIONS

CONCLUSIONS AND FUTURE DIRECTIONS

The ability to provide time-lapse, cell specific observations of the physiological consequences in disease state biological systems has further integrated techniques developed in engineering and physics with topics in neurobiology. Using novel nonlinear optical methods, used previously in applications such as micro-machining, we can now experimentally induce microscopic lesions in a live intact brain to study disease. The work in this dissertation takes advantage of these optical techniques to help provide an understanding of the physiological response after a microvascular lesion. In this final chapter, we will review some of the major conclusions presented in the dissertation as well as present topics where future work can be explored.

We looked at the response of nearby blood vessels after an occlusion to a penetrating arteriole. By measuring flow rates and diameter changes of nearby pial and penetrating arterioles, before and after the occlusion, we found no active vasoregulation that increased blood flow to the occlusion area. However, capillaries directly downstream from the occluded penetrating arteriole did dilate but remained slow. Capillaries not connected to the occluded penetrating arteriole, but in the hypoxic area, did not experience the same dilation or blood flow decrease. This spatial intermingling of slow, dilated capillaries with unaffected capillaries indicates that the mechanism to dilate blood vessels is vasogenic in origin and travels along the vessel walls. Application of vasodilator, acetylcholine, resulted in an increase in diameter and blood flow of surrounding blood vessels, indicating that mechanisms for dilation were not affected by our technique.

Our findings suggest that occlusions to single penetrating arterioles do not lead to active compensatory mechanisms that increase blood flow to the affected area. Furthermore, capillaries downstream did not increase in blood flow even after

application of a vasodilator. This may be one reason why vasodilators such as xanthine derivatives have not been unsuccessful in the treatment for stroke or vascular dementia. In future work, isolating mechanisms that enable increases in blood flow to the stroke region may provide a platform for therapy.

Microhemorrhage bleeding, dendrite health, and microglia/macrophage response was characterized acutely and out to seven days. After rupturing a penetrating arteriole using tightly focused femtosecond laser pulses, we found that bleeding and blood extravasation is limited by vessel clotting. Intracranial pressure between the hematoma and surrounding tissue interface was not high enough to cause capillaries to collapse, ruling out acute ischemia as a possible mechanism for injury. We find that although cortical dendrites near the red blood cell (RBC) filled core did not show signs of structural degeneration, an inflammatory response of microglia and macrophages invaded the affected area 1.5-hr after the microhemorrhage and persisted out to seven days.

In future work, isolating the minimum hemorrhagic area before neuronal degeneration develops can provide new perspectives for stroke therapy. For example, if an injury to a patient is below the minimum spatial area that illicits cellular degeneration, then more aggressive strategies for stroke treatment could be administered.

We hypothesized that even though structural degeneration of neuronal dendrites were not observed after microhemorrhage, subtle changes in spine maintenance may take place. Changes in dendrite spine growth and loss rates may alter the function of neurons within the hemorrhage area. Preliminary data has suggested differences in dendrite spine turnover rates, defined as the rate of spine growth and loss, between spines in the hemorrhagic region and spines on the contralateral side of the brain, where no hemorrhage injury was induced.

Work integrating engineering techniques to solve issues in medicine has provided potential new platforms for therapeutics. The ability to manipulate biological systems and collect quantitative information over time in a live intact animal model can help advance our understanding of injury mechanisms and provide a testbed for the evaluation of new therapeutic strategies in medicine.